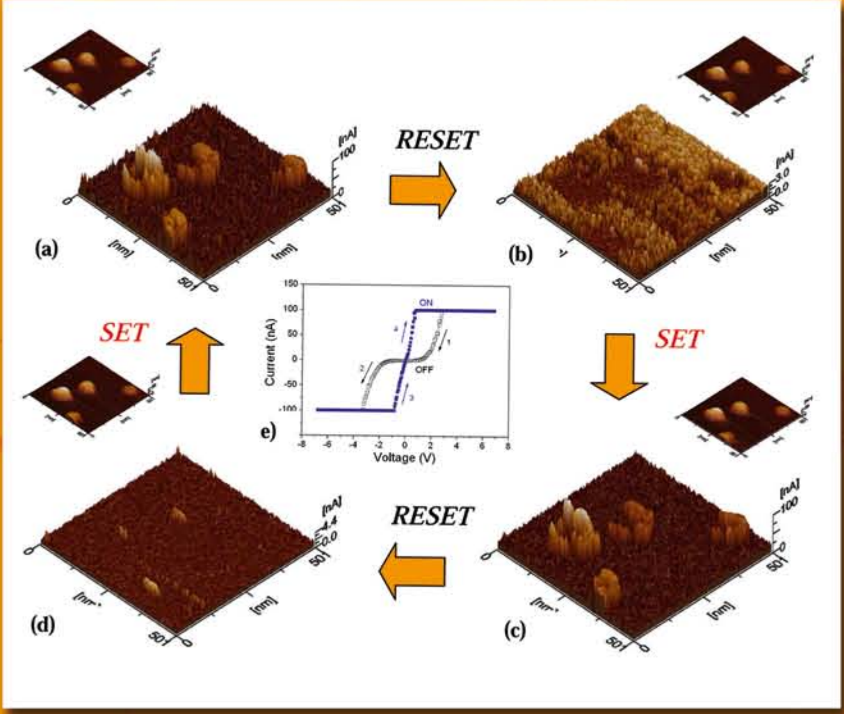

Resistive switching in TiO2 thin films

Lin Yang

JÜLICH
FORSCHUNGSZENTRUM

Schriften des Forschungszentrums Jülich
Reihe Information / Information Band / Volume 17

Forschungszentrum Jülich GmbH
Peter Grünberg Institut (PGI)
Elektronische Materialien (PGI-7)

Resistive switching in TiO2 thin films

Lin Yang

Schriften des Forschungszentrums Jülich
Reihe Information / Information Band / Volume 17

ISSN 1866-1777 ISBN 978-3-89336-707-8

Bibliographic information published by the Deutsche Nationalbibliothek.
The Deutsche Nationalbibliothek lists this publication in the Deutsche Nationalbibliografie; detailed bibliographic data are available in the Internet at http://dnb.d-nb.de.

Publisher and Distributor: Forschungszentrum Jülich GmbH
Zentralbibliothek
52425 Jülich
Phone +49 (0) 24 61 61-53 68 · Fax +49 (0) 24 61 61-61 03
e-mail: zb-publikation@fz-juelich.de
Internet: http://www.fz-juelich.de/zb

Cover Design: Grafische Medien, Forschungszentrum Jülich GmbH

Printer: Grafische Medien, Forschungszentrum Jülich GmbH

Schriften des Forschungszentrums Jülich
Reihe Information / Information Band / Volume 17

D 82 (Diss., RWTH Aachen University, 2010)

ISSN 1866-1777
ISBN 978-3-89336-707-8

Abstract

The continuing improved performance of the digital electronic devices requires new memory technologies which should be inexpensively fabricated for higher integration capacity, faster operation, and low power consumption. Resistive random access memory has great potential to become the front runner as the non volatile memory technology. The resistance states stored in such cell can remain for long time and can be read out none-destructively by a very small electrical pulse. In this work the typically two terminal memory cells containing a thin TiO_2 layer are studied.

Polycrystalline TiO_2 thin films are deposited with atomic layer deposition and magnetron reactive sputtering processes, which are both physically and electrically characterized. The resistive switching cells are constructed in a metal/TiO_2/metal structure. Electroforming process initiate the cell from the beginning good insulator to a real memory cell to program the resistive states. Multilevel resistive bipolar switching controlled by current compliance is the common characteristic observed in these cells, which is potentially to be used as so called multi-bit memory cells to improve the memory capacity. With different top electrodes of Pt, Cu, Ag the resistive switching behaviors are studied. The switching behaviors are different depending on the top metal such as the minimum current compliance, the endurance of the programmed resistance states and the morphology change during the switching. The temperature dependence of different resistance states are investigated. A reduction of the activation energy and their possible conduction mechanisms is discussed on the base of the basic current conduction models. It is found that the resistance state transfers from semiconductor to metallic property with the reducing resistances. The calculated temperature coefficients of their metallic states on the Cu/TiO_2/Pt and Ag/TiO_2/Pt are very close to the reported literature data, which implying a Cu and Ag filament formation.

With the help of conductive atomic force microspectroscopy the local conductivity of the initial TiO_2 thin films and the TiO_2 in ON state after removing the top Cu electrode are investigated. The results from both cases confirm the local filaments formation in nanometer scale under the proper electrical voltages contributing to the observed switching behaviors. The time of flight secondary ion mass spectroscopy analysis shows the interdiffusion of Cu into the TiO_2 layer. Therefore the resistive switching in the TiO_2 with Cu electrodes could involve the electrochemical metallization process which forms and dissolves the Cu filament with respect to the applied voltage.

Kurzfassung

Neue nicht flüchtige Speichertechnologien rücken verstärkt in den Fokus der Wissenschaftler und Unternehmen, um das Tempo der Weiterentwicklung der hoch leistungsfähigen elektrischen Devices mitzuhalten. Solche Speichertechnologien müssen mit Standardhalbleiterprozessen gut kompatibel sein und die weiteren Kriterien wie zum Beispiel hohe Speicherdichten, schnelles Einschalten/Ausschalten und geringem Energieverbrauch erfüllen. Resistive Random Access Memory ist eine der Speichertechnologien, die am intensivsten erforscht wird, und hat dadurch großes Potential als zukünftige Technologie. In solchen RRAM Zellen müssen die progammierten resistiven Zustände für lange Zeit beibehalten werden, während die Zustände mit sehr niedrigen elektrischen Pulsen zerstörungsfreie ausgelesen werden. In dieser Arbeit wird das resistive Schalten auf Basis von TiO_2 Dünnschichten untersucht.

Polykristalline TiO_2 Schichten wurden mittels atomic layer deposition and magnetron reactive sputtering hergestellt und sowohl physikalisch als auch elektrisch charakterisiert. Die resistiven Speicherzellen sind in der Form Metall/TiO2/Metall aufgebaut. Die Zellen, die am Angang nur ein guter Isolator sind, wurden mit einem speziellen Elektroforming-Prozess für die danach kommenden Schaltzyklen aktiviert. Multilevel bipolares resistives Schalten geregelt von der Current Compliance könnte durch das Speichern von mehr als zwei Bits zur Erhöhung der Speicherkapazität beitragen. Die unterschiedlichen Schalteigenschaften wie zum Beispiel die minimale Current Compliance, die Haltbarkeit der programmierten resistiven Zustände und die morphologische Veränderung in den Zellen mit verschiedenen Topelektroden von Pt, Cu, Ag wurden beobachtet. Verschiedene resistive Zustände (anfänglicher Zustand, OFF Zustand und drei unterschiedliche ON-Zustände) wurden mit Temperaturmessungen untersucht. Damit wurden die möglichen elektrischen Leitungsmechanismen basierend auf grundlegenden theoretischen Modellen diskutiert. Es wurde gefunden, dass sich die Aktivierungsenergie mit der Reduktion der Widerstände verringert. Gleichzeitig entsteht eine Übergangsphase der Leitfähigkeit zwischen Halbleiter und Metall. Die Temperaturkoeffizienten der metallischen resisitven Zustände der Zellen mit jeweils Cu und Ag Topelektroden sind ähnlich zu den veröffentlichten Daten und weisen deshalb darauf hin, dass Cu oder Ag Filamente in den Zellen ausgebildet wurden.

Mit Hilfe vom Conductive Atomic Force Microscopy wurde die Leitfähigkeit eines einzelnen Orts mit einem Durchmesser bis 10 nm sowohl in initialen TiO_2/Pt Probe als auch in ON-Zustand programmierten Zelle nach dem Entfernen der Cu Elektrode untersucht. Die Ergebnisse bestätigten den Zusammenhang des lokalen Pfadwachstums mit dem resistiven Schalten in den Zellen. Die Wanderung der Cu Ionen nach dem Schalten wurde mit Time of Flight Secondary Ion Mass Spectroscopy bestätigt. Deshalb könnte ein elektrochemischer Metallierungsprozess in den Zellen auf Grund der Cu (ähnlich auch mit Ag) Wanderung unter den entsprechenden elektrischen Spannungen stattfinden.

Danksagung/Acknowledgement

Für meine Doktorarbeit schulde ich sehr vielen Menschen einen herzlichen Dank. Zuerst möchte ich mich bei meinem Doktorvater Herr Professor Rainer Waser für die tolle Chance herzlich bedanken, an seinem Institut diese Arbeit anfertigen zu dürfen. Besonders bedanke ich mich bei meinen zwei Betreuern Dr. Carsten Kügeler und Dr. Andreas Rüdiger, denn Sie brachten mir sehr viel Geduld entgegen und sorgten mit wertvollen Ratschlägen für das Gelingen der Arbeit. Des Weiteren möchte ich mich bei meinen Eltern bedanken, ohne die ein Studium und eine Doktorarbeit niemals möglich geworden wären.

Ein großer Dank geht auch an Herr Professor Szot, Ruht Münstermann und Dr. Menke für die Unterstützung und Diskussion bei CAFM Messungen. Des Weiteren gilt meiner großer Dank Dr. Susanne Hoffman-Eifert, Herr Professor Herbert Schröder und Dr. Xin Guo, für die Diskussionen mit ihrem fundierten Fachwissen und ihre Ideen.

Hans Haselier, Holger John, Dr. Takayuki Watanabe, Manfred Gebauer, René Borowski danke ich für die Unterstützung bei der Prbenherstellung. Weitere möchte ich Marcel Gerst für die Hilfe bei Problems mit Computer und Internet und Jochen Friedrich, Dr. Uwe Breuer, Andrea Stärk, Dr. Astrid Besmehn, Sandra Gilles für die Materialcharakterisierungen. Maria Gacia gilt mein besonderer Dank für die Organisation und nette Hilfe.

Danke sage ich auch meinen Kollegen Rohit Soni, Dr. Christian Nauenheim, Dr. Matthias Meier, Roland Rosezin, Jiahua Zhang, Florian Lenz, Dr. Christina Schindler, Dr. DooSeok Jeong, und alle anderen für die freundlichen Zusammenarbeiten. Mit euch habe ich auch viele Spaß bei meinem Aufenthalt in Institut gemacht.

Auch geht mein Dank an meine Eltern und meinen Bruder, der mich stets bestärkt hat, wenn ich an mir gezweifelt habe.

Danke!!

Contents

List of Figures

Abbreviation

AFM	Atomic Force Microscopy
ALD	Atomic Layer Deposition
CAFM	Conductive Atomic Force Microscopy
CMOS	Complementary Metal Oxide Semiconductor
CVD	Chemical Vapor Deposition
DRAM	Dynamic Random Access Memory
ECM	Electrochemical Metallization Effect
FeRAM	Ferroelectric Random Access Memory
HRS	High Resistance State
LRS	Low Resistance State
MLC	Multi Level Cell
MRAM	Magnetic Random Access Memory
PCM	Phase Change Memory
PRAM	Phase Change Random Access Memory
PVD	Physical Vapor Deposition
RRAM	Resistive Random Access Memory
SEM	Scanning Electron Microscopy
ToF SIMS	Time of Flight Secondary Ion Mass Spectroscopy

Chapter 1 Introduction

The fast development of the memory technology is accompanied by the continuing thrive on the computer technology and other functional consumer electronics such as PDAs (personal digital assistants), laptop computers, digital audio players, digital cameras and mobile phones. Two kinds of memory currently dominate the market: the electrical addressed memory and the mechanical addressed memory. The former includes typically the dynamic random access memory (DRAM) and flash memory, which are also called semiconductor memory. The mechanical addressed memory mainly refers to the magnetic storage memory typically hard disk which has much higher storage capacity and lower price than DRAM and flash memory. However, the electrical addressed memories like DRAM are widely applied as the primary memory because of their very fast reading and programming speed. Although DRAM composed of a transistor and a capacitor to store information operates with very short cycle time even lower than 2 ns as unveiled by IBM in 2009 for their new embedded DRAM (eDRAM) with a 32 nm silicon on insulator (SOI) technology, [1] the stored information cannot be maintained without power and therefore is volatile. Non volatile electrically addressed memory attract more and more attention these years with the growing demand for large capacity of the information storage, low power consumption and meanwhile the fast operation speed comparable with the volatile RAM. Currently the flash memory is the most widely used non volatile memory in memory cards in many above mentioned consumer electronics and USB flash drivers. But the feature size of the flash memory cells will reach approximately the limitation of the technology at ~ 20 nm by around 2010. Even though further improvement of the memory density is possible by using multi level cell (MLC) or 3-D stacking structures, it may be not economically to drive the scalability to smaller dimensions. On the other side the flash memory operates with a much slower access time ~ 25 µs (Hynix) compared with the volatile RAM. [2] Therefore for the future applications new generation of the non volatile memory technologies are intensively researched and developed in order to drive this technology to the real productions with higher integration scalability, lower power consumption, fast programming and compatible to the existed semiconductor manufacturing processes.

Many companies and research institutes are involved in the development of the new memory technologies such as the magnetoresistive RAM (MRAM), Ferroelectric RAM (FeRAM), Phase change RAM (PRAM) and Resistive RAM (RRAM). All these upcoming new non volatile RAM technologies are vying for the dominance in the “universal memory” race and have potential to replace all existing semiconductor memories and to require few changes to the manufacturing equipment used for the standard CMOS technology. MRAM stores the data not with the electric charge but by magnetic polarities. A MRAM cell composes two ferromagnetic plates separated with a thin insulating layer. The resistance of such a cell is determined by the polarities of the both magnetic plates due to the magnetic tunnel effect: the stored information is regarded as “0” if both plates have same polarity and “1” if both the states have different polarities. The magnetic state of the writable plate can be programmed through an induced magnetic field created by the current flowing in the write line. Such write process requires much higher power, three to eight times needed for reading. On the other side the induced magnetic field could overlap the adjacent cells and lead to a false writing. Therefore MRAM technologies currently don’t show very promising higher scalability and suffer from the high power consumption similar to the flash memory. However IBM has demonstrated the very fast operation of the MRAM cells with an access time in the order of 2 ns, [3] which is almost 1000 times faster than the flash memory. FeRAM is another alternative non volatile memory technology with a similar construction of DRAM but uses a ferroelectric layer instead of a dielectric layer. By changing the polarization of the ferroelectric material under the applied electrical field the information of “0” and “1” can be programmed and stored in the FeRAM cell. The FeRAM technology shows advantages over the flash memory because of its low power consumption, fast write performance (35 ns) and much greater endurance for write-erase cycles. [4] The most drawback of the FeRAM is its low integration density and higher cost. The PRAM programs and store the information by switching the materials typically chalcogenide glasses into amorphous by heating the material above the melting temperature or into crystalline by heating below the melting point. The state of the material has dramatically influence on the electrical resistance of the cell: high resistance state in amorphous and low resistance in crystalline state. Same material can be used for the rewritable optical media like CD-RW and DVD-RW, where the refractive index is changed with the state of the material. In recent years several companies announced the progress made in the PRAM research and productions. In 2008 Intel and ST Microelectronics announced four-state MLC PRAM and begin shipping samples to customers. [5] [6] In September 2009 Samsung announces mass production start of 512M bit PRAM device. The great challenges of the PRAM facing is the higher current required for writing process in the range of upper micro ampere and mille ampere. However, the new progress made in the research on the RRAM technology has shown the attractive properties for a promising alternative future non volatile memory.

Typically a RRAM cell is in a configuration of metal/insulator/metal (MIM) stack structure. The principal of the RRAM technology is the switching of the resistance states of the insulator layer by applying a proper electrical voltage between low resistance state (LRS or ON) and high resistance state (HRS or OFF) corresponding to “1” and “0” respectively. The sandwiched dielectric layer “I” spans from a great variety of materials such as binary transition metal oxides, perovskite oxides, chalcogenides and SiO_2. The studies until now indicate the very impressive performance of this kind of memory in many respects compared with the existing flash and other upcoming new non volatile memory technologies. (1) Lower power consumption and faster write speed. RRAM cell of $Cu/SiO_2/Ir$ can operate with much lower current even down to 25 pA and much lower voltage around several hundred milli volts according to the published results by Schindler et al, [7] which reduces the power consumption dramatically with respect to the high current and voltage operation in the PRAM, MRAM and flash memory. RRAM operates with a fast switching timescale less than 10 ns. Fujitsu demonstrated the high speed (5 ns) low power (100 μA) RRAM technology with the configuration of Pt/Ti:NiO/TiOx/Pt in 2007. [8] 4DS Inc. announced also in 2009 that their high capacity RRAM works with a fast write time between 5 – 10 ns, near to the DRAM write time ~ 2 ns and 3 order of the magnitude faster than the current flash memory. (2) Simple structure and higher scalability. Researches indicated that the resistive switching occurs in most cases locally in the cell, which could be down to 10 nm as demonstrated with conductive atomic force microscopy (CAFM) by Szot et al. and in this work as well. [9] This indicates the potential to further scale down the RRAM memory cell to 10 nm, which results in the possible high density integration normally in the form of the crossbar arrays on the chip. 4DS Inc. has announced the 1 – 10 gigabit memory chip with an excellent endurance of 1 billion write/read cycles. [10] HP has also demonstrated the crossbar arrays RRAM on the base of the TiO_2 thin films and declared to begin prototyping RRAM using their memristors in July 2008. [11] (3) Lower cost fabrication using existing semiconductor manufacturing equipments. As already mentioned the RRAM has very simple MIM structures which can be fabricated with common PVD or CVD processes. Most of the materials showing resistive switching such as the transition metal oxides, SiO_2, chalcogenide and perovskites are compatible to the CMOS manufacturing process and therefore no specific equipments required for the industrial production of the RRAM.

It will take still some time to move the RRAM technology into the real production although such kind of memory has already shown its very impressive performances compared with other candidates of the potential alternative non volatile memory. Besides the further increasing of the integration density with new lithography technologies RRAM technology so far need to be further optimized in order to improve its operation stability and reduce the cost. However the exact resistive switching mechanisms is still going to be fully understood despite growing interest and efforts done according to the published results, which becomes an obstacle to improve the RRAM performance currently. The research group led by Prof. Waser in Forschungszentrum Jülich has researched intensively on various typical materials such as the transition metal oxides (TiO_2, NiO, WO_3), perovskites ($SrTiO_3$), SiO_2 and chacogenide (Ag:GeSe) and progresses was made. In most cases an electroforming process is needed in order to initiate the virgin MIM stack cell to be switchable. On the base of the various reports and observations the mechanisms of the resistive switching can be either due to the formation of the local filament or the interface effects between the electrode and the insulator layer. Depending on the different dielectric material system and the electrochemical activity of the electrodes materials either oxygen vacancies or electrochemically active metal ions migration or even both effect are involved in the resistive switching effect. However in such perpendicular

MIM structures the local filament is very difficult to directly observed and characterized because of the very fine dimension in nanometer scale. Therefore, some principle aspects are still highly concerned such as the identification and controlling of the switching location(s), the change of the compositions responsible for the switching phenomenon and so on.

Titanium dioxide TiO_2 is a well known insulator dielectric material widely used as pigment, photocatalyst, gas sensor and solar cells. TiO_2 thin film sandwiched between two metal electrodes (Pt, Cu, Ag) exhibits repetitive resistive switching behavior. Most published papers about the resistive switching in TiO_2 with two inert metal electrodes are unipolar switching with very high programming current above milliampere (mA) range and with poor endurance of write/erase cycles, which is very negative for the application as commercial RRAM productions. Jeong reported the observation of coexistence of the unipolar and bipolar resistive switching in the $Pt/TiO_2/Pt$ configuration. But the programming current is still high around 1 mA. [12] With a Ag electrode the programming current to switch ON or OFF on TiO_2 can be reduced down to nanoampere range. However the low resistance state with low programming current is only stable at low temperatures as reported by Tsunoda. [13] However his research shows the dramatically reduced switch ON and switch OFF voltage at around + 0.2 V and – 0.15 V, which is much lower than the reported resistive switching with both inert metal electrodes and very similar to the voltage in chalcogenide system with one electrochemical active Cu or Ag electrode. Therefore in this case the Ag migration into the TiO_2 should form or dissolve the filament with respect to the applied voltage. Interface effect is also proposed by HP group to be responsible for the resistive switching in $Pt/Ti/TiO_2/Pt$ stack system. They believe that the resistance changes with the oxygen migrations according to the voltage resulting in the modification of the Schottky barrier in the interface.

Silver is not a common electrode materials in the CMOS manufacturing process because of the expensive cost and the possible contamination for its easy diffusion in the solid materials. However copper is already common used as electrode and conduct line in the CMOS technologies and it is also an electrochemical active metal as the Ag. The resistive switching related to the Cu or Ag migrations in dielectric thin films like chalcogenide, SiO_2 exhibits generally the low programming current and voltage, which meets the requirement of the low power consumption for the future non volatile memory technology. Therefore in this work the resistive switching in TiO_2 with different electrodes of Pt, Cu and Ag is investigated:

(1) $Pt/TiO_2/Pt$ system shows some new behaviors of the bipolar resistive switching such as the dramatically reduction of the switching current down to 200 μA, the multi level bipolar resistive switching and the repetitive transfer between bipolar and unipolar switching.
(2) Bipolar resistive switching in $Cu/TiO_2/Pt$ is studied for its multilevel behaviors, scalability, endurance and retention of both programmed LRS and HRS. For

comparison the resistive switching of $Ag/TiO_2/Pt$ is also investigated.

(3) Temperature dependence measurements of the different resistance states from virgin state, HRS and 3 different LRS, the investigation of the activations energy of these states and some discussion about the possible conduction mechanisms.

(4) Resistive switching in nano meter scale on the virgin sputtering and atomic layer deposition (ALD) TiO_2 with CAFM measurement is investigated and compared with each other. The local resistive switching on a cell of LRS after the removing of the top Cu electrode is investigated with CAFM as well.

The structure of this thesis is arranged as following. Chapter 2 introduces briefly the material TiO_2 which is used as the matrix for the resistive switching in this work. The important proposed mechanisms related to the resistive switching are summarized as well. The techniques for the thin film deposition either for TiO_2 or metal oxides such as sputtering, ALD, and Evaporation are described. The sample preparing process is sketched and introduced. The characterizations of the thin film with different techniques are shown in chapter 4. The electrical measurement results and the CAFM results are presented in chapter 5. Some new observations and bubble formation are discussed. In Chapter 6 the resistive switching in the TiO_2 thin films with electrochemical active metal electrodes Cu and Ag are presented and discussed. The temperature measurements of 5 different resistance states are discussed with the calculations on the base of the conduction mechanism in MIM structure. Both characterized metallic ON state in $Cu/TiO_2/Pt$ and $Ag/TiO_2/Pt$ cells supports the Cu or Ag filament formed in the TiO_2 layer. The results obtained from CAFM measurement on the virgin TiO_2 as well as the cell in ON state after etching Cu top electrode show the different geometric and resistive switching in nano meter scale. The SIMS measurement on the cell in ON state confirms the Cu interdiffusion into the TiO_2 after forming and switching. Finally the results are summarized in the Chapter 7. An outlook for the further study on the resistive switching on TiO_2 with Cu electrode is also discussed.

Chapter 2 Fundamentals and overview of resistive switching mechanisms

2.1 Fundamentals of TiO_2, defects and electrical conduction

2.1.1 TiO_2

Titanium dioxide has wide applications in pigments, photocatalyst, dye-sensitised solar cells, antireflection layers and gas sensors. With incorporate voids amorphous TiO_2 shows no strict crystal structures in the film, which is normally deposited at a lower temperature range (under 150°C). [14, 15] Three crystal structures are observed in TiO_2: anatase, rutile and brookite. Two of them – anatase and rutile crystallographic structures – are the common form in thin films. Their crystal structures are sketched with a ball-and-stick model, as indicated in Figures 2.1 (a) and (b) respectively. The red balls represent the oxygen atoms and the grey balls titanium atoms. [16, 17] Both have a tetragonal structure but the rutile type has a larger density than the anatase and amorphous TiO_2 thin films. The anatase phase can convert to the rutile phase by higher annealing or with a higher deposition temperature (above 700°C).

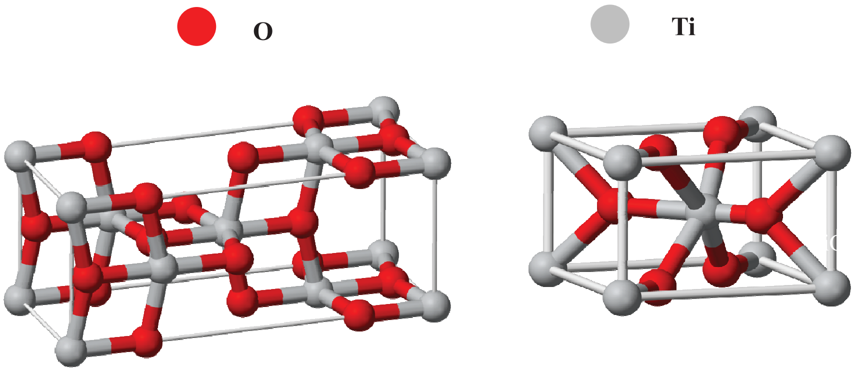

(a) (b)

Figure 2.1: Crystal structure of (a) anatase and (b) rutile.

For chemical vapour deposition methods (CVD) the crystallographic structures of the deposited thin films are normally controlled by the substrate temperature or the process temperature. For physical vapour deposition methods (PVD) it is controlled by the kinetic energy of the atoms hitting the surface of the thin films. Therefore, rutile structures can be formed at a lower deposition temperature with optimised processes conditions. [18, 19, 20] In this work, the TiO_2 thin films are deposited by the atomic layer deposition (ALD) at 240°C and DC magnetron sputtering deposition at room temperature. Both methods studied produce polycrystalline structures, which will be discussed in Chapter 3.

The physical, chemical and optical properties depend significantly on the microstructures – crystal phases and amorphous – which are greatly determined by the deposition methods and conditions. Stoichiometric TiO_2 is a good electrical insulator with a wide band gap of 3.0–3.5 eV. The refractive index n of TiO_2 varies from 2.0 to 2.7 depending on the deposition techniques and composition, which generally increases with the phase conversation from amorphous to anatase to rutile. [21] The refractive index is one of the most important parameters for the description of models such as the Schottky conduction and Poole–Frenkel conduction in solid materials.

In this work, the resistance change of the TiO_2-based metal–insulator–metal (MIM) structures during electroforming or switching procedures involves the localised redox reaction or the interdiffusion of the Cu or Ag atoms into the thin films. Therefore, it is necessary to give some brief introduction on the defect and electrical conduction in solid materials.

2.1.2 Defects and non-stoichiometric TiO_2

In solid electrochemistry, the defects in bulk, interfaces and surfaces have a significant influence on the catalytic activity and mass transport as well as the electrical conduction of the solid materials. [22, 23] These different defects can be classified into the following groups:

(a) Point defects (intrinsic and extrinsic)

Point defects, such as vacancies, interstitial ions or substituted ions, can occur in all crystalline materials. Generally, they fall into two categories: intrinsic and extrinsic defects. Intrinsic defects are thermally generated in the internal or pure crystalline structure, which includes the Schottky and Frenkel defects. Using stoichiometric metal oxide MO as an example, the Schottky defects can be expressed with the Kröger–Vink notation as:

$$M_M^x + O_O^x \Leftrightarrow V_M^{''} + V_O^{\cdot\cdot} + (MO)_{defect} \qquad 2.1$$

where V_M and V_O denotes the vacancies of metal and oxygen in the lattice, $(MO)_{defect}$ represents the a lattice unit on the surface, the single point • represents a positive charge and a ' means a negative charge.

The Frenkel defect in MO can be expressed as:

$$M_M^x + V_i^x \Leftrightarrow M_i^{\cdot\cdot} + V_M^x \qquad 2.2$$

where V_i is the interstitial sites in the lattice. Frenkel defects occur normally in the metal sublattice because the metal ions are in most cases smaller than the oxygen ions in many metal oxide materials. Therefore, the metal atoms can move into the interstitial positions, leaving metal vacancies V_M^x in the crystalline structure.

However, the extrinsic defects are induced by the insertion of foreign atoms into the lattice, which results in the donor or acceptor doping states in the band gap of the materials.

By increasing defect concentration, the interaction of the defects is enhanced and the cluster of such defects can be formed locally, thereby resulting in the deviation of the stoichiometry. Therefore, such locations in materials become non-stoichiometric and can establish the extended defects. In the case of the TiO_{2-x}, it is reported that x should be no more than 0.0001 for the accommodation of the point defect. [24, 25] Greater oxygen deficiency forms the extended defects.

(b) Extended defects (dislocations and grain boundary)

Dislocations are linear misaligned defects in the crystal lattice. There are two kinds of dislocations: edge and screw dislocations. Edge dislocations result from the missing of a plane of atoms in the crystal structure. Screw dislocations are the structures with a helical path traced around the linear defect.

Grain boundary is the region where the crystallographic directions of the lattice change abruptly. They are often observed between crystals growing separately and finally meet during the deposition, for example, the regions between the neighbouring column structures of the sputtered TiO_2 thin films (see next chapter of thin film characterisation).

In this work, we study the resistance change in the MIM configurations such as Pt/TiO_2/Pt and Cu(or Ag)/TiO_2/Pt. The stoichiometry of TiO_2 can be changed, possibly to non-stoichiometric TiO_x or possibly to doped TiO_2 by Cu or Ag atoms. It is already known that a small variation of the composition of the TiO_2 such as the oxygen vacancies in the material results in a significant reduction of resistance. Even with 0.0017 at percentage of oxygen deficiency ($TiO_{1.9995}$) the conductivity increases to 10^{-1} $\Omega^{-1}cm^{-1}$, whereas the stoichiometric conductivity of single TiO_2 has a much higher conductivity at 10^{-13} $\Omega^{-1}cm^{-1}$. Much higher conductivity can be obtained by introducing more oxygen deficiency into the TiO_x, for instance, titanium (II) oxide TiO is a metallic sub-oxide and titanium (III) oxide Ti_2O_3 is a semiconducting sub-oxide. The conductivity of the non-stoichiometric TiO_x is listed in Table 2.1. [26, 27, 28]

(c) Surface states

In the surface region, the observed broken bonds greatly influence chemical reactivity. The interface between the metal and metal oxides can be complicated and is possibly related to the different interface reactions such as redox reaction, alloy formation, encapsulation and interdiffusion. [29, 30] Thus, the composition and defects in the interface region determine the electrical conduction through the interface in such MIM structures.

Table 2.1: Conductivity of the stoichiometric and non-stoichiometric TiO_2

Oxide	Conductivity
TiO_2	$< 10^{-10}\ \Omega^{-1}cm^{-1}$
$TiO_{1.9995}$	$10^{-1}\ \Omega^{-1}cm^{-1}$
$TiO_{1.995}$	$0.8\ \Omega^{-1}cm^{-1}$
$TiO_{1.75}$	$100\ \Omega^{-1}cm^{-1}$
Ti_2O_3	$0.94\ \Omega^{-1}cm^{-1}$
TiO	metallic

2.1.3 Basic electrical conduction in MIM structures

MIM- or metal oxide semiconductor (MOS)-sandwiched structures are widely applied to fabricate various micro- or nanoelectrical devices. Their electrical response under applied electrical fields are not only related to their own materials properties, but also greatly determined by the interface features between electrodes and the material surface. Whether the interface or the bulk dominates the device properties can be very different and normally depends on the material properties, sizes and preparation processes. For the wide applications of the base of thin film technologies in particular, the interface effects greatly influence the current transport. Great efforts have been made to understand the current transportation mechanisms of the devices, and several basic theories about the conduction process are listed in Table 2.2. But none alone can explain satisfactorily the conduction mechanism in thin film electronic devices. In most cases, the current transportation results from different processes according to the temperature or bias applied.

Table 2.2: Basic electrical conduction models for the current conduction in solid thin films

Conduction	**Expressions**	**Interface or bulk effect**	**Voltage and temperature dependences**
Schottky emission	$J = A^* T^2 \exp[\frac{-q(\Phi_B - \sqrt{qE/4\pi\varepsilon_0\varepsilon})}{kT}]$	Interface	$\ln J \propto \sqrt{V}$ $\ln\left(\frac{J}{T^2}\right) \propto -q(\Phi_{ac})\frac{1}{kT}$

Poole–Frenkel emission	$J \propto E \exp[\frac{-q(\Phi_B - \sqrt{qE/\pi\varepsilon_0\varepsilon})}{kT}]$	Bulk	$\ln\left(\frac{J}{V}\right) \propto \sqrt{V}$
Fowler–Nordheim emission	$J \propto E^2 \exp[-\frac{4\sqrt{2m^*}(q\Phi)^{3/2}}{3\hbar qE}\sigma(\frac{\Delta\Phi}{\Phi})]$	Interface	$\ln\left(\frac{J}{V^2}\right) \propto \frac{1}{V}$
Space charge limited	$J = \frac{9\varepsilon_0\varepsilon_r\mu_n V^2}{8d^3}$	Bulk	$J \propto V^2$
Ohmic	$J = qn\mu_n E + qp\mu_p E$	Interface, bulk	$J \propto V$
Ionic	$J \propto \sqrt{TE}\exp[(-\frac{\zeta}{2} + \sqrt{\frac{q^3E}{4\pi\varepsilon_r\varepsilon_0}})/kT]$	Bulk	
Parameters: *A** = effective Richardson constant; *T* = temperature; *q* = electron charge; Φ_B = barrier height; *E* = electrical field; ε_0 = vacuum permittivity; *ε* = dynamic permittivity; *εr* = static permittivity *m** = effective mass; *d* = thickness; μ_n = electron mobility; μ_p = hole mobility			

2.2 Resistive switching memories: mechanisms and integration structures

The non-volatile RRAM memory composites high density memory cells, which are tiny MIM structures. The resistance of such MIM cells can be programmed by appropriate electrical voltages. Two kinds of resistive switching behaviours can be distinguished – unipolar and bipolar resistive switching – as shown in Figure 2.2 (a) and (b). Unipolar resistive switching can SET (red solid line) and RESET (green solid line) both the resistance states of ON and OFF in the same bias polarity. Typically, the voltage for SET V_{ON} is always higher than the RESET voltage V_{OFF}. Current compliance (CC) is necessary here to limit the current flow through the cells. Switching OFF (erasing) the current of the unipolar resistive switching is larger than the CC for switching ON. According to unipolar resistive switching, the RESET current is in most cases typically above several mA. In the case of the bipolar resistive switching, the RESET procedure must be done under the opposite voltage bias to the SET procedure; in other words the switching event of the bipolar behaviour is polarity-dependent (Figure 2.2 (b)).

The resistance state after SET and RESET can be read out by distinguishing the magnitude of the current under a low enough voltage to avoid changing the programmed resistance states. The ratio of the high resistance state (HRS) to low resistance state (LRS) should be large enough (> 10) for device applications. In contrast to unipolar resistive switching, bipolar behaviour can occur with a much lower current, down to the nA range, which helps develop low power devices. However, unipolar resistive switching with its non-polarity dependence simplifies the control circuit.

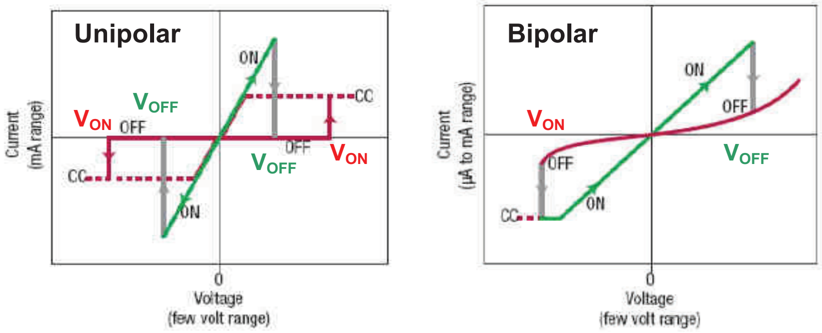

(a) (b)

Figure 2.2: Sketch of (a) unipolar and (b) bipolar resistive switching. Adapted from [31]. Red lines describe the OFF state current and can be set ON with proper bias. A CC must be set to protect the cell from breakdown by limiting the maximum current. The green line is the current of the ON state with voltage and can be switched back into the OFF state.

2.2.1 Mechanisms of resistive switching

The real mechanisms responsible for resistive switching in several materials in MIM configurations have been reported and discussed since the 1960s. According to the geometric locations where switching occurs, it can be classified into two categories: filamentary switching and area switching.

A filament is a local conduction path bridging two electrodes in the MIM structure shown in Figure 2.3 (a) and (b). [31]Generally, such conductive paths were often observed in lateral MIM structures (Figure 2.3 (b)), with no special sample preparation process for such observations. However, it is more complicated watching local filaments in the perpendicular MIM structure because of the uncertainty of the positions where these paths grow under the top electrode as well as the damage resulting during the preparation processes for measurements such as TEM. Conductive filaments are formed after electroforming or during the first SET ON operation by applying a proper electrical bias to the electrodes. Therefore, the resistance of the MIM cell is lowered because these kinds of better conductive locations dominate the property of the current transportation.

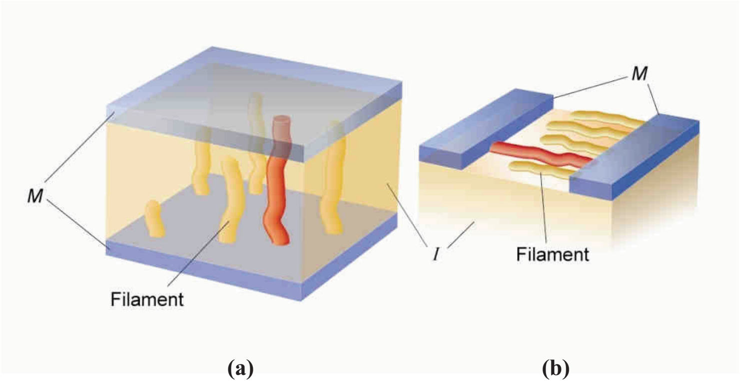

Figure 2.3: Sketch of the filamentary resistive switching in (a) perpendicular and (b) planar MIM structures. [31]

Another kind of resistive switching shows homogeneous switching under the electrodes, where the resistance of the states proves to be strongly electrode dimension dependent. Waser et al. have reviewed research developments in resistive switching phenomenon in several materials and have summarised the classifications of related mechanisms (Figure 2.4). [32] All resistive switching phenomena are triggered electrically. However, the basic principles responsible for most switchable resistances vary greatly depending on the materials and configurations of the cell.

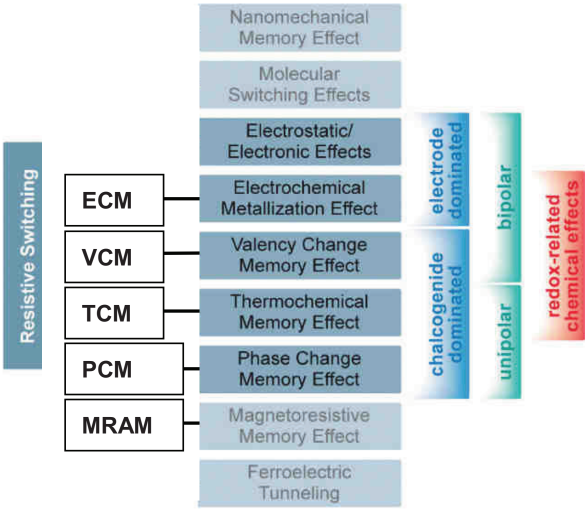

Figure 2.4: Classification of the resistive switching mechanisms (partly adapted from [32]).

Molecular switching effects can be induced by changing the molecular configuration. [33] The technology of magnetoresistive random access memory (MRAM) utilises the magnetic tunnelling effect to program the cell into two resistance states according to the magnetic orientations of two magnetic plates separated by a tunnel barrier. Ferroelectricity can also influence the tunnel current of the cell with respect to the ferroelectric polarisation of domains in the layer, which results in the two resistance states. [34] The phase change memory (PCM) changes its phase transition of the cell between the amorphous and crystalline phase with a temperature controlled by the current. Resistance also changes with its microstructures. This resistive switching based on different physical principles is not related to the switching behaviour in the TiO_2 thin film discussed in this work. Therefore, more attention is paid to the mechanisms most frequently discussed for the ongoing development of future non-volatile RAM devices.

Electrochemical metallisation effect (ECM)

The ECM is induced by electrochemical metallisation and dissolution in a solid electrolyte system, which is also called programmable metallisation cell (PMC) or conductive bridge RAM (CBRAM). In ECM memory devices one electrode is made from an electrochemically active metal such as Ag and Cu, whereas the counter electrode is normally a noble metal such as Pt, W or Au. A solid thin film is sandwiched between two metal electrodes and works as the matrix for Ag or Cu ion migrations. The resistive switching in ECM cells is schematically described in Figure 2.5. By applying a positive voltage to the Ag or Cu electrode the metal atoms are firstly ionised and then migrate towards the cathode, where the positively charged ions are reduced and electrocrystallised on the interface region between the cathode and solid electrolyte thin film. At the beginning there can be simultaneously more than one preferred position for the metallisation process. As one of fastest growing filaments comes into contact with the anode, the resistance of the cell becomes a LRS. The growth of the filament in the ECM cell is called the SET procedure. It is difficult to observe directly the growth and dissolving of the filaments in a vertical structure. However, the formation of Ag dendrite in $Ag/Ag_2S_3/Au$ was reported by Hirose and Hirose in 1976 (Figure 2.5 (a)). [35] A similar dendrite filament (Figure 2.5 (b)) was also demonstrated by Guo using water as the diffusion matrix between Ag and Pt electrodes. [36] Silver dendrite paths bridge the anode and cathode and reduce the resistance dramatically. In both examples, several silver dendrites started to grow from the cathode and continued this metallisation process until one contacted the anode. The cell remains in a LRS or ON state as long as the Ag dendrite is connected to both electrodes. With the opposite bias, the Ag dendrite begins to be electrochemically dissolved from the anode. The cell switches into a HRS as the connection between the dendrite and anode breaks, which is called the RESET procedure. During this initial stage, the current measured through the ECM cell is contributed by both electron and ion migrations. The metallisation and dissolution of the electrochemical reaction here can be expressed as follows:

$$Ag^{n+} + e^{n-} \Leftrightarrow nAg \qquad 2.3$$

The arrow in the double direction means the reversible reactions of the growth and dissolution of the Ag dendrite depending on the bias polarity applied to the cell. The same electrochemical process can take place in the solid electrolyte thin films with a Cu electrode.

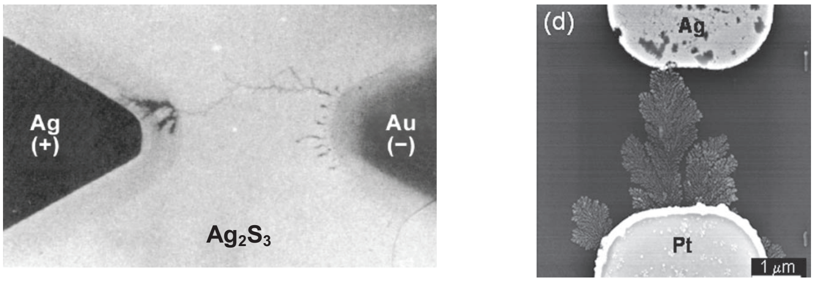

(a) (b)

Figure 2.5: Ag dendrite grown from cathode in (a) Ag_2S_3 thin film and (b) water.

Several papers have reported a resistive switching based on the ECMs in chalcogenide solid electrolyte materials such as Ag_2S, [37] GeSe, [38] Ag-doped GeSe [39] and Cu_2S. [40] Moreover, recent research has shown a similar ECM-based resistive switching in many oxide materials such as in WO_3, [41] SiO_2, [7, 42] TiO_2, [43] ZrO_2 [44] and Al_2O_3. [45] Both amorphous and crystalline thin film of such oxides exhibits bipolar resistive switching with Cu or Ag electrodes, which provides the mobile metal ions. In their virgin state, these oxides are all good insulators. Therefore, an electroforming process under a higher voltage is conducted to initiate the MIM cell to become switchable by incorporating the metal ions into the thin layer, which creates a channel for the fast ion migration in the thin film.

The significant advantages of the ECM based RRAM are very good scalability (< 20 nm), very low operation voltage ($V < 0.5$ V) and very low switching current (several μA or even in the nA range) with very high ratio of R_{OFF}/R_{ON}. It has also been reported that switching such ECM cells can be faster and consume less power by introducing conductive nanoparticles (diameter 5–8 nm) into the thin film because of the reduced migration path to form the conduction channel in the layer. [46] ECM-based resistive switching is related to nanoionics. Theoretically, the diameter of a filament can be down to atom scale, which shows a great potential to scale this kind of ECM ReRAM into several nanometer ranges. High integration density could even be realised in the future. Fast mobile Ag in solid materials can make it difficult to integrate its deposition process into the current CMOS technology. The deposition of the chalcogenide materials also arouses the concern about their dangerous impact on health.

Valence change memory effect (VCM)

Bistable resistive switching in many transition metal oxides or other related multinary oxides involves anion migration during the electroforming or switching procedures. In such materials, the oxygen vacancies have a much better mobility than the transition metal cation ions. Such positively charged oxygen vacancies drift through the defects under the applied electrical field. The accumulation or depletion of the oxygen vacancies have a significant influence on the valance state of the transition metal atoms and change the current conduction of the materials. Therefore, resistive switching involving the migrations of oxygen vacancies falls into this category.

The oxygen vacancies appear in the crystal lattice as point or extended defects. The extended defects appear when the density of the point defects increases and then accumulates to form a defect chain. For example, the concentration of point defects in $SrTiO_3$ is well below 0.1% even at high temperatures. [47] Similarly, the point defects of oxygen vacancies distribute in TiO_{2-x} with x in the order of 10^{-4}. [48, 49] Szot et al. have verified that the oxygen vacancies have a much higher mobility in dislocations than that in the regular lattice. [50] Therefore, the oxygen vacancies composed defects like dislocations or dislocation arrays in the materials can be formed during the electro-forming procedure and provide the fast ion transport channel. The related electrochemical reaction is also a called redox reaction. During forming, the reduction reactions in the cathode can be expressed as:

$$Ti^{4+} + ne^{-} \rightarrow Ti^{(4-n)+} \qquad 2.4$$

The negatively charged oxygen ions move to the anode and leave the Ti^{4+} in the cathode region reduced. In the anode, the oxygen ions are oxidised and release oxygen gas.

$$O_O \Rightarrow V_O^{\cdot\cdot} + 2e^{-} + \frac{1}{2}O_2 \qquad 2.5$$

Where O_O is the oxygen in regular site and $V_O^{\bullet\bullet}$ is the positively charged oxygen vacancy according to the Kröger–Vink notation. The oxygen vacancy-rich region moves towards the anode, which is also referred to as the virtual cathode because of the enhanced conductivity of the TiO_x. After electroforming, the bipolar resistive switching occurs through the redox electrochemical reaction between the anode and the virtual cathode. As an example, Figure 2.6 schematically represents the bipolar resistive switching process on a formed $SrTiO_3$, where the Pt tip of the conductive AFM measurement works as an anode. The dislocation channel between the anode and virtual cathode are reduced or oxidised depending on the anion migrations within the applied electric field, which reduces or increases the energy barrier and thereby results in ON (LRS) and OFF (HRS) states. Instead of the dislocation, Yang from Hewlett-Packard Laboratories proposed the Schottky-like barrier modification induced by the repelling and penetrating of the oxygen vacancies in the interface region of the Pt and virtual cathode TiO_x. [51]

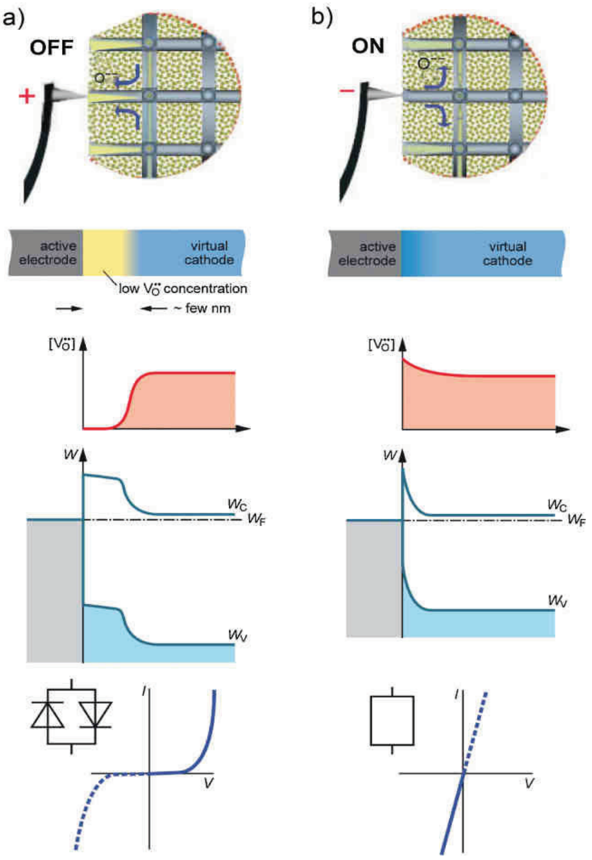

Figure 2.6: Schematic description of the bipolar switching of a formed $SrTiO_3$, resulting from the redox reaction between the anode and the virtual cathode (adapted from [52]).

The VCM effect-based resistive switching in $SrTiO_3$ and TiO_2 belongs to the filament model because of the localised oxygen vacancy channel formed after the electroforming procedure. In the VCM resistive switching category, there could also be the area-dependent resistive switching reported by Sawa, which is also called homogeneous interface switching. [53] This model is mostly reported in the interface between the electrode and semiconducting perovskite oxides such as Ti/PCMO and SRO/Nb:STO. [54, 55, 56, 57, 58, 59] The Schottky barrier dominates current conduction in the kinds of MIM cells in a virgin state. Barrier height and width have a great influence on the contact resistance of the devices, which are all dependant of the interface state including charges, defects and impurities (Figure 2.7). The electrochemical migration of the oxygen vacancies in or out near the interface changes the contact resistance significantly. The influence can be different depending on whether the semiconducting oxides are or an n- or p-type conduction. For the p-type PCMO, the induced oxygen vacancies will neutralise the acceptors and widen barrier width. Thus, the p-type conduction of the bulk is reduced, resulting in an OFF (HRS) state. By contrast, in the interface of n-type perovskite oxides such as Nb-doped STO, the oxygen vacancies as an effective donor reduce barrier width by increasing the number of oxygen vacancies, resulting in the reduction of the resistance (ON or LRS).

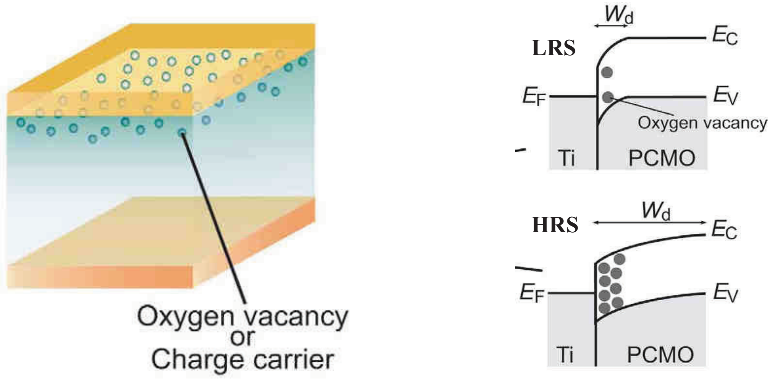

(a) **(b)**

Figure 2.7: (a) Sketch of the interface modification-induced resistive switching; b) The barrier width modified by the concentration of the oxygen vacancies in the interface of p-type PCMO (adapted from [53]).

Thermochemical memory effect (TCM)

Unipolar resistive switching, a typical example of thermochemical memory effect-related switching behaviour, is generally reported in a lot of binary TMO thin films such as TiO_2, [60, 61] NiO [62] and Al_2O_3 [63] sandwiched between inert metal electrodes such as Pt or Ru. After electroforming, their thin films can be switched reversibly between the ON and OFF states with the same voltage polarity as shown in Figure 2.2 (a). The ON state is metallic. [64] Their RESET operations are mostly above the mA range, which results in high temperatures in the fine metallic filament. The highly conductive filament comes to break as the temperature increases above the melting point of the filament. Therefore, this kind of unipolar switching is called fuse–antifuse resistive switching, where Joule heating is attributing to the breaking of the filament during the RESET procedure. The SET (switch ON) procedure can be described as a thermochemical process. The residue conductivity in the OFF state increases the temperature locally, which helps the drift of the oxygen out of the high temperature locations because of the energetically favoured lower valence states of the transition metal oxide. Yasuhara et al. have studied the valence state of the CuO_x in the filament formed in a Pt/CuO/Pt lateral MIM structure (Figure 2.8 (a)). By comparing the XAS spectra in the filament bridge (region I in red) and its neighbouring region (region II) lower valence state of the Cu was found in the filament region, indicating a reduced composition of CuO. [65]

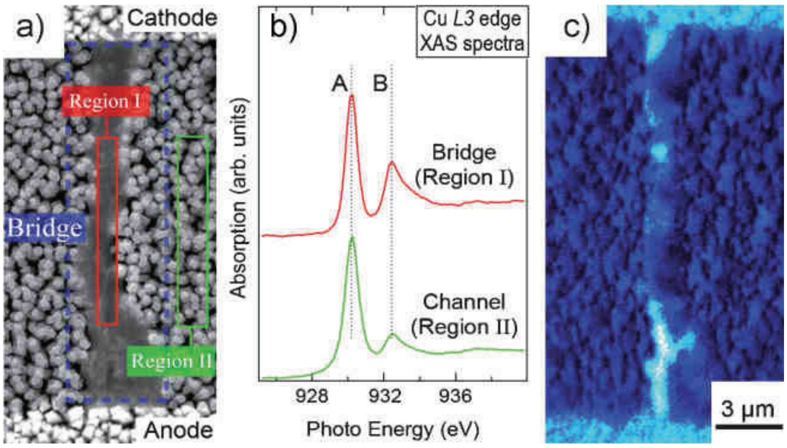

Figure 2.8: (a) SEM image of the filament formed in the CuO between two Pt electrodes; (b) XAS spectra and (c) PEEM images indicate the more Cu_2O existing in the filament (adapted from [65]).

2.2.2 Study of the resistive switching in TiO_2 thin films

TiO_2 is one of the most interesting TMO materials and has been intensively studied to understand its resistive switching mechanisms. Unipolar [12,60,61] and bipolar [13,66, 67] resistive switching are both observed in TiO_2 thin films depending on the magnitude of compliance of current and electrode materials.

Unipolar switching in TiO_2 normally switches with a very high compliance current and reset current up to 60 mA. The related mechanism for such high current unipolar switching is reported frequently as the fuse–antifuse of the metallic filaments composed of TiO_x. Jeong reported that lowering the compliance current at 1 mA after forming in the Pt/TiO_2/Pt MIM cell results in bipolar resistive switching. [12] The temperature measurement indicates the semiconductor-like current transportation at both the HRS and LRS. When the compliance current increased to more than 3 mA, unipolar switching was then triggered. The HP group has demonstrated bipolar resistive switching on the base of the 50 nm × 50 nm crossbar of Pt/TiO_2/Ti/Pt MIM structures. [25] They proposed a parallel conduction model to elucidate that the drift of the oxygen vacancies by the electrical field modifies the interface Schottky barrier height. A high concentration of oxygen vacancies near the surface collapses the Schottky barrier and forms ohmic contact there. The device turns ON. With reverse bias the oxygen vacancies will be removed backwards, and they then reduce their concentration near the interface, where the Schottky barrier is formed. The device turns OFF. Unlike the pure interface effect mentioned above, the current conduction in the HP model is decided by a group of locations with the lowest Schottky barrier. For both models – the fuse–antifuse model for common unipolar resistive switching in the Pt/TiO_2/Pt structure and the HP model for the Pt/TiO_2/Ti/Pt structure – the drift of the oxygen vacancies is considered responsible for the switching between the HRS and LRS. But the differences are also clear. The fuse–antifuse model is related to the anion migration of redox reaction as well as the thermal effect; however, the Schottky barrier-based model is purely electrical and takes place in the interface between the oxide and metal electrodes.

Cation migration-induced bipolar switching has been observed in amorphous chalcogenide glass with one electrochemically active electrode such as Ag and Cu. The switching in this combination normally occurs with a lower operation current than in Pt/TiO_2/Pt structures. Tsunoda reported the bipolar resistive switching on the Pt/TiO_2/Ag MIM cell and showed multilevel resistive switching down to 1 nA.[13] However, the LRS set by such low current switching (< 100 µA) is thermally unstable at room temperature. The metallic LRS is around 40 ohm and, as the Ag filament builds up in the TiO_2 matrix, considered similar to those in the chalcogenide materials.

2.2.3 Integration of the resistive switching memory

The two terminal resistive switching cells can be integrated into crossbar arrays. But such simple structures with only resistive switching cells in arrays have a serious problem with the so-called parasitic path. That means the current will flow through the nodes in LRSs, which makes it difficult to control the resistance states of the nodes, no matter whether they are addressed to be changed or not. This problem can be avoided by connecting an element of non-linearity to each node, either a diode (passive) or a transistor (active). Both concepts are described in Figure 2.9 (a) and (b) and are called 1R1D and 1R1T structures, where R represents the resistive switching element, D is the diode and T is the transistor. However, the additional elements in the circuit require more area in the chip and for the 1R1T even more footprints, which reduces the integration density of the memory cells of the chip and raises the complexity of the fabrication processes.

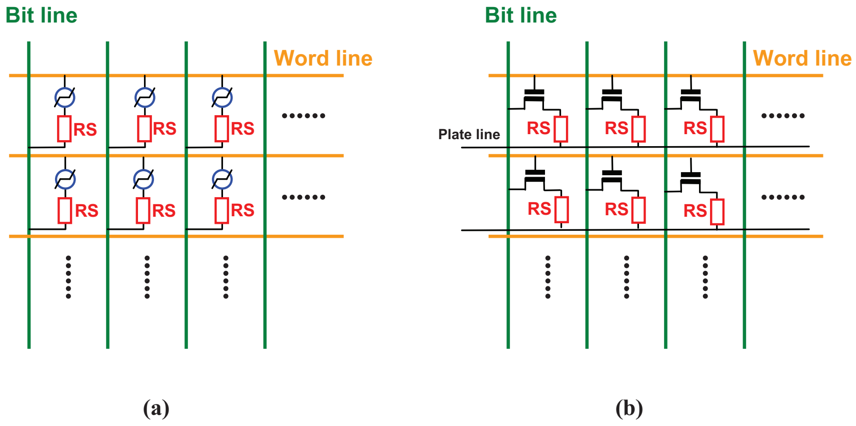

Figure 2.9: Matrix of the storage cells of the RRAM. (a) Passive matrix with a specific non-linearity element as the unit node; (b) active matrix with a transistor.

Chapter 3 Experimental

In this work, various thin film deposition techniques are used to fabricate TiO_2 and different metal electrodes thin films. TiO_2 thin films are deposited in two different ways: (1) DC magnetron reactive sputtering (sputtering for short); and (2) atomic layer deposition (ALD). The top metal electrodes are deposited using either sputtering (Pt) or evaporation (Cu, Ag and Pt) processes.

3.1 Fabrication methods

3.1.1 DC magnetron reactive sputtering

In this work, TiO_2 and Pt thin films are prepared using a Leybold Univex 450C magnetron reactive sputtering system, which has five chambers for the deposition of different materials. Figure 3.1 describes the sputtering system and the deposition process for the TiO_2 layer on the substrate in the $Ar+O_2$ mixture atmosphere. Argon ions Ar^+ are generated in the Ar plasma by a DC voltage applied between the cathode target and the anode. They are accelerated in the electric field and transfer the kinetic energy to the cathode, from which Ti atoms are emitted and move towards the substrate. The Ti atoms react with the O_2 and then reach the substrate surface or the earlier deposited TiO_2 surface. Pt top electrodes are deposited in the Ar atmosphere without reaction. The thickness of the TiO_2 thin film can be defined by changing the process time with a constant deposition rate of 1.8 nm/minute under the given conditions as shown in Table 3.1 for TiO_2. No oxygen gas is used to deposit Pt thin films at a much higher growth rate of 108 nm/minute than that for TiO_2 thin films. Every sputtering chamber is separated from the central transfer room with a shutter during the deposition process. Therefore, each target is protected from possible contamination by foreign particles or gases. However, it is still necessary that a pre-sputtering process is conducted to clean up the target surface from contamination or oxidisation before the deposition starts. A cooling system with cold water is built under the sample holder (Figure 3.1 (b)) to prevent the substrate overheating. Because of the slow growth rate for TiO_2 thin films with this system, the temperature on the sample still increases over time. The temperature of the sample can be more than $100^{o}C$ for the deposition of 27 and 54 nm TiO_2.

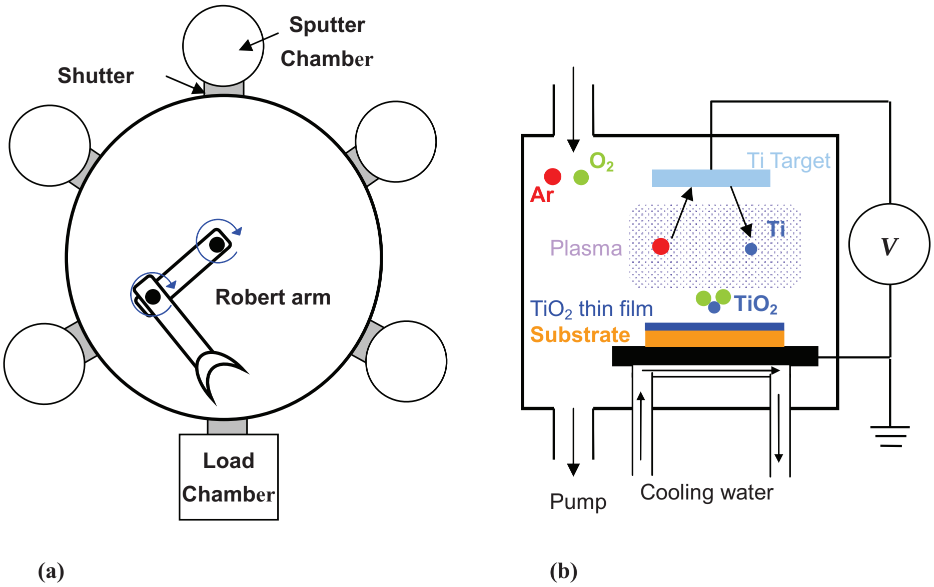

Figure 3.1: Schematic of (a) the DC magnetron reactive sputtering system and (b) the process of the TiO_2 deposition in the chamber.

Table 3.1: Sputtering parameters for TiO_2 and Pt thin films

	TiO_2	Pt
Working pressure	2.2×10^{-2} mbar	1.35×10^{-2} mbar
Gas composition	77% Ar + 23% O_2	Ar
Power	300 W	375 W
Temperature	Room temperature	Room temperature
Deposition rate	1.8 nm/minute	108 nm/minute

3.1.2 Atomic layer deposition

The ALD process is a chemical vapour deposition (CVD) technique. With the ALD process it is possible to fabricate highly conformal thin layers with a thickness down to single atomic scale on extremely complex surface structures. Various types of materials can be deposited by ALD such as gate oxides for CMOS technology, [68] capacitor dielectrics of dynamic random access memory (DRAM) [69] and transition metal nitrides for use as metal barriers and gate metals. [70] Because of the ongoing perspective of scaling down the devices into the nanometer range, the ALD process now has a wide range of applications through its own technical advantages. Intel has reported the fabrication of a high *k* gate dielectric by using this technique for its 45 nm CMOS technology.

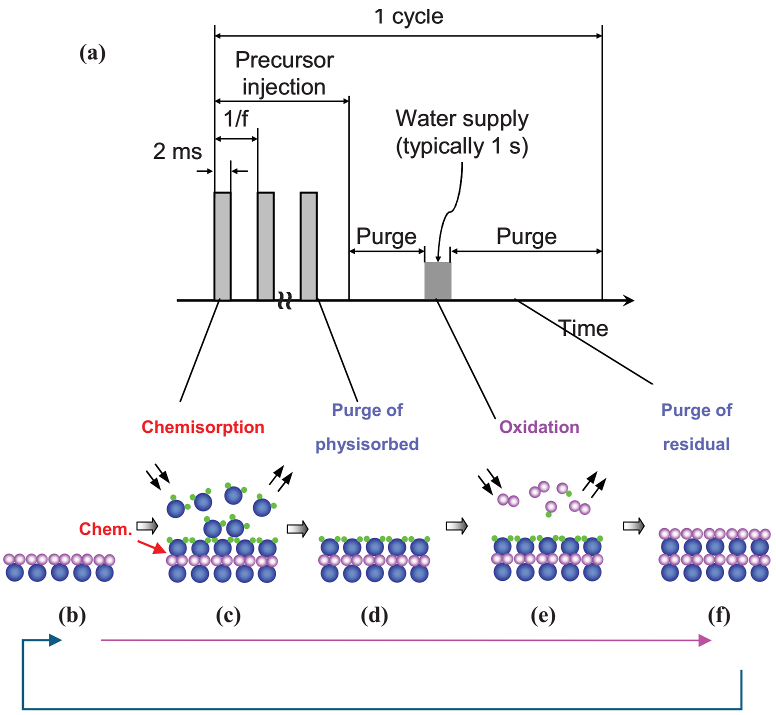

Figure 3.2: Principle of the atom layer deposition procedure: (a) gas pulse of single cycle; (b) one single TiO_2 layer already formed on the substrate; (c) exposure of the precursor TTIP; (d) removing the non-reacted precursor by purging the reaction chamber; (e) reaction of the deposited precursor with oxidant water; (f) the second TiO_2 single layer formed after purge.

ALD can be defined as a sequential self-limiting surface reaction controlled process that leads to homogeneity and thickness control on complex surface structures. In this study, precursor $Ti[OCH(CH3)_2]_4$ (titanium tetraisopropoxide, TTIP) was used because of its high vapour pressure, lack of corrosive by-products and high cost efficiency compared with other halide or metalorganic precursors. TTIP is first to be dissolved and diluted in an ethylcyclohexane (ECH) solvent at a precisely defined concentration. Thus, the amount of injected TTIP molecules in a single deposition cycle can be controlled by setting the number of injections. One single deposition cycle supplies precursor, reactants and inert gas sequentially into the reaction chamber at 240 ^{o}C, where TiO_2 will be deposited on a one inch square substrate. Figure 3.2 (a) indicates the programmed gas pulse in a single cycle. The general procedure of the deposition of ALD TiO_2 is illustrated in Figure 3.2 (b), (c), (d), (e) and (f). The TTIP precursor is injected and a chemisorption reaction occurs between the precursor and substrate surface until the surface is passivated (b, c, d) because TTIP does not react by itself. Therefore, TTIP terminates the reaction as the surface is fully covered by a single atomic layer. The unreacted extra precursor and reaction by-product are removed by Ar. Next, water is injected into the chamber and this reacts with the dangling isopropoxy ligand [–OCH(CH_3)$_2$] on the new surface, forming titanium oxygen (Ti-O) bridges (e). Therefore, a single layer of TiO_2 is homogeneously deposited on the surface. Again, the Ar gas brings the reaction by-product and the rest of the water out of the reaction chamber, and the next deposition cycle starts by repeating the same programmed injection and purge process. In this way, the thickness can be precisely controlled by the sequential cycles. The self-limiting growth character results not only in the precisely controlling the thickness but also a homogenous composition on complex structures, if multinary oxides are fabricated with this technique.

3.1.3 Evaporation

In this work, metallic electrodes were deposited by two different evaporation methods: thermal evaporation and electron beam evaporation (Figure 3.3 (a) and (b)).

The materials were heated on a Tantalus (Ta) boot working as an electrical resistance heater by applying proper voltage. The materials were melted and evaporated into the vacuum and then allowed to condensate on the substrates. The high vacuum of only 10^{-6} mbar reduced the possible scattering and reacting of the evaporated metal atoms with other gas phases in the chamber and avoided contamination from previously deposited materials on the chamber wall. The deposition rate was controlled by setting the voltage on the Ta boot to control the current flow. In this way, thin films such as Ag, Cu, Au and Al can be fabricated because of their lower melting temperatures.

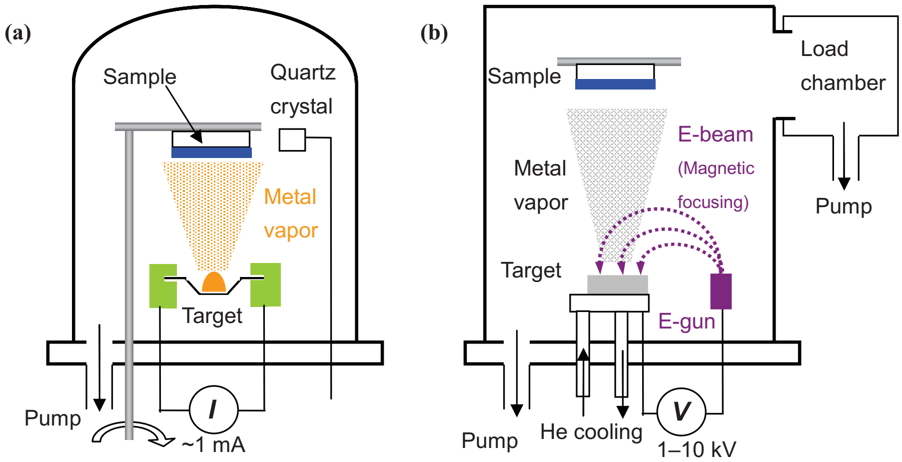

Figure 3.3: Schematic of (a) thermal evaporation and (b) electron beam evaporation.

Metals such as Pt, W, Ta, Ti and some oxides, which are melted at much higher temperatures, can be deposited using electron beam evaporation. This process is schematically shown in Figure 3.3 (b). A high energetic electron beam is emitted from an electron gun by applying a high voltage (between 1 and 10 kV). The electron beam is magnetically focused on the target to avoid exposing the electron beam gun directly to the material vapour. The material of the target is heated under the high energy electron beam and locally evaporated and deposited on the substrate above the target.

3.1.4 Microstructuring

Optical lithography is a widely used technology for manufacturing microstructures on substrate or thin films. The light transforms the pattern from the mask to the photo sensitive photoresist deposited on the sample. In our work, we used the 320 nm UV lithography process to prepare structures down to 1 µm (size of a wafer).

The optical lithography process is schematically illustrated in Figure 3.4, and aims to apply the processes of deposition (left) and etching (right) to the selected regions on the thin film. Firstly, the positive photoresist is coated homogeneously on the substrate to a certain thickness depending on spin parameters such as time and speed of the spinning machine. A pre-exposure bake is necessary to remove solvents in the resist at 90°C for 5 minutes. The regions on the photoresist exposed under the UV light for 13.5 seconds through a gas mask with dark Cr structures become more soluble than the unexposed area. Post-exposure baking at 120 °C for 60 seconds and a second exposure without the mask reverse the solubility of the exposed pattered areas during the first exposure, which then become insoluble. By contrast, the unexposed region in the first exposure becomes soluble and can be removed in the developer. Afterwards, a deposition process such as evaporation or sputtering brings the metal thin film onto the whole wafer no matter whether it is free from resist or not. In the lift-off process, the wafer pattered with photoresist is firstly immersed in acetone solution for a certain duration where the photoresist dissolves away and only the metal thin film on the patterned region without photoresist is left.

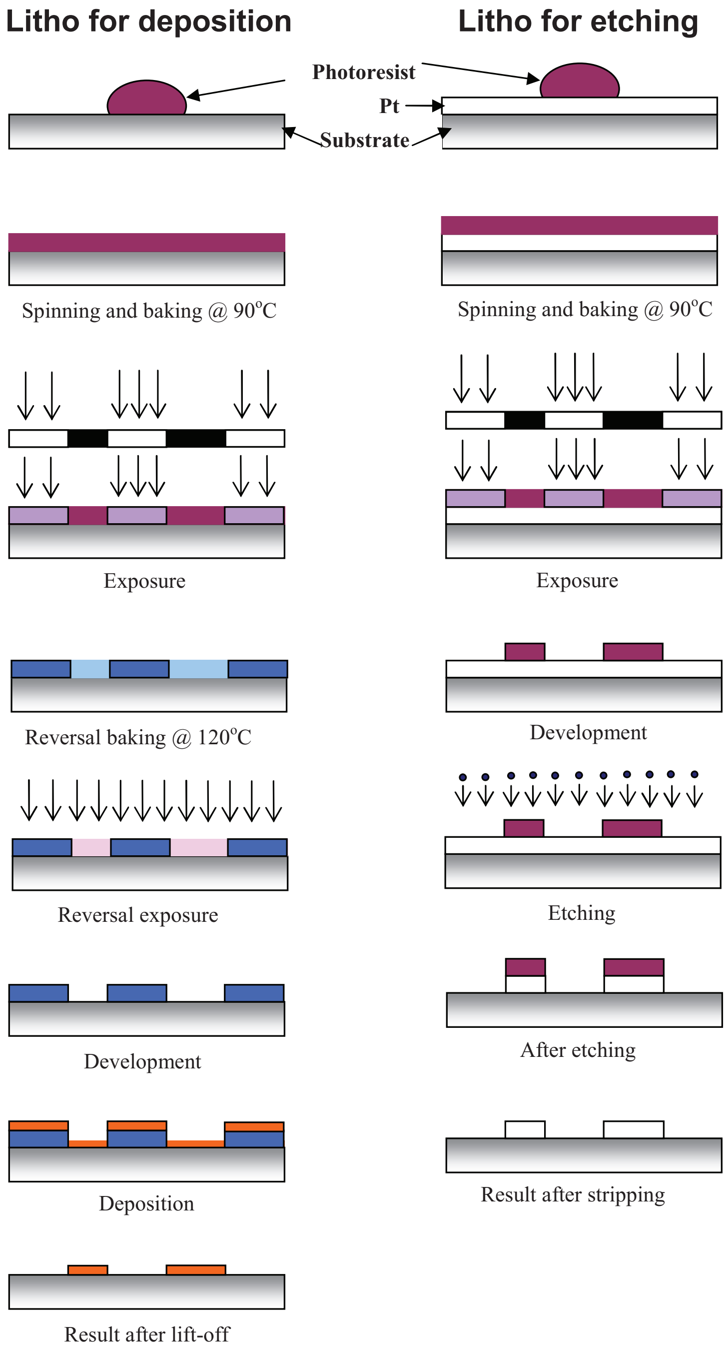

Figure 3.4: UV lithography processes for deposition and etching.

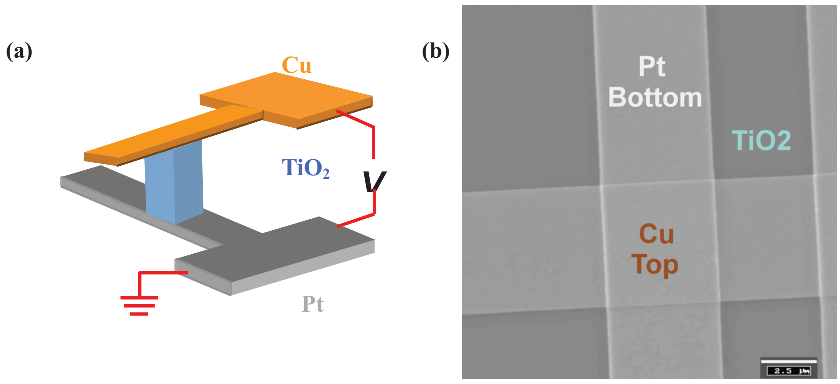

Figure 3.5: (a) Schematic crossbar structure concerned; (b) SEM image of a cross point (5 μm × 5 μm).

3.2 Characterisation methods

3.2.1 Conductive atomic force microscopy (CAFM)

CAFM is one of the special modes of the common AFM, which enables high resolution measurements of surface properties and current distribution simultaneously. The principal of the CAFM measurements is shown in Figure 3.6. In this work, a Jeol JSPM 4210A was used to measure the local current conductivity on the TiO_2 surface in the vacuum of 10^{-5} mbar. Using the contact mode, the CAFM records the local current through the Pt-coated tip (radius ~10 nm) and the sample under a constant voltage. Normally, the tip is grounded while the positive voltage is applied to the bottom electrode of the sample. This configuration enables a higher sensitivity of the current measurement because the electrons are injected from the negatively biased sharp tip. The measurement from the back side of the sample (bottom electrode) can be noisier because of the capacitive effect over the large area, especially on thin films with poor conductivity.

CAFM is a convenient method to measure the local conductivity and surface topography simultaneously with very high resolution down to several nanometer scales. In this work, it is used to measure the sputtering and ALD TiO_2 thin films. The results will be shown in Chapters 4, 5 and 6.

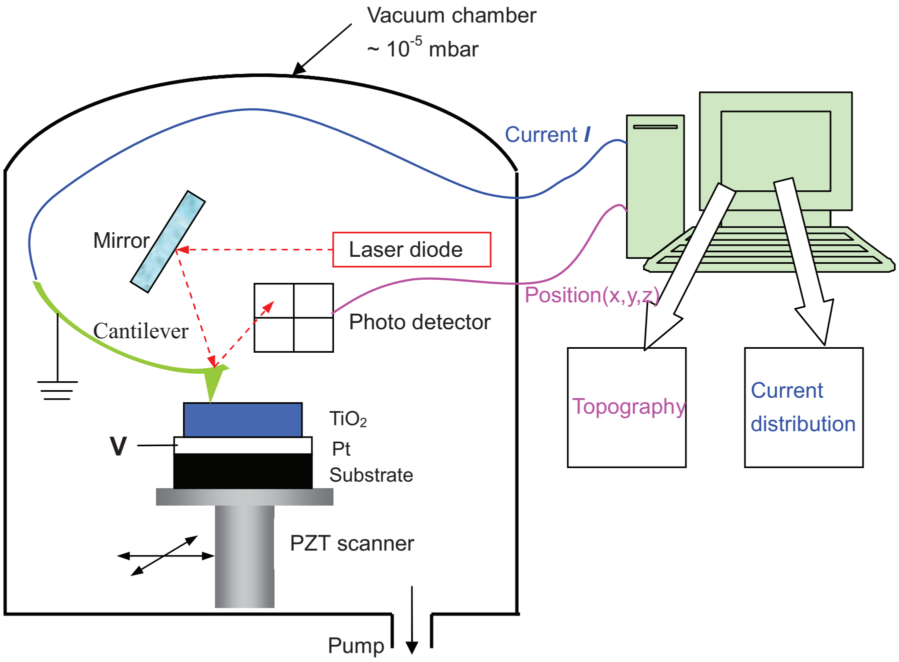

Figure 3.6: Schematic of the CAFM measurement principal.

Chapter 4 Material characterizations

The deposited thin films of both sputtering and ALD TiO_2 were characterised with different methods to obtain the information about the chemical, microstructure and the local electrical conductions.

4.1 Characterisation of the sputtered TiO_2 thin films

The crystalline structure of the sputtered TiO_2 thin film on Pt substrate was analysed by X-ray diffraction (XRD) [71] scanning electron microscopy (SEM) and transmission electron microscopy (TEM). Both images of the cross-section on TiO_2 samples show polycrystalline characteristics in Figure 4.1 (a) and (b) respectively. In picture (a), the column structure can be clearly identified with a uniform diameter of ~12 nm. Generally, every bump corresponded to a column structure. The surface is rough because of the corrugation topography on the parallel grown columns. Grain boundaries between neighbouring columns can be easily indentified. The composition of the sputtered TiO_2 thin film on the platinised substrate is illustrated in Figure 4.1 (c). The carbon signal near the TiO_2 surface region can be detected, which can be introduced during the cleaning process with acceton before the Tof-SIMS analysis.

The surface morphology and the local conductivity (down to nanometer scale) can be measured by scanning with –1 V on the tip of the sputtered TiO_2 thin film by CAFM simultaneously as shown in Figure 4.2 (a) and (b). The wave-like corrugation on the surface in Figure 4.2 (b) can be regarded as the top form of the parallel grown column structures according to the SEM and TEM images in Figure 4.1 (a) and (b). The grain boundaries can be identified between two adjacent columns directly with SEM and TEM images, which are normally located in the deep groove in the AFM images. Based on the current image in Figure 4.2 (b), the conductivity of the single columns is different from each other: some are more conductive, whereas some are not. By contrast, the grain boundaries are not more conductive than the columns themselves. The columns indicated with blue arrows have a better current conduction than the interface region between the two neighbouring columns. Figure 4.2 (c) and (d) are the morphology and the current image scanned with –4 V on the tip of the same sample. Higher scan voltage helps confirm the higher conductivity in the columns than in the boundaries (Figure 4.2 (c)).

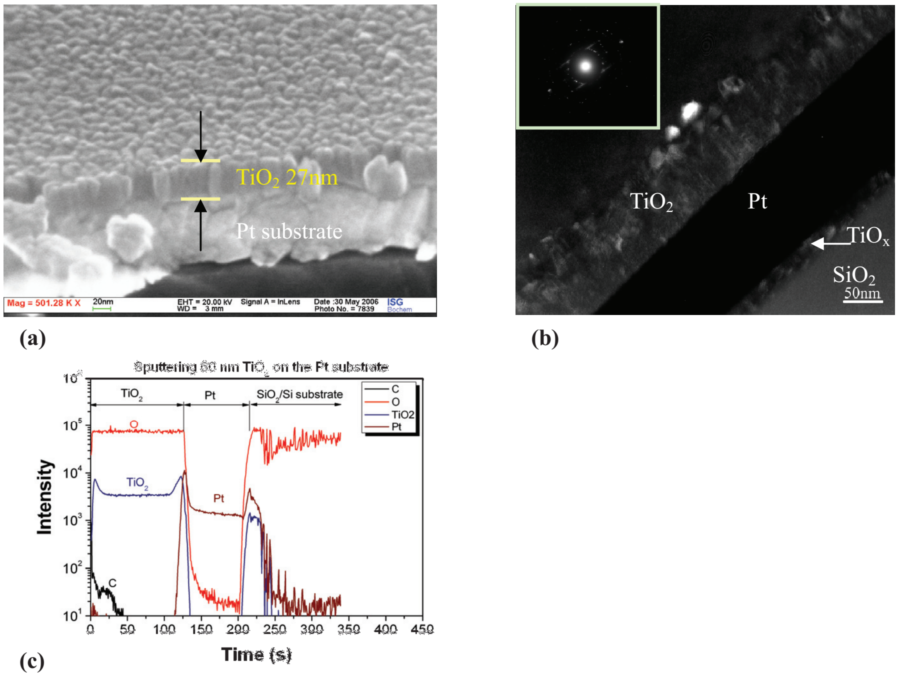

(a) **(b)**

(c)

Figure 4.1: Film characterisation of the sputtered TiO_2 on Pt substrate. (a) SEM cross section of a sample with 27 nm TiO_2; (b)TEM image of a sample with 60 nm TiO_2 and corresponding SAED pattern (inset); (c) Tof-SIMS analysis of a sputtered TiO_2 layer of 60 nm.

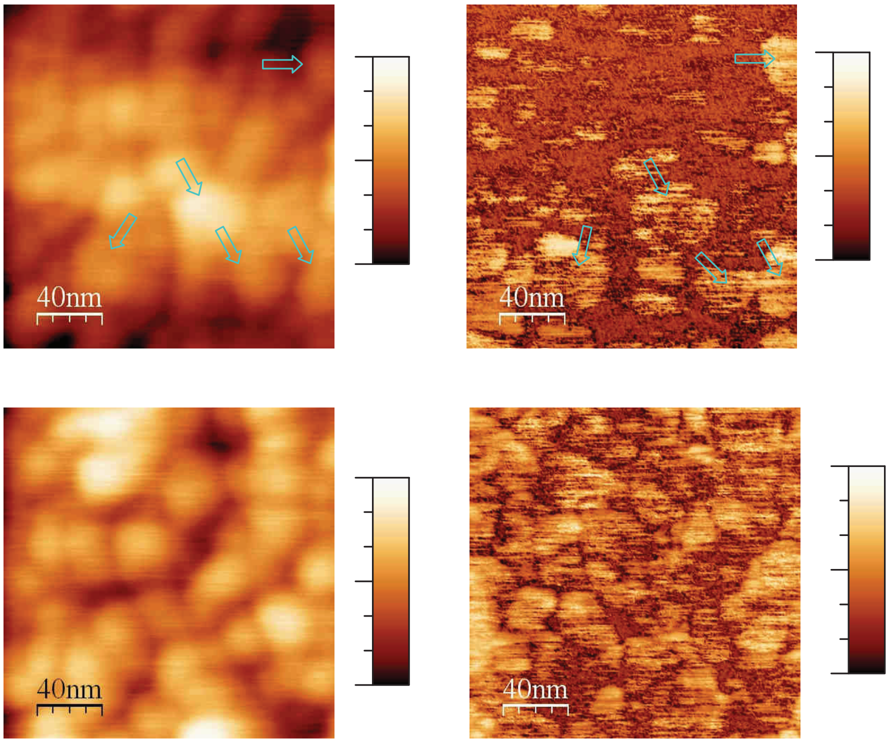

Figure 4.2: CAFM measurements on the 54 nm TiO_2 thin film on the Pt substrate. (a) Morphology; (b) current image scanned with –1 V on the tip; (c) morphology and (d) current image scanned with –4 V on the tip.

4.2 Characterisation of the ALD TiO_2 thin films

The cross-section of the ALD TiO_2 thin film was analysed with SEM and TEM as shown in Figure 4.3 (a) and (b). The SEM image of Figure 4.3 (a) shows no clear crystalline structures and much more smooth surface quality than the sputtered TiO_2 thin films as shown above. However, the TEM image of the same ALD TiO_2 with top Cu electrode in Figure 4.3 (b) indicates the fine polycrystalline structures orientating in almost every direction according to the light diffraction rings of the phase 110, 200 and 220 in the SAED picture. In contrast to the SAED picture, the inset of Figure 4.1 (b) has fewer diffraction points, indicating a better orientated and less crystalline phase in the sputtered TiO_2 thin film. The composition of the ALD TiO_2 is more complex than that of the sputtered TiO_2 according to the Tof-SIMS results in Figure 4.3 (c), which contains higher C, S, F and Cl in the layer. These foreign chemical elements occur because if the rest chemical composition from the precursor during deposition.

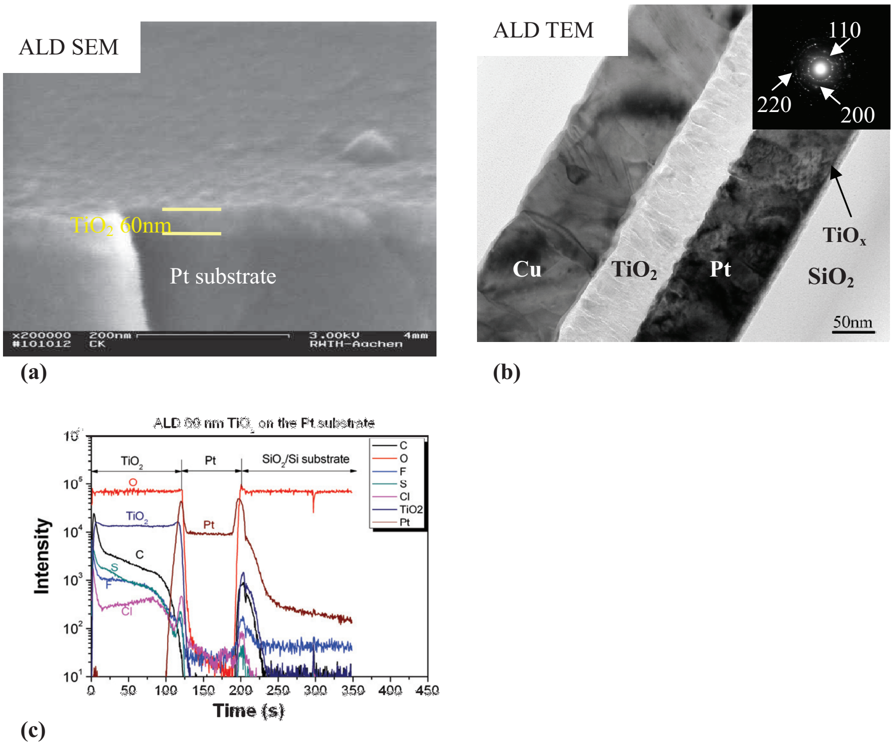

(a)

(b)

(c)

Figure 4.3: Film characterisation of the ALD TiO_2 on Pt substrate. (a) SEM cross-section of a sample with 60 nm TiO_2; (b) TEM image of a sample with 60 nm TiO_2 and corresponding SAED pattern (inset); (c) Tof-SIMS analysis of a sputtered TiO_2 layer of 60 nm.

Poor but homogeneous local current conductivity on the ALD TiO_2 thin film (Figure 4.4 (b) and (d)) is found by CAFM measurements compared with that on the sputtered TiO_2 thin film (Figure 4.2 (b) and (d)). A scanning voltage of –1 V on the tip of the ALD thin film shows uniform but low local current (no more than 400 pA), as shown in Figure 4.4 (b), whereas it can be as large as 9.5 nA in the sputtered TiO_2. Even with a much higher scanning voltage (–7 V on the ALD TiO_2), the local conductivity is not only uniform but also very low (no more than 2.45 nA; Figure 4.4 (d)), which is much lower than that on the sputtered TiO_2 thin film scanned with –4 V on the tip shown in Figure 4.2 (d).

The morphology of the ALD TiO_2 thin film measured by CAFM shows a smooth surface with an RMS around 0.59 nm, which is much lower than that on the sputtered TiO_2 with an RMS of 1.97 nm. However, the dimension of the surface corrugation of both ALD and sputtered TiO_2 is similar no matter their morphology or current images.

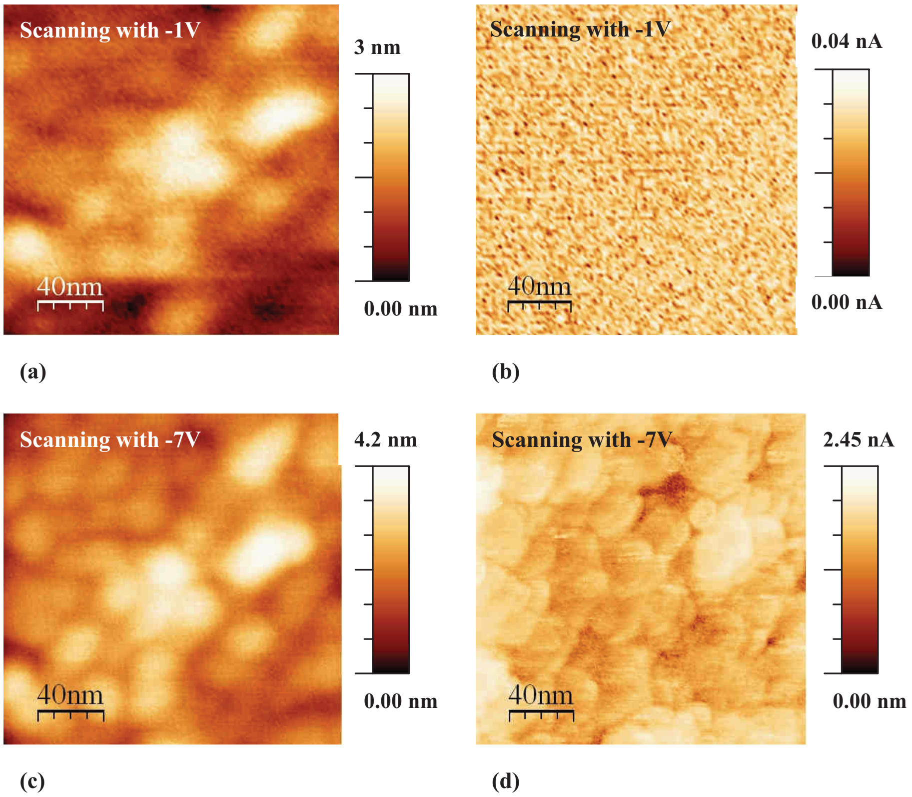

Figure 4.4: CAFM measurements on the 60 nm TiO_2 thin film of the Pt substrate. (a) Morphology; (b) current image scanned with –1 V on the tip; (c) morphology; (d) current image scanned with –7 V on the tip.

Chapter 5 Resistive switching in Pt/TiO_2/Pt structures

50 nm thick TiO_2 thin films were deposited on a 30 nm thin platinized SiO_2/Si substrate by DC magnetron reactive sputtering. Electro-forming is needed to initiate the cell to perform resistive switching. A brief introduction on the forming process is first discussed with reference to the literature. Current-controlled electro-forming was used to form Pt/TiO_2/Pt stack cells. Both unipolar and bipolar resistive switching were observed and both switching modes could be reversed by setting the proper current compliance. Bubbles were created on the top pt electrode during the forming or switching procedure under a positive bias. A Pt-coated tip of Conductive AFM worked as a mobile top electrode with a very fine diameter down to 10 nm. The experiments give a better understanding of nano-scale switching properties.

5.1 Electro-forming of Pt/TiO_2/Pt MIM structures

5.1.1 Electro-forming theory

Most transition metal oxides sandwiched between two metal electrodes have first to be “electrically formed” by applying the proper electrical voltage or current before the sample is capable of initiating resistive switching. During the forming process, some chemical or structural changes take place in the oxide layer. For decades, the mechanisms of electro-forming have been investigated but, until now, this phenomenon has not been well understood. Various models have been proposed on the basis of different material and structure systems. Either uniformly or locally reversible resistance degradation can occur and is believed to be a defect-related phenomenon in the interface region or in the bulk. Depending on the sources of the defects, the forming can be classified into the following two categories: intrinsic defects and extrinsic defects.

In the case of resistive switching in the Pt/TiO_2/Pt stack system, intrinsic defects in the form of oxygen vacancies play a significant role. Greene suggested that a high-field electrolytic process is responsible for electro-forming, during which the anion vacancies are injected into the insulator.[72] The electrochemical reaction in such metal oxide insulator MO_x near both the anode and cathode can be described as follows:

$$O^{2-} \rightarrow O + 2e^{-} (anode)$$
$$M^{2x+} + xe^{-} \rightarrow M^{x} (cathode) \qquad 5.1$$

This process is illustrated in Figure 5.1 (a)–(c), where the negatively charged *O* ions migrate from the cathode to the anode to form the conductive path composed of oxygen vacancies in the bulk until they reach the anode. At the same time, the *O* ions release electrons at the anode and form O_2 in the interface region. Bubbles of oxygen could be released under the Pt electrode during forming and resistive switching.

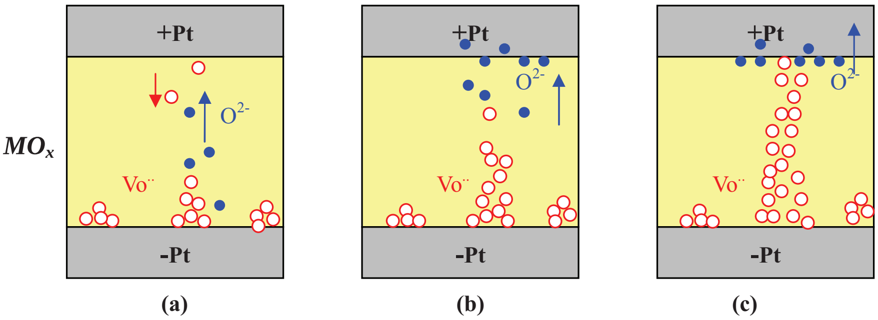

Figure 5.1: Sketch of the electro-forming process: the filaments grow by intrinsic ion migration under effect of the electric field.

Such electro-forming processes can occur either at certain locations or at sites distributed homogeneously over the substrate. For a local forming model, Dearnaley suggested that local filaments are formed by defects chains such as oxygen vacancies. Since the interface between the anode and insulator is not always smooth, the surface roughness causes some sharp locations, resulting in particularly high electrical fields there. Thus, forming can start from these positions and give rise to the growth of conducting filaments. At the beginning, there could be several similar positions on the cathode where the accumulation of oxygen vacancies grows simultaneously as shown in Figure 5.1 (a). The development of columns of oxygen vacancies in the direction of the anode can act like a moving cathode because of their much better conductivity than the virgin TiO_2. The continuous reduction of the distance between such a virtual cathode and the anode causes the local electrical field on the top of the growing paths to continually increase. Therefore the growth process is accelerated until one of the filaments reaches the anode first (Figure 5.1 (c)). The chain in the middle corresponds to a grown conduction path composed of oxygen vacancies. This chain could be metallic or semiconducting depending on the density of vacancies in the filament.

The resistive switching phenomenon has been investigated intensively for potential applications in new non-volatile memory devices. New evidence shows that the switching is an inhomogeneous phenomenon which takes place in a localized volume after the forming process. Recently, using conductive atomic force microscopy

(CAFM), the local conductivity in the film has been observed directly and characterized with nm resolution. Filaments in TiO_2 and Al_2O_3 after removal of the top electrodes from pads already in low resistance and high resistance states, respectively, have been reported. [60, 73] Due to the fact that the forming procedure is the initial step for resistive switching in many materials, forming can also be considered to be a localized process for the growth of filaments. On the basis of an investigation of binary TMO materials, the Greene model which combines the Dearnaley´s filametary model provides a good explanation of the forming process in this material system. It should be noted here that TMO with easy mobile ions like Ag and Cu could introduce a different phenomenon and therefore other mechanisms, as will be discussed in the next chapter. In this chapter only TiO_2 with Pt electrodes on both sides are considered.

5.1.2 Current-controlled electro-forming of Pt/TiO_2/Pt

Electro-forming can be done in one of two modes, with voltage-controlled or current-controlled set-ups. The current must be limited to its compliance value during a voltage-controlled forming process in order to protect the sample from breakdown. When the current produced by the applied voltage exceeds the set value of the compliance current, the voltage is limited in current-controlled mode until the measured voltage is less than the running programmed sweep voltage. The most significant drawback of the voltage-controlled process is that a larger number of swept forming cycles are needed if the compliance current is not set at a high enough level. Very often, the electrical conductivity of the cell changes after one or more unsuccessful swept forming cycles, which makes it difficult to understand the results in order to study the important parameters influencing the forming process.

In this work, current-induced electro-forming is used to initiate resistive switching of MIM cells. The sample is a Pt-TiO_2-Pt structure, with a sputter-deposited 50 nm TiO_2 layer sandwiched between Pt electrodes, including a 150 µm diameter top Pt electrode, as shown in Figure 5.2 (a). The current-controlled forming process is illustrated in Figure 5.2 (b), where the current is increased at a rate of 10 µA/step with a delay time of 500 ms, which means that the current is held for 500 ms during every step, before being ramped up to the next step with current increments of 10 µA. No voltage compliance was used in this measurement as long as this didn't destroy the sample. Normally the voltage increases with current as shown in Figure 5.2 (c). Forming occurs at around 650 µA when the voltage drops abruptly from 5 V to 0.112 V. A very low resistance of 177 Ω can be calculated according to a linearly increasing $V(I)$ characteristic after forming. This very low resistance state can be reversed back to a HRS by applying the correct negative voltage, as shown in Figure 5.2 (d). This kind of forming process, which initiates a process which transforms the cell from a virgin insulator into a device which is switchable between two resistance states, is also known as "soft break down". In contrast, so-called "hard breakdown" refers to permanent degradation of the resistance or destruction of the MIM cell.

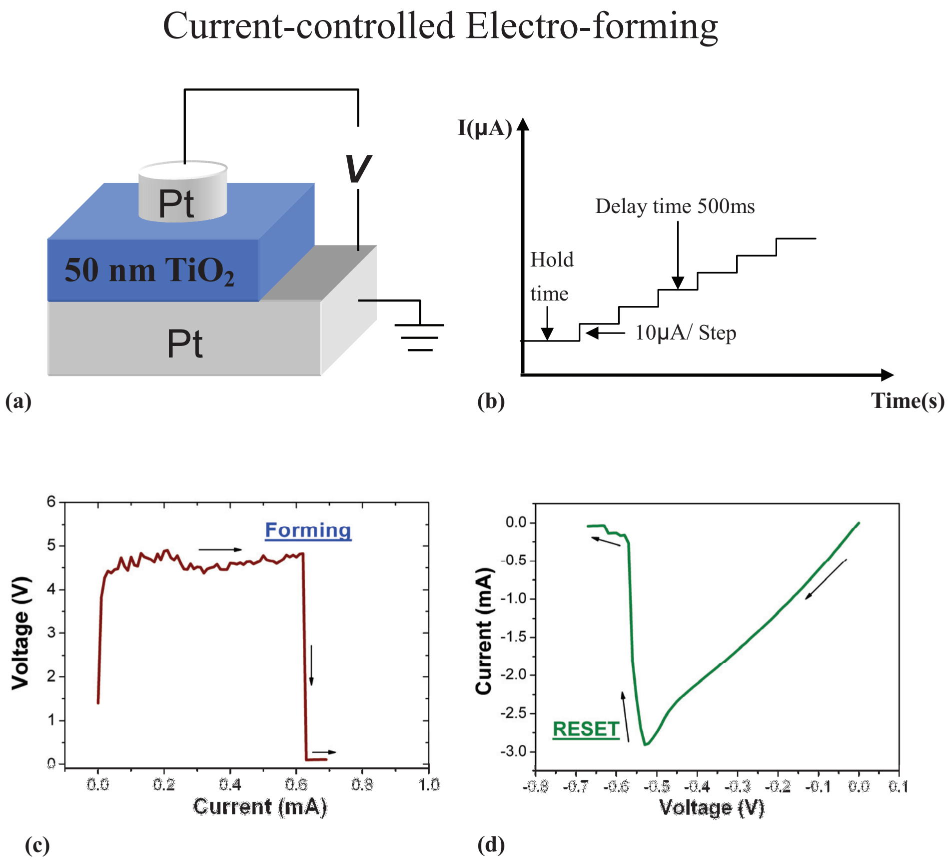

Figure 5.2: (a) Sample and measurement configurations. The top electrode has a diameter of 150 µm and the thickness of the TiO_2 is 50 nm. (b) Set-up for current-controlled forming; (c) Current-induced forming (from initial state to LRS); (c) Voltage-controlled RESET (LRS to HRS).

5.2 Switching behaviour and structure change

5.2.1 Unipolar and bipolar resistive switching

The resistive switching phenomenon in the transition metal oxide TiO_2 has been intensively investigated for potential applications in new non-volatile memory devices. [12, 60, 74, 75] Unipolar resistive switching has been observed very frequently. The most significant character is the polar nature which is independent of SET and RESET operations. Both switching ON and switch OFF can be done by applying either a positive or negative voltage of the proper magnitude. In TiO_2 thin films, very high currents (> 10 mA) are normally necessary for the RESET operation (LRS to HRS). A typical example of unipolar resistive switching measured on a $Pt/TiO_2/Pt$ stack cell is shown in Figure 5.3 (a), where SET and RESET can be repeatedly conducted for 30 cycles at both negative (orange) and positive (blue) voltages. Figure 5.3 (b) depicts the resistance values at ±0.1 V of both HRS and LRS "reads" from the 30 continuous unipolar resistive switching cycles that have already been shown in Figure 5.3 (a). The blue full and blue empty squares represent the HRS and LRS taken from positive voltage unipolar resistive switching cycles, respectively. The orange full and orange empty triangles are the HRS and LRS for negative voltage unipolar resistive switching cycles. Both HRS and LRS remain almost constant for all cycles, no matter which voltage polarity is applied. The LRS is very low to 25 Ω, whereas the HRS is much higher at 0.1 MΩ. The ratio of HRS to LRS is approx. 4000. In Figure 5.3 (c), all SET and RESET voltages are plotted for unipolar switching cycles with both polarities, positively biased switching in blue and negatively biased switching in orange. The RESET voltage for both polarities is almost identical at ±0.7 V. The SET voltage is around -2.5 V for negatively biased switching cycles, whereas switching with a positively biased voltage shows that the SET voltage has larger fluctuations between 1 V and 2 V.

Jeong reports that both bipolar and unipolar resistive switching can be initiated in $Pt/TiO_2/Pt$ stack cells by setting the right compliance current after the forming procedure. [12] Bipolar resistive switching is characterised by a dependence of the resistance transformation on the polarity of the applied voltage. The current compliance for forming is lower than 0.1 mA to induce bipolar resistive switching and, with a larger compliance current at 1 mA, unipolar resistive switching can be initiated. Secondly the report points out that bipolar resistive switching can be changed to unipolar resistive switching by applying a larger compliance current in the SET procedure, but such a change is irreversible. However some differences were found in this work compared to the above mentioned observations:

Current-controlled forming is needed to initiate unipolar or bipolar resistive switching behaviour in the same cells. Whether bipolar or unipolar resistive switching appears is just a matter of the current compliance in the SET step.

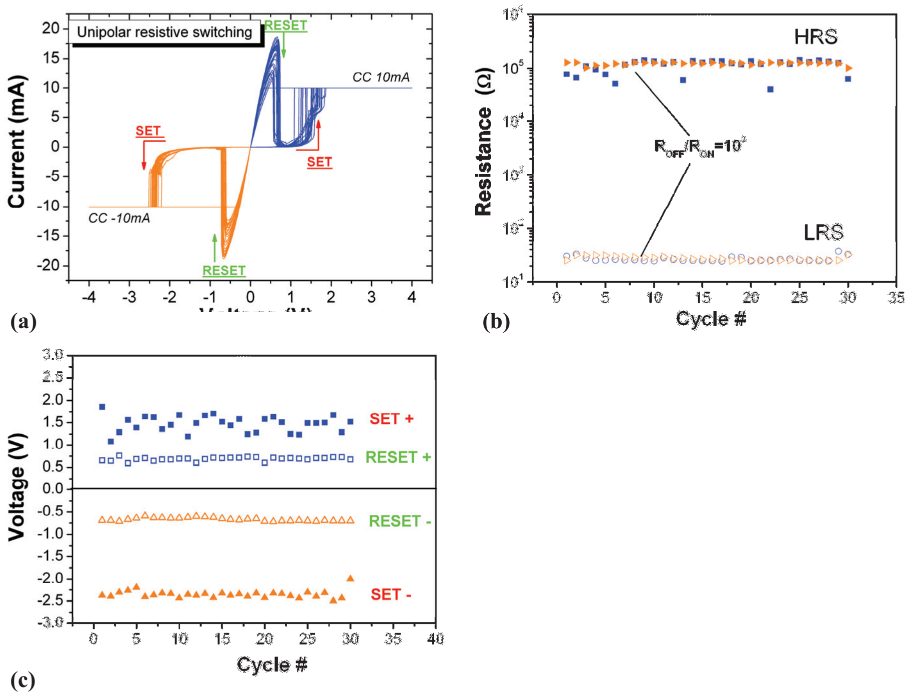

Figure 5.3: Unipolar resistive switching on Pt/TiO$_2$/Pt stack cells. (a) Unipolar switching for both polarities; (b) Resistance in both HRS and LRS states taken from the switching curve in (a) at 0.1V. (c) SET and RESET voltage of the 30 sequential switching cycles for both voltage polarities.

The change from bipolar to unipolar switching is reversible. Figures 5.4 (a) and (b) depict, respectively, the *I*(*V*) and *R*(*V*) characteristics measured during 5 continuous swept cycles of unipolar resistive switching to both polarities with 5 mA current compliance. The SET voltages varied from cycle to cycle, but the RESET voltages were very close at around ±0.8 V. The resistances in the HRS at ±0.1 V ranged between 10 kΩ to 100 kΩ, whereas the resistances in the LRS at ±0.1 V were very similar abd about 34 Ω. The real resistance of the cell in the LRS is 14 Ω if the resistance (+20 Ω) of the direct contact between the two measurement needles on the Pt electrode is taken into account. The ratio of R_{OFF}/R_{ON} was therefore ~ 3000. Repetitive bipolar resistive switching cycles using 200 μA compliance current before (black) and after (red) unipolar resistive switching cycles are shown in Figures 5.4 (c) and (d). The arrows with numbers indicate the voltage sweeping procedures. Both bipolar resistive switching curves are very similarly before and after unipolar resistive switching with 5 mA current compliance. The LRS at 0.1 V is very high around 10 kΩ, whereas the HRS shows a small difference for switching cycles before and after unipolar resistive switching with a resistance at 0.1 V of around 136 kΩ for the former case and 388 kΩ for the latter case. They are comparable with the values of HRS with unipolar resistive switching shown in Figure 5.3 (b). The R_{OFF}/R_{ON} rations in bipolar resistive switching before and after unipolar switching are around 14 and 38.8, respectively, which are much lower than the ratio for unipolar switching.

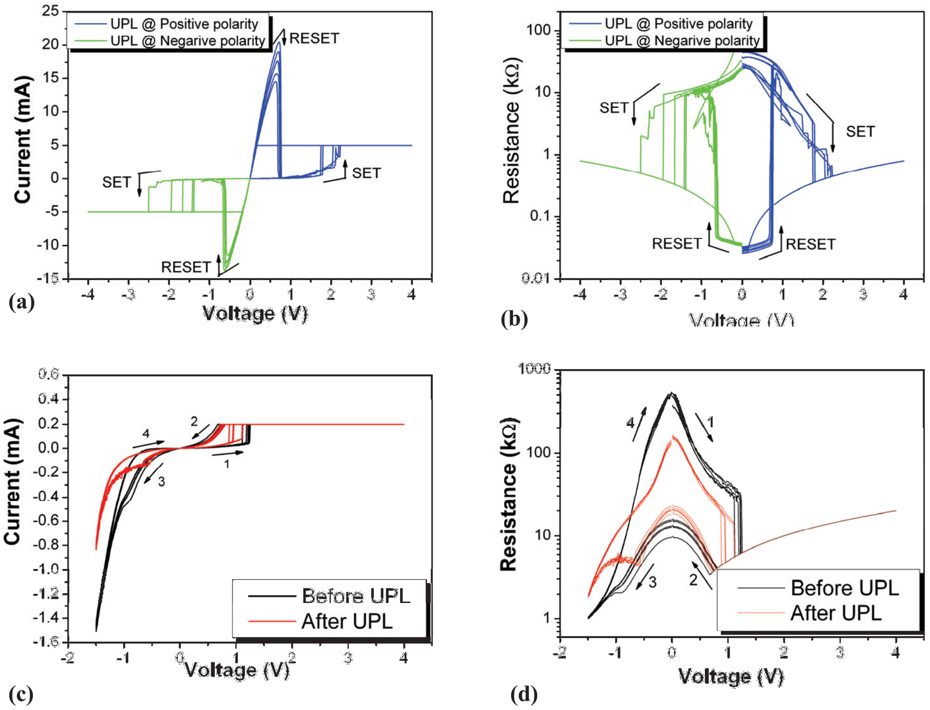

Figure 5.4: Five continuous unipolar resistive switching cycles of both polarities: (a) *I*(*V*) and (b) *R*(*V*) curves. Bipolar before and after unipolar resistive switching: (c) *I*(*V*) and (d) *R*(*V*) hysteretic curves.

Multi-level bipolar resistive switching can also be observed by setting the correct current compliance, as illustrated in Figure 5.5 (a), where 5 continuous switching cycles with a current compliance of 800 µA (blue), 2 mA (red) and 5 mA (black) are plotted. It could be different from pad to pad. Therefore bipolar resistive switching can be still observed using 5 mA compliance current. The great influence of current compliance on the LRS can be clearly seen in Figure 5.5 (b), which depicts the resistance at 0.1 V of both HRS and LRS “read” from the curves in Figure 5.5 (a). The LRS decreases with increasing compliance current from 800 Ω to 100 Ω. However the HRS remains almost unchanged above 10 kΩ.

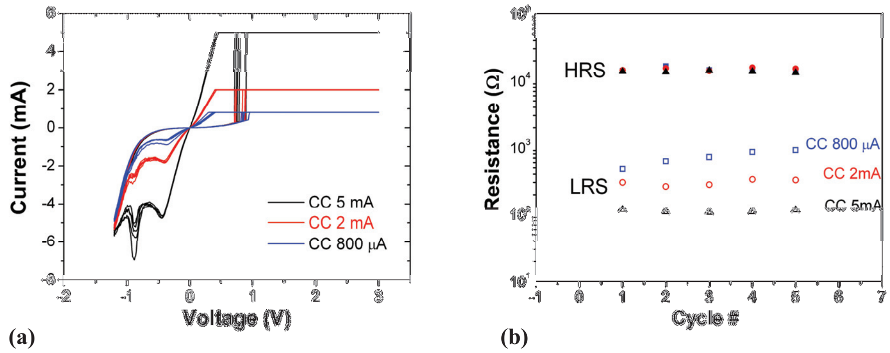

Figure 5.5: Multi-level bipolar resistive switching: (a) *I*(*V*) curves with different compliance current; (b) HRS and LRS at 0.1 V.

5.2.2 Structural change

Bubbles often appear in the Pt/TiO_2/Pt stack structures during electro-forming or resistive switching with a higher current compliance in the mA range. In Figure 5.6 (a)–(c), bubbles that appear on the cell have been captured on an optical microscope after some switching cycles. They are distributed over the whole cell with different sizes which grow from cycle to cycle. A similar phenomenon is found under other pads of in the Pt/TiO_2/Pt configuration but with different numbers and distributions. Under certain pads, only two larger bubbles were observed, whereas under other pads, more bubbles appear. The growth of such bubbles is polarity dependent in that the bubbles only appear and grow during positive voltage sweeps no matter whether they are SET or RESET procedures, but they are seen more frequently after a SET step as shown in Figures 5.6 (e) (f) (g).

It should be mentioned that bubbles grow either in the procedure of the bipolar resistive switching shown in Figure 5.6 (e) or unipolar resistive switching as shown in Figure 5.6 (f) and (g). They appear only under the positively charges sweeping procedures.

This phenomenon may result from an electrochemical redox reaction in TiO_2, during which TiO_2 near the cathode is reduced locally to a non-stoichiometric TiO_x ($x<2$) by attracting O^x ions out of the film. This process can be described by the Krönig-Vink equation as follows:

$$O_O^x \rightarrow V_O^{\cdot\cdot} + 2e^- + 1/2O_2 \qquad 3.2$$

$$Ti^{4+} + ne^- \rightarrow Ti^{(4-n)+} \qquad 3.3$$

The growth of such bubbles was observed with a positive bias applied to the top Pt electrode, which would suggest a local increase in the releasing of O^x ions from the TiO_2 film. This could then end up damaging the cell permanently if these switching operations were repeated during many cycles under very high current compliance in the mA range. This could also be the reason why unipolar resistive switching operations at higher current (mA) have worse endurance characteristics.

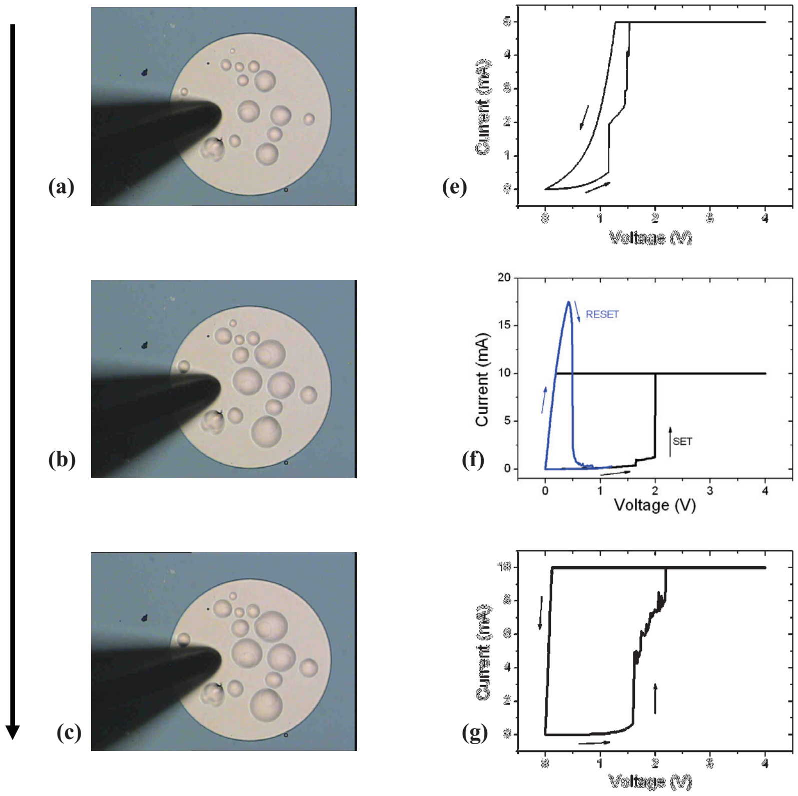

Figure 5.6: Bubble growth during switching procedures. (a) (b) and (c) are pictures taken with a camera after sweeping $I(V)$ on the probe station. (e) (f) and (g) present a switching curve during bubble growth.

This redox process is illustrated in Figures 5.7 (a) and (b). As already mentioned in the discussion about the forming process, local channels composed of defective TiO_x were created after forming, which provides for better mobility of the O^x ions in the film than that in the initial TiO_2. The O vacancies could be filled or left free, with migration of the O^x ions under the applied voltage. This model is mostly used to explain the SET and RESET procedures of bipolar resistive switching as well as bubble growth on the basis of intrinsic ion migration through filaments. Until now, unipolar resistive switching was believed to be a fusing-antifusing process of the filament, with thermal effects leading to breaking of the filament (RESET) when high currents flowed through it. For the SET procedure in unipolar switching, an ion migration model can be applied to understand the reactivation of the filament. However still more investigations are needed to understand bubble growth as well as switching behaviours in such cells. The following study with CAFM could be helpful in giving more insight into this question.

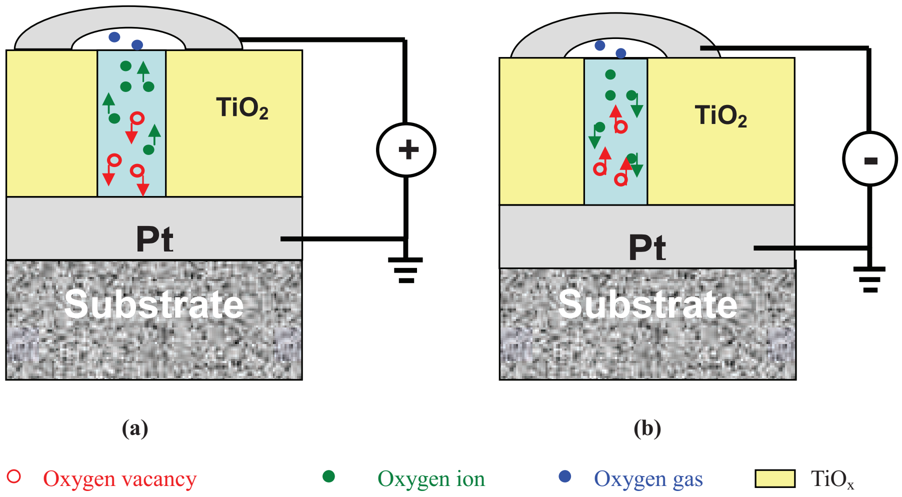

(a) (b)

Figure 5.7: Sketch of bubble growth in a Pt/TiO_2/Pt stack structure under (a) positive and (b) negative bias on the top electrode.

In these MIM cells based on the Pt/TiO_2/Pt configuration, the bubbles are formed only with a positive bias on the top electrode. The structure is apparently symmetric with Pt electrodes on either side of the structure. But there are still many reasons to result in asymmetric situations in the both interfaces. For example, the different behaviours could be cased by the different properties of the electrode-to-oxide interfaces between the top electrode (formed by a metallic deposition process) and the bottom electrode (formed when the oxide is sputtered onto the substrate). It could also be caused by differences in the surface conditions of the interfaces - for example, the top layer of oxide may be contaminated with impurities depending on whether the sample was exposed to anything between the sputter deposition process and the top platinizing process. It should also be noted that the bottom electrode in the sample is a continues Pt thin film which covers the whole 1 inch SiO_2/Si substrate, on which 5 nm thick TiOx is deposited as an adhesion layer. Because the top Pt electrode is much smaller with a diameter of 150 μm, a much higher charge density can form on the top electrode with the same current flowing through the cell. The charge density ratio is around 3.8×10^4, assuming the interfaces under the electrodes are homogeneous and same. Therefore, more oxygen ions can accumulate with a higher density under the much smaller top electrode and form gas bubbles easier than near the much larger bottom electrode

A similar phenomenon is also found in the CAFM measurement on the TiO_2/Pt sample with a mobile Pt coated tip discussed in the next section.

5.3 CAFM study on Pt/TiO_2

The mechanisms responsible for the resistive switching phenomenon observed in sandwiched TiO_2 thin films between two inert metal electrodes have been studied intensively. Most of the published papers propose that the formation and rupture of conductive filaments are responsible for the resistance changing between the HRS and LRS states. The filaments are proposed to be TiO_x sub-oxides after the forming procedure. But until now, there is still very limited evidence to give detailed insight into the nature of the filaments. Most of the analysis methods such as XPS, RBS, XRD, Tof-SIMS, etc., do not have enough lateral resolution to explore the chemical composition or chemical binding energy of the locally distributed conductive paths. High resolution TEM can provide information on the atomic scale. But the preparation methods could either introduce new defects or change the chemical or physical states of the filaments in the film. It is especially difficult to study resistive switching in polycrystalline thin films, which already have defects in the region of grain boundaries. However, CAFM is a direct way for investigating the local conductivity of thin films by scanning the surface with a biased Pt-coated tip, where the Pt tip works as a mobile electrode and measures the I(V) characteristics as well as the surface topography of the film. Choi and co-authors have reported multi filaments observed with CAFM in a vacuum. [60] They put Ru/TiO_2/Al stacked cells into HRS and LRS respectively. Then, the Al top electrodes were removed with nitric acid solution. CAFM revealed that there were more conductive spots distributed in the measured area (500 nm x 500 nm) in LRS than in HRS. According to the much larger cell diameter (300 µm) set to LRS and HRS compared to the much smaller measured regions by CAFM, the filament model is supported but the measured maximum current in both LRS and HRS is very low (< 1.7 nA) and the filaments are distributed randomly. Thus it cannot be excluded that other stronger filaments or a higher filament density could exist outside the areas measured by CAFM. In this work, resistive switching is investigated on a Pt/TiO_2 sample with a mobile Pt tip serving as the top electrode. Therefore, it is advantageous that no etching process is needed to remove the top Pt electrode in order to study directly the filaments on a nanometer scale.

Two models of the CAFM measurements are shown schematically in Figure 5.8. The resistance state can be either formed, SET or RESET with appropriate voltage scanning over the area (red square in Figure 5.8 (a)) or the tip can be kept in one position (red point in Figure 5.8 (b)) and the applied voltage sweeps. Afterwards, the change of topography or current conduction in the area or position can be read out in a scan performed at a much lower voltage in the same area or a larger area. Repeated cycles such as read-out procedures carried out after SET and RESET operations will reveal changes in the local conductivity.

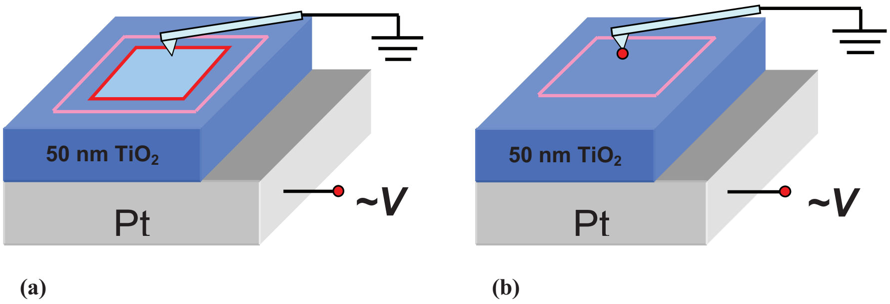

Figure 5.8: Schematic CAFM measurement set-up: (a) write ON or OFF in area in red and read out in pink square. (b) Local conductivity measured at the red point and read out in pink square.

5.3.1 Forming procedure studied with CAFM

For the CAFM measurements, only the voltage-controlled process is used. First, a voltage of -10 V is applied to the bottom Pt electrode, which corresponds to applying a positive +10 V on the Pt tip scanning the surface area (500 nm x 500 nm) indicated by the red dashed line in Figure 5.9(a). Next, a read scan was carried out over a larger area (1000 nm x 1000 nm) by applying +5 V to the tip, with the formed area included in the scan. Figure 5.9 (a) shows the topography of the read out scan and the right pictures (b) are the corresponding current images. Clearly, the topography of the pre-formed region (red dashed line) has changed dramatically compared with the un-formed area surrounding it and has become a rounded bump with maximum height of 27 nm. The local conductivity is not homogeneously distributed with a maximum magnitude of 1 μA, which is the current compliance of the CAFM equipment. Figure 5.9 (a) and (b) show that there is no direct relationship between topography and local conductivity within the formed area. The blue line indicates zoom into the region containing one corner of the formed area and the un-formed area surrounding it. The corresponding topography and current image are illustrated in Figures 5.9 (c) and (d), respectively. In contrast to the virgin topography (Figure 5.9 (e)) and its current image (Figure 5.9 (f)) scanned with the same voltage +5 V on the tip, the area surrounding the formed region shows more locations with much higher conductivity equivalent to more than 1 μA of measurement limitation. The growth of the bump within the formed area could be the result of O^x ion migrations towards the film surface during the forming procedure under the +10 V applied to the Pt tip. Jeong has observed the porous cross-section of a switched Pt/TiO$_2$/Pt structure by TEM. Therefore, the bubbles in Figure 5.6 formed during switching operations with a positive bias may accompany the morphological changes like the bump observed by CAFM in Figures 5.9 (a) and (c), which exhibit a higher locally conductivity than the original states.

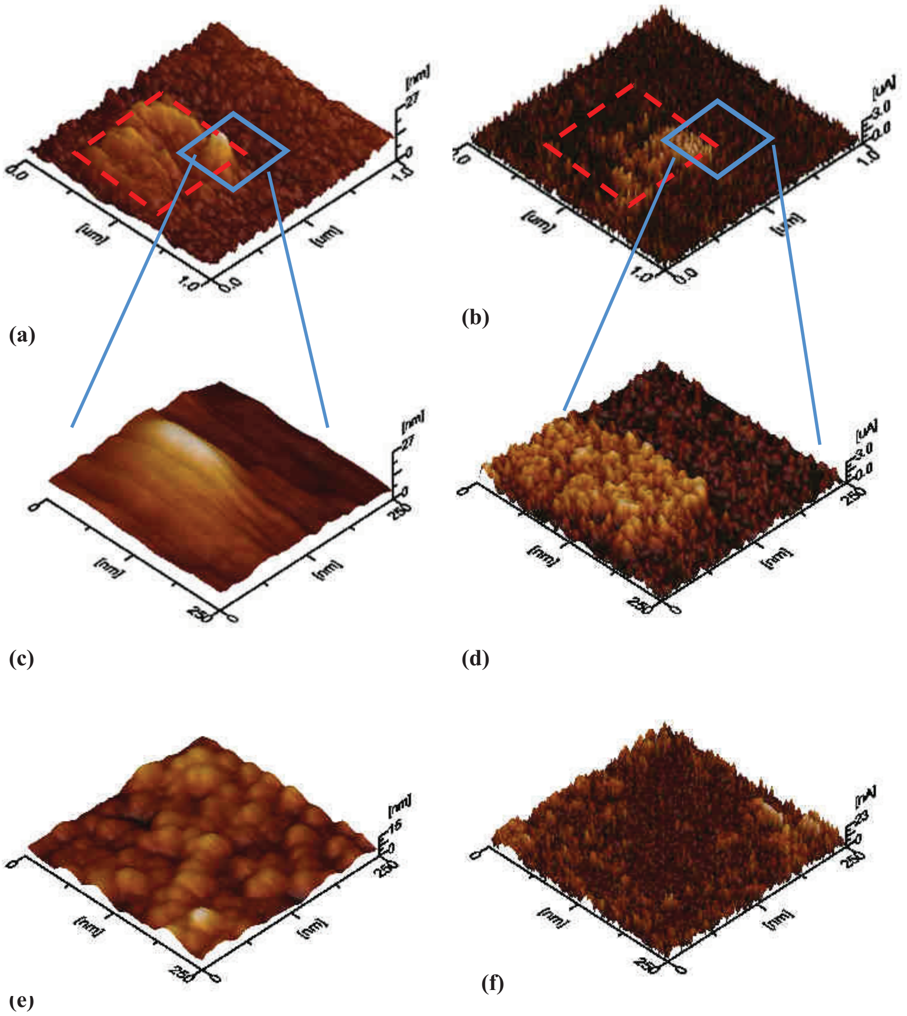

(a)

(b)

(c)

(d)

(e)

(f)

Figure 5.9: (a) Read-out topography (1000nm x 1000 nm) after forming in area (dashed red square); (b) Read out e current image; Amplified (c) topography and (d) current image of the area indicated in blue square. (e) Virgin topography and (f) its current image. All scanned with +5 V.

5.3.2 Resistive switching with CAFM

Both bipolar and unipolar resistive switching in Pt/TiO_2/Pt stack cells have been introduced in section 5.2. CAFM measurements with a Pt-coated tip can be used to study local switching behaviour on a Pt/TiO_2 sample directly without any process being necessary to remove the top Pt electrodes, neither chemically nor physically. In a macro MIM cell, an electro-forming procedure is needed to initiate bipolar or unipolar resistive switching. However, with a biased Pt-tip, resistive switching can be observed without any special forming process. A possible reason for such a difference could be the much higher focused electric field on the very sharp Pt tip over which the voltage can be swept compared to macro electrodes. The four current images in Figure 5.10 display repeatable resistive switching over the whole area indicated with the red square, which can be set to either the HRS or LRS by scanning the area with the correct SET or RESET voltage. Figures 5.10 (a)–(d) show the current image scanned with 1 V over an area of the same size (500 nm x 500 nm). Figure 5.10 (a) shows the local current magnitude in column form distributed over the read-out area. Scanning the area in the red square (250 nm x 250 nm) with 4 V on the bottom electrode eliminates the higher local conductivity areas (LRS to HRS). The effect of RESET scanning can be clearly identified after a sequential read-out scan, as shown in Figure 5.10 (b). The area surrounding the RESET area remains almost unchanged and is much more conductive than the area in the red square, which is in a very poorly conducting state (HRS) with a the magnitude of the current lower than 1 nA under 1 V, which corresponds to the characteristics of a very good insulator. A subsequent SET scanning in the same area (red square) can reverse the resistance state into LRS again. As a result, these columns with higher conductivity tend to “grow” in the same positions with similar magnitude as those shown in Figure 5.10 (a). Similarly, a second RESET procedure carried out in the same area (red square) causes the conductive columns to disappear again, as shown in picture (c). Furthermore, the SET and RESET processes are polarity-dependent: SET HRS-to-LRS with -4 V (+4 V at the tip) and RESET LRS-to-HRS with +4 V (-4 V at the tip). During such reversible growth and elimination of conductive characteristics, the topography remains always the same.

Keeping the Pt-tip in contact with the surface and sweeping the bias between the tip and bottom electrode can characterize the local current-voltage behaviour. Figure 5.11 (a) sketches the measurement set-up. The surface topography is formed roughly by bumps with a maximum height of 12.7 nm. Referring to the description about the sputtered TiO_2 with CAFM provided in chapter 2, the boundaries between two neighbouring bumps are normally the grain boundary. Typical local resistive switching behaviour is shown in Figure 5.11 (b), where in the SET step the voltage is swept from -6 V to +6 V (red), switching the resistance to LRS, and the RESET step involves sweeping the voltage from +6 V to -6 V (green) to revert the resistance to the HRS state. For both the SET and RESET sweeps, a current compliance 10 nA was set.

But a shift of the compliance current from one sweep to another is caused by the offset current regulated by the equipment, which does not play any role in the present discussion. Such switching cycles are repeatable over many cycles.

The surface topography can be changed during scanning with a very high voltage as discussed before in connection with Figures 5.9 (a) and (c), where the whole scanned area grew by up to 27 nm with 10 V applied to the tip. A change in structure on the surface can also be observed by repetitive voltage sweeping at a single location. The measurement configuration is illustrated in Figure 5.11 (a). The wave-like topography was measured by CAFM. The schematic tip in yellow contacted the surface without moving and the voltage was swept. Here, the tip worked as a Pt top electrode with ~10 nm diameter. On a nanometer scale Pt/TiO_2/Pt MIM structure, resistive switching can be observed as shown in Figure 5.11 (b).

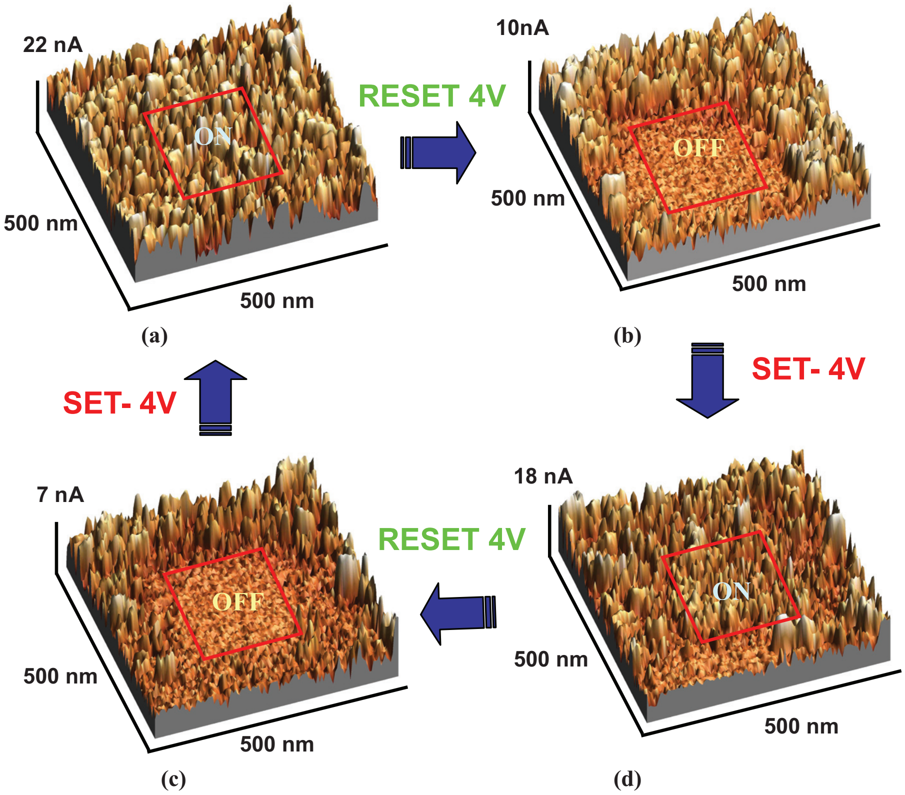

Figure 5.10: Sequential switching states (a) ON to (b) OFF to (c) ON to (d) OFF as a result of read scans with 1 V in areas of 500 nm x 500 nm on the tip after SET and RESET scanning in areas of 500 nm x 500 nm.

After similar repetitive switching cycles at a single position on the surface, a bump-like structure can be observed when an area 250 nm x 250 nm is scanned with less than 0.5 V applied. The bump structure formed around the tip position with a diameter ~ 200 nm is shown in Figure 5.12 (a). Some locations in the ~20 nm diameter area shown in Figure 5.12 (b) had much better conductivity than other areas including the original state. Four very good conductive filaments (> 800 nA) on the hillock were indicated, whereas the other areas still had very low conductivity equivalent to a good insulator. A similar change in morphology is not observed with a negative bias on the tip, which destroys the measurement location directly resulting in a deep hole. An explanation can be advanced similar to the reason given above for the formation of bubbles with a positive bias applied to the top electrode, which is discussed above in section 5.2.2. The radius of the tip (~10 nm) is much smaller than the top Pt electrode shown in Figure 5.6, therefore the formed oxygen gas escapes into the vacuum without accumulating as do those formed under the micro Pt electrodes.

As the sample is exposed to air under normal conditions, the conductivity of such filaments is reduced dramatically, as shown in Figure 5.12 (d). Its topography also changes to some extent, but the same bumpy structure is still identified in Figure 5.12 (c). Although the corresponding filament positions and dimensions remain unchanged, the current with 0.5 V applied decreases by more than 90 % with a maximum magnitude of 83 nA (Figure 5.12 (d)) compared to the individual filaments measured in a vacuum of 10^{-5} mbar (Figure 5.12 (b)). Moreover the positions with higher conductivity cannot be detected again after the first scan in air even with higher scanning voltages of -1 V, -2 V and -3 V. Meanwhile the surface topography becomes so ill-defined that no structure can be identified.

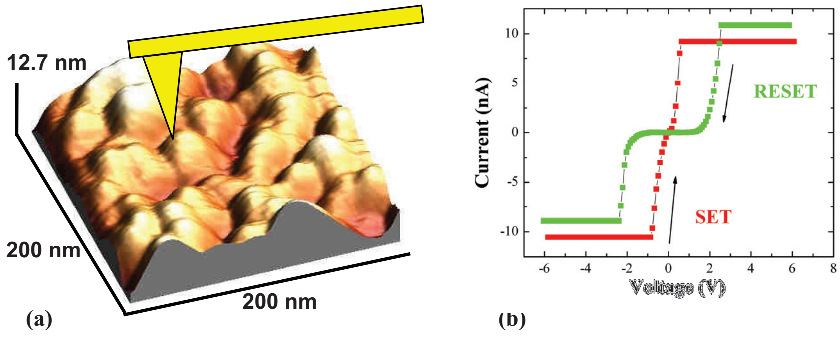

Figure 5.11: (a) Schematic set-up for measuring I(V) characteristics at a particular location; (b) typical resistive switching I(V) hysterics with CAFM.

There could be two reasons responsible for the reduction and disappearance of filaments after exposure of the sample to air:

Firstly, an adsorbed layer may form under ambient conditions between the tip and the actual TiO_2 thin film layer. Peter el al. have investigated the effect of adsorbates on measurements of surface topography and on the corresponding piezoelectric response of the single-crystal $BaTiO_3$ using piezo-response force microscopy (PFM).[76,77] They compared the results on the same area under ambient conditions and in vacuum after heating to 350 ^{o}C, after which the surface can be considered to be adsorbate free. Their results show that the surface topography image measured under ambient conditions is vague but still comparable with that measured under adsorbate-free conditions. The effective amplitude of the piezoelectric response on the adsorbate-free surface can be drastically enhanced by 250 %. Their simulation gives more insights and reveals that adsorbates result in an additional potential drop between tip and actual layer and therefore reduces the piezoelectric response. Similarly the conductivity is reduced dramatically when the measurements are done under ambient conditions. Both surface topographies measured under the two conditions are comparable, but the difference is also obvious. The adsorbate becomes a series resistance between the tip and the actual layer and results in a dramatic reduction of the current there.

Secondly, the re-oxidation of filaments composed of non-stoichiometric TiO_x could be another reason for the reduction of the current passing through them. As introduced in chapter 2 in connection with the resistive switching mechanisms in transition metal oxide materials, the filaments could form regions which are locally deficient in oxygen owing to oxygen migration under the action of the electrical voltage. This process is also classified as an electrochemical reaction in transition metal oxides. These locations become better conductors. Therefore, if the composition of these locations is oxidized by the diffusion of the oxygen from outside, a higher resistance can result.

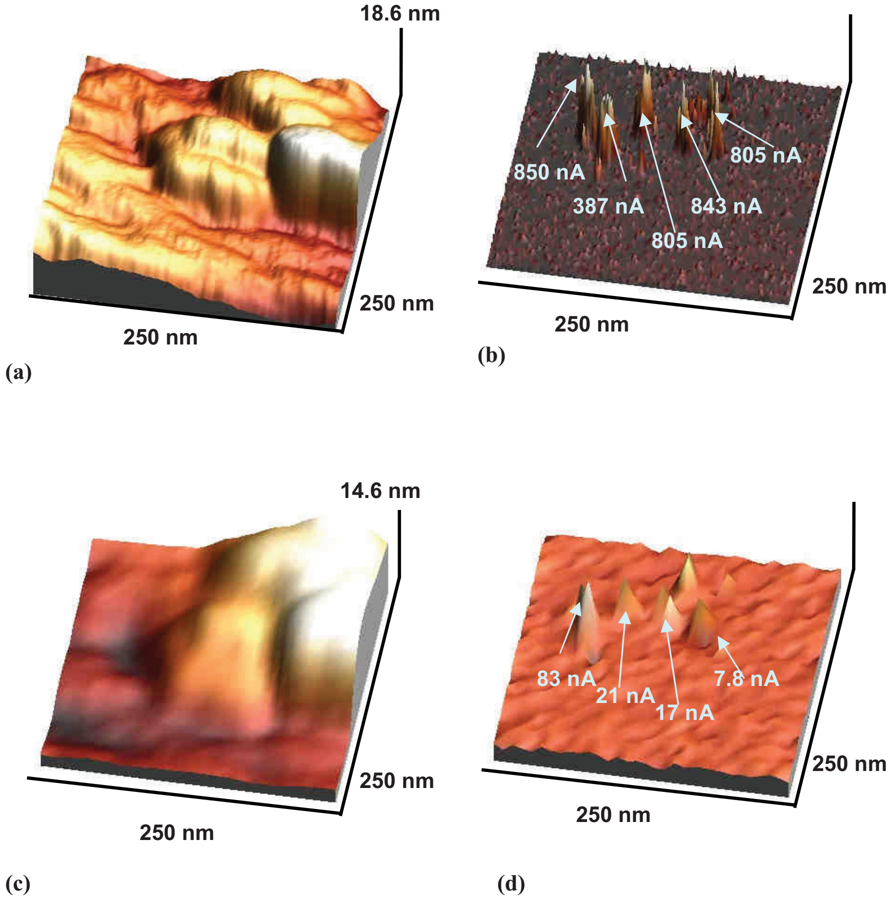

Figure 5.12: (a) Topography and (b) Current image of CAFM in vacuum (10^{-3} mbar); (c) Topography and (d) Current image in air.

Chapter 6 Resistive switching in TiO_2 with Cu or Ag electrodes

In this chapter the electro-forming process and resistive switching in TiO_2 with electrochemically active electrodes of Cu and Ag are discussed. Five resistance states are identified: initial, OFF and 3 different ON states exhibiting reduced activation energies depending on their resistances. The possible current conduction mechanisms are discussed. CAFM helps to confirm the role of filament conduction inside the formed Cu/TiO_2/Pt MIM cells.

6.1 Electro-forming

In the initial starting state, the Cu/TiO_2/Pt metal-insulator-metal (MIM) cell doesn't show any resistive switching behaviour without a forming procedure. The input current controlled by an Agilent B1500 semiconductor analyzer is sketched in Figure 6.1 (a), where the current increases in 10 µA steps with a delay of 500 ms without voltage limitation. A typical current-controlled forming process takes place at a cross point of size 10 µm x 10 µm as shown in Figure 6.1 (b), during which the voltage on the cell increases with current as indicated by arrow 1. The electro-forming is complete when the voltage drops abruptly from ~ 2.9 V to 0.6 V at ~ 600 µA (arrow 2). The forming voltage (V_{form}) and forming current (I_{form}), with which forming ocuurs, are important parameters related to cell size and thickness of the sandwiched TiO_2 layer. The electrical field for forming E_{form} can be calculated with the equation in the inset of Figure 6.1 (b). The resistance (R_{form}) of the example cell directly after forming is around 800 Ω as calculated from the linear $V(I)$ characteristic (arrow 3). This low resistance can be reversed to a HRS by a voltage-controlled process as shown in Figure 6.1 (c) with the arrows and numbers indicating the sweep procedure: Voltage swept forwards from 0 V to -3 V and backwards again to 0 V. Between 0 V and -2.8 V, the resistance remains constant at 800 Ω exhibiting ohmic conduction. At -2.8 V, the current drops abruptly with any increase in voltage magnitude. The cell is then switched OFF (LRS to HRS). Current conduction in the HRS state is non-ohmic in that the device exhibits a non-linear current-voltage characteristic. The resistance of the HRS at 0.1 V is 2.3 MΩ, which is 5 orders of magnitude larger than that at LRS after forming. Therefore the MIM cell is activated and becomes switchable.

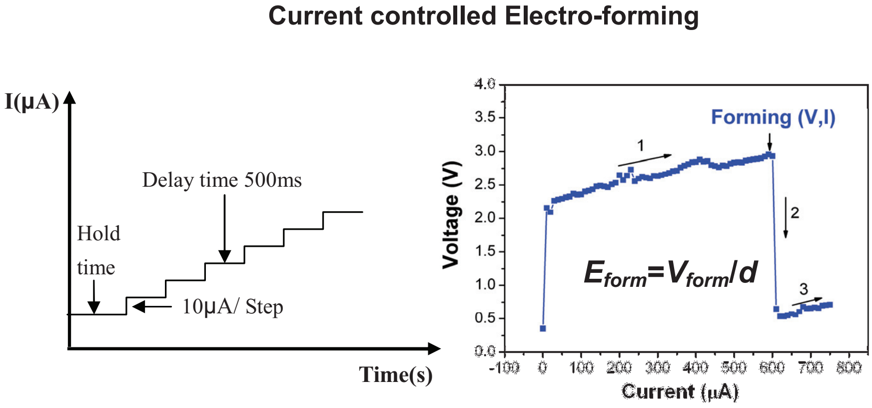

(a) (b)

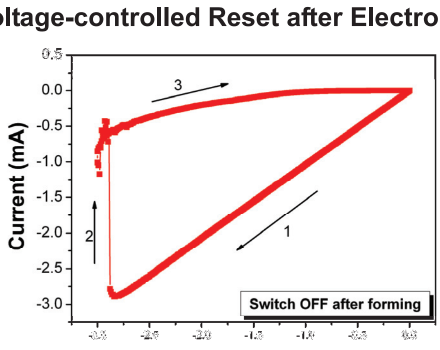

(c)

Figure 6.1: (a) Important parameters set for current-induced forming procedure (b) Current-induced forming (initial state-to-LRS); (c) Voltage-controlled RESET (LRS-to-HRS).

The dependence of the forming process on oxide thickness and pad size were investigated as follows. Cells with two different TiO_2 layer thicknesses (27 nm and 60 nm) and three different pad sizes: 2 x 2 μm^2, 5 x 5 μm^2, 10 x 10 μm^2, were prepared. They were all electroformed with current-controlled processes at the same step rate (10 μA/step) and delay (500 ms) as described in Figure 6.1(a). Mean values and standard deviations of the forming electrical field, E_{form}, the forming current, I_{form}, and the resistance after forming, R_{form}, are plotted as a function of the pad size as shown in Figures 6.2(a), (b), (c), respectively, where black points and bars represent the mean value and standard deviation measured on the cells with 27 nm ALD TiO_2 and the red points and bars are measured from those with 60 nm ALD TiO_2.

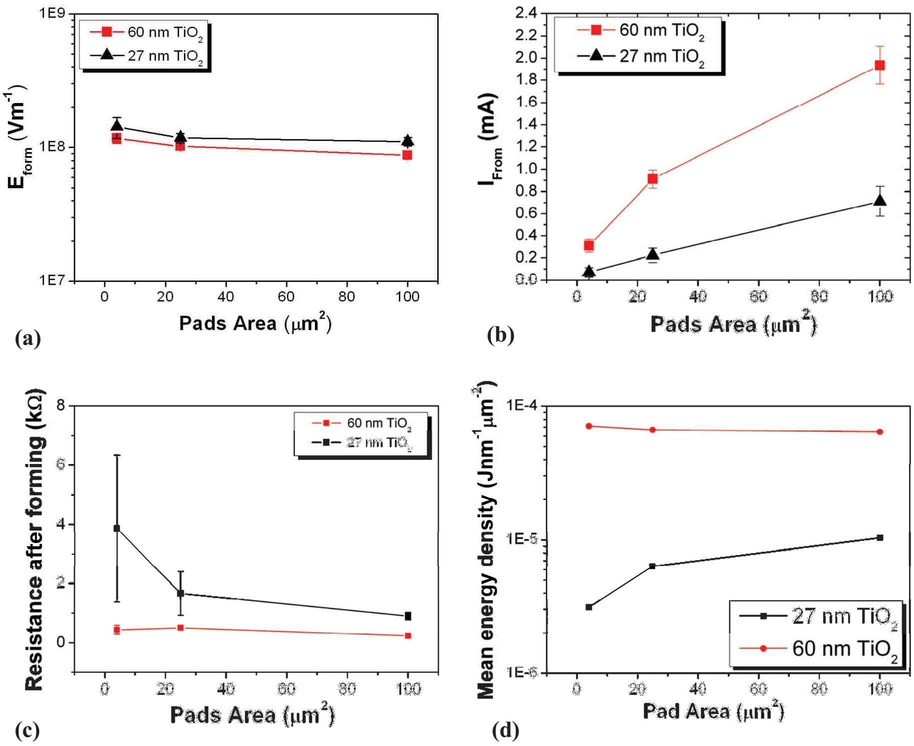

Figure 6.2: Size and thickness dependence of current-induced forming at the Cu/ TiO_2/ Pt MIM cross points. (a) Size and thickness dependence of the forming electrical field E_{form}. (b) Size and thickness dependence of the forming current. (c) Size and thickness dependence of the resistance after forming. (d) Mean electrical energy *V.I.t/volume* (Joule/nm*μm^2) imput until forming finished.

Although the forming electrical field, E_{form},on the pads of the thinner film was larger than that for the thicker film, the values for both thicknesses are still very close to one another other, between 10^8 V/m and 2 x 10^8 V/m as shown in Figure 6.2 (a). Therefore, a strong thickness dependence of the forming voltage V_{form} can be found in this Cu/TiO_2/Pt MIM structure. This is consistent with results obtained on Cu/SiO_2/Pt systems.[78] This weak size dependence suggests that the electro-forming mechanism in this material system should be attributed to the formation of local filament(s) or conductive path(s) bridging the two electrodes. The constant forming electrical field E_{form} implies a migration of ions involved in the process in the Cu/TiO_2/Pt configuration. The ToF-SIMS shows an interdiffusion of Cu atoms into the TiO_2 thin film as indicated in Figure 6.3 (a) on a sample in the ON state. Its top Cu electrode is etched with 0.1 mol/L $FeCl_3$ solution before the SIMS measurement. On the other hand, the forming electrical field E_{form} is nearly constant in spite of the dramatic increase in pad size: 4 μm^2, 25 μm^2, 100 μm^2. The filament model can be applied to explain this observation as follows: Similar to Ag dendrite growth indicated in Figure 2.5, several parallel accumulations of Cu are able to grow from the cathode at the beginning. With a reducing distance between the filaments tip and Cu anode, the electrical field there will be enhanced and will accelerate the growth of the filament from the tip. This process will continue until one of them makes contact with the anode as sketched in Figure 6.3 (b).

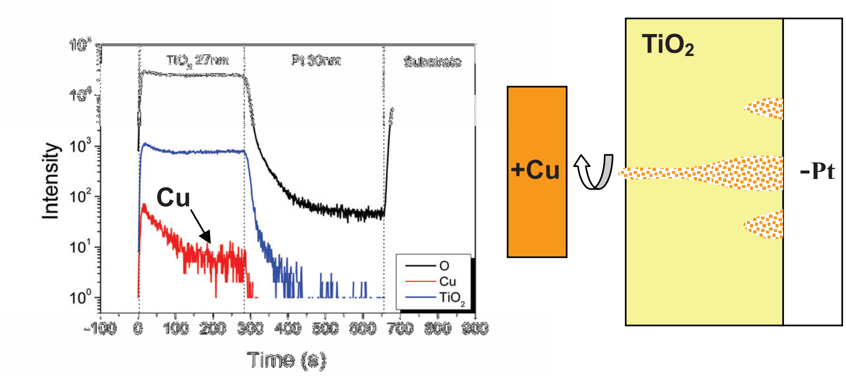

(a) (b)

Figure 6.3: (a) ToF-SIMS of a switched ON cell on a Cu/TiO_2/Pt structure after etching of the Cu top electrode. (b) Sketches of the sample in the ON state for SIMS measurements after removal of Cu top electrode.

Figure 6.2 (b) depicts how the forming current I_{form} depends also on the oxide thickness and pad size. The forming current increases almost linearly with size, possibly implying an interfacial current conduction mechanism before the electro-forming procedure. The values of the forming current I_{form} in the 60 nm thick TiO_2 film are between 3 and 5 times larger than in the 27 nm thick films, i.e. larger than the ratio of thicknesses which is 2.

Figure 6.2 (c) shows the low resistance R_{form} of the formed pads with both oxide thicknesses as a function of pad size. The resistance after electro-forming is in both cases much lower compared with in the resistance in the initial resistance state. Firstly, for cells with 60 nm TiO_2 the value of R_{form} is around 500 Ω, which is obviously lower and with less scatter than the resistance between 1 kΩ and 4 kΩ found in the thinner, 27 nm film. Secondly, the resistance R_{form} in the 27 nm film is more likely to be related to pad size. The mean value of R_{form} and the scatter are reduced with increase in size, while it remain almost constant in the 60 nm thick film. This may suggest that more than one filament could be formed simultaneously in the thinner film. In the thicker film, one filament could reach the counter electrode as a result of the competition between parallel growing filaments. However, this seems to contradict the distinctly lower R_{form} found in the thicker film if only one filament is formed with the same characteristics as in the case of the thinner film. This can be understood with the help of Figure 6.2 (d).

Figure 6.2 (d) depicts the total energy density (in Joule nm^{-1}μm^{-2}) injected into the systems with the two thicknesses as a function of the pad area, until electro-forming. Firstly, the energy is nearly unchanged in the 60 nm TiO_2 (red), equivalent to a more than 10 orders of magnitude higher volume energy density than that needed in cells with a thinner TiO_2 layer (black). However, the energy density in the thinner film is pad size-dependent, increasing from 3 x 10^{-6} J nm^{-1}μm^{-2} to 1 x 10^{-5} J nm^{-1}μm^{-2} with an increasing in pad size from 4 μm^2 to 100 μm^2. An observation of the injected energy density until electro-forming may help to explain the much larger resistance in the thicker film and the clear dependence of the resistance on pad area in the thinner film. On the basis of the literature and the ToF-SIMS measurements of Figure 6.3 (a), Cu ion migration takes place in TiO_2 during forming and resistive switching. In such an electrolytic system, both electron and ion migration make contributions to the measured current I. However it is still difficult to distinguish exactly how much contribution is made by ion migration during electro-forming.

The total electrical energy W_{form} transferred per unit volume until the cell is formed can be found by integrating the energy at every current stage as follows:

$$\text{Total injected energy} = W_{form} = W_e + W_i = \sum_{0}^{I_{form}} V_i * I_i * t \qquad 6.1$$

$$\text{Total injected energy density} = \frac{W_{form}}{thickness(nm) * Padsarea(\mu m^2)} \qquad 6.2$$

where V_i is the voltage on the cell at current I_i until forming is complete, t is the 500 ms time period for every current stage I_i. W_e and W_i are the contributions of energy from the electron and ion transportation through the structure, respectively. Although no exact information exists on the proportion of ion migration involved in the total energy density before forming is complete, the much higher total injected energy density in the 60 nm thick TiO_2 layer than in the thinner 27 nm TiO_2 layer may imply that more ion migration is involved during the forming process, which could give some insight into why lower resistances are found after forming in cells with thicker TiO_2 layers than in cells with thinner film, as shown in Figure 6.2 (c). The similar total input energy density in the thicker 60 nm TiO_2 layer (red symbols in Figure 6.2 (d)) may be responsible for the similar resistance of about 500 Ω after forming, whereas the much lower total injected energy density of the pads in cells with 27 nm thick TiO_2 layers (black symbols in Figure 6.2 (d)) could result in a higher resistance after forming.

On the basis of the electrochemical metallization memory model (ECM) and the above measurements and discussions, the processes involved in electro-forming and I the following RESET procedure in Cu/TiO_2/Pt MIM cells is sketched schematically in Figure 6.4. The forming mechanisms can be described qualitatively as follows: (a) At the start, by applying a positive current or voltage on the Cu electrodes, the Cu atoms in the anode are ionized and start to drift towards the cathode via some easier mobile channels. (b) The positively charged Cu ions from such channels are reduced in the Pt cathode and accumulate there. Therefore, some parallel filaments are formed simultaneously and grow with time until one or several filaments bridge across to the electrode. The distance between the tip of the growing filaments and the cathode reduces with time, which corresponds to a visual cathode moving towards the anode and results in an enhancement of the local electrical field there. As a result, the ion migration in the gap is accelerated as the distance is continuously reduced. The growth of a similar channel has already been introduced in Figure 2.5 (c), where several Ag dendrites are formed from the cathode. In this way, some filaments grow faster, whereas the growth of other filaments is slowed down. Thus, there is competiton in growth between different filaments during the forming process until one or several filaments reach the cathode first. After this, a filament is formed and causes the low resistance state after electro-forming. (d) A RESET procedure is needed now to set the resistance state back to the high resistance state by dissolving the filament with a negatively swept voltage applied to the Cu electrode. At this point, the cell is ready for repetitive resistive switching.

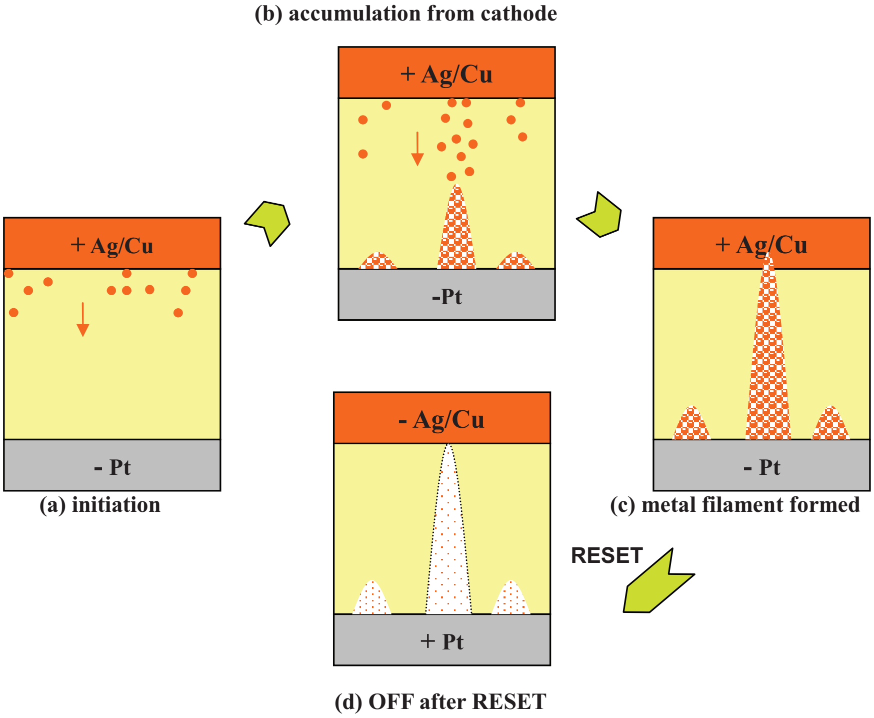

Figure 6.4: Electro-forming and RESET process caused by migration of extrinsic ions from an electrochemically active anode electrode, typically Cu or Ag electrodes.

Based on this model, the effect of the oxide thickness and pad size on the electro-forming process can be explained.

Firstly, enough energy is needed for the migration of ions through a solid electrolyte layer. According to the result of Figure 6.2 (a), the forming electrical field E_{form} is independent of film thickness and pad size.

Secondly, before electro-forming, the leakage current through the cell is area-dependent, which means that a homogeneous conduction mechanism over the whole device area is responsible for charge transport.

Thirdly, if the film is very thin, it is very possible that more than one filament will be formed during forming. As a result, the final low resistance of the MIM structures with thinner TiO_2 layer (27 nm) after electro-forming depends on electrode size. However, if the sandwiched TiO_2 layer is thick enough, competition of filaments during growth usually leaves a single filament standing, or possibly a small number of filaments. This could be the reason for the observation that the low resistance after electro-forming in MIM structures with thicker TiO_2 layers (60 nm) is independent of pad size as shown in Figure 6.2 (c).

Fourthly, the much higher injected energy density before electro-forming in thicker films may imply that much more ion migration is involved, which results in a lower resistance after forming in the device with a 60 nm thick TiO_2 than in the cell with a 27 nm thick TiO_2 layer.

The filaments retraced after the electro-forming procedure initiates the MIM cell for resistive switching. Different low resistance states can be reached by programming the appropriate currents (compliance currents). More detail about resistive switching in Cu/TiO_2/Pt structures will be provided in the following sections.

6.2 Resistive switching of Cu/TiO_2/Pt structures

6.2.1 Typical bipolar resistive switching

Typical voltage-controlled bipolar resistive switching behaviour: the current-voltage and resistance-voltage characteristics of a Cu/TiO_2/Pt cross point cell are shown in Figures 6.5 (a) and (b), respectively. The active size responsible for resistive switching is regarded as the crossed area of the bottom Pt electrode and top Cu electrode. Thus the active switching structure can be sketched in a simplified form as in the inset of Figure 6.5 (a) by replacing the continuous TiO_2 layer with a single column sandwiched between two electrodes. The voltage sweeping procedure is depicted by the arrows and numbers in both pictures. The voltage starts forwards from

0 to a maximum of 3 V. At ~1 V the current increases abruptly from HRS (OFF) to LRS (ON). This voltage is defined as the threshold voltage (V_{ON}) for switching ON. To avoid breakdown, the allowed current during switching was limited through the current compliance (here 200 µA) or writing current. This value has a great influence on the resistance in the LRS and can result in multi-bit storage characteristics for the cell, as will be shown later. Next, the LRS can be set back or reversed to the HRS with a negative voltage sweep. As shown in Figure 6.5 (a) by arrow 3, the cell starts to return to the HRS (OFF) from the LRS (ON) gradually from -0.8 V (V_{OFF}) when the voltage is swept backwards from +3 V to -2 V. The corresponding current at the voltage V_{OFF} is regarded here as the erase current (I_{Erase}). The ratio of the resistances in HRS to LRS states at 0.1 V is ~ 40. In this case, the switch OFF is a slow process compared to the abrupt switch ON at V_{ON}. The transition of the resistance state starting at -0.8 V indicated by arrow 3 is also classified as negative resistance behaviour, which could be attributed to dissolution of the filament under negative voltage. Several parameters in the measurements set-up such as compliance current, delay time and negative voltage range exert a great influence on the resistance state of the cell and will be discussed in the next sections.

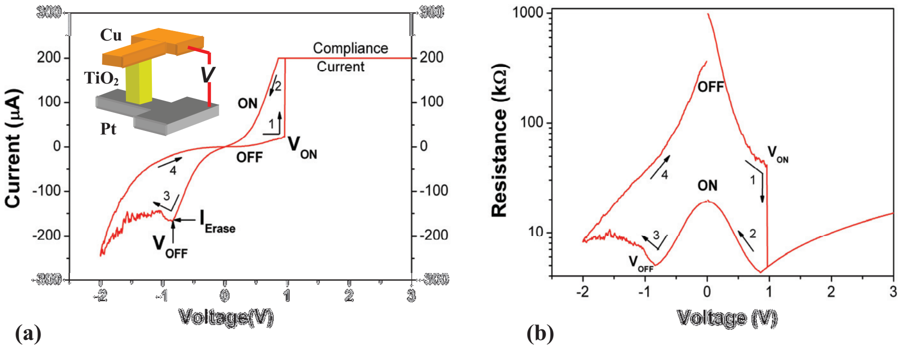

(a) (b)

Figure 6.5: Typical (a) current-voltage and (b) resistance-voltage characteristics of a Cu/ TiO_2/ Pt MIM cross points with 27 nm thick ALD TiO_2 and a pad area of 4 μm^2

6.2.2 Compliance current-dependent resistive switching

The compliance current is set to protect the cells from excessive currents flowing through the cell as the resistance state changes abruptly from HRS to LRS abruptly. As the voltage increases above the switch ON voltage V_{ON}, the bias applied to the cell starts to be controlled by the current via the resistance after switch ON at V_{ON}. By setting the correct current compliance, multi-level resistive switching can be observed, as shown in Figure 6.6 and measured on a Cu/60nm TiO_2/Pt crossbar cell with a lateral size of 15 x 7.5 μm^2. Figure 6.6 (a) depicts the current-voltage characteristics obtained with different current compliance settings. The changes in the two resistance states as a function of the current compliance are shown in Figure 6.6 (b) where the currents at a voltage of 0.1 V in the LRS (red) and HRS (black) states are plotted. It can be seen that the LRS current increases by more than 12 times as the compliance current is increased, but the HRS current reduces just slightly from 0.1 µA to 2 µA.

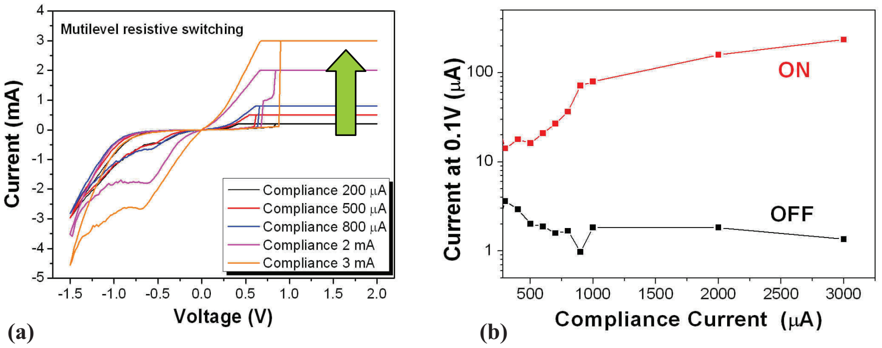

Figure 6.6: Typical current compliance-controlled multi-level resistive switching in a Cu/ TiO_2/ Pt MIM cross cell with a 60 nm thick ALD TiO_2 and a pad area of 15 x 7.5 μm^2. (a) $I(V)$ characteristics and (b) Current in LRS and HRS states at 0.1 V as a function of current compliance.

The resistance (R_{ON}) of the ON state at 0.1 V is plotted as a function of compliance current in Figure 6.7 (a). Every red point here is the mean value of resistance measured at 0.1 V in 5 continuous swept cycles at the same compliance current and in the same crossed cell. The resistance reduces from 8 kΩ to only 100 Ω as the compliance current is increased from 300 µA to 3 mA. Meanwhile the resistance in the HRS did not change much compared with LRS, with increasing compliance current. Figure 6.7 (b) depicts the ratio of the resistances in the HRS and LRS states at 0.1 V and this is seen to increase with compliance current from a ratio of 4 to 173. This feature can be attributed to the voltage behaviour during switch ON. The current remains at the compliance current so long as the calculated voltage ($V=I_{compliance}*R$) is larger than the swept voltage, which is increased (forward direction) or decreased (reverse direction) at a rate of 10 mV/10 µA. Thus, the actual bias applied to the cell during this stage depends not only on the current compliance but also on the resistance change from the HRS state up until it reaches a stable LRS state. In other words, a higher compliance current value results in a higher actual voltage applied to the cell during the switch ON process. In a solid electrolyte system, the current through the structure includes contributions from both the electron and ionic currents as soon as the filament(s) growth involves ion migration. But it is impossible to extract the value of this current from this measurement. Both the higher current and higher voltage during the switch ON process could imply more ion migration under the effect of the electrical field, which may enlarge the size of the metallic filament(s) or enhance the conductivity by inducing a higher carrier density in the semiconductor filament(s). The way in which different LRS levels can be programmed by setting different compliance currents leads to great advantages in the realization of high memory densities in RRAM chips. This is an alternative way for shrinking the memory cell size but increasing memory capacity by enlarging the number of memory states in each memory cell.

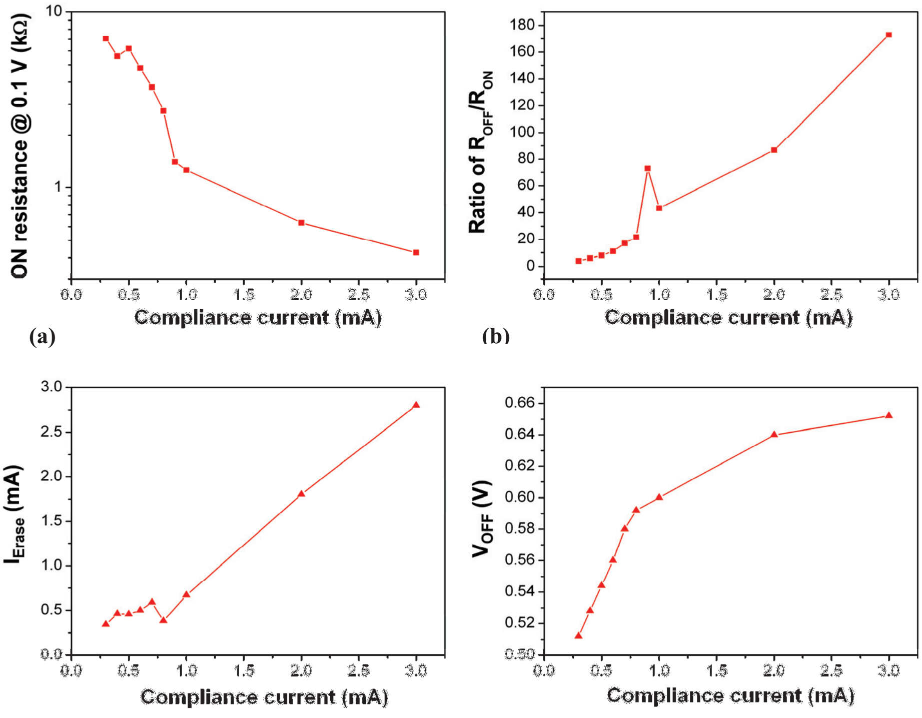

(a) (b)

(c) (d)

Figure 6.7: Influence of compliance current on (a) ON resistance at 0.1 V; (b) Ratio of high resistance to low resistance at 0.1 V; (c) Maximum switch OFF current or Erase current I_{Erase}; and (d) Switch OFF voltage V_{OFF}. The measurements were done on a Cu/TiO_2/Pt MIM crossed cell with a 60 nm thick ALD TiO_2 layer and a pad area of 15 x 7.5 μm^2.

As already mentioned above, I_{Erase} and V_{OFF} are the critical voltage and current at which the LRS begins to return to the HRS, either abruptly or continuously, as the voltage is swept. The magnitudes of I_{Erase} and V_{OFF} are plotted as a function of the compliance current in Figures 6.7 (c) and (d). The erase current I_{Erase} is also the maximum ON current under a negative voltage and depends on the LRS after resistive switching, resulting in an increase in I_{Erase} with programmed current (compliance current) as shown in Figure 6.7 (c). For bipolar resistive switching, the corresponding I_{Erase} should be lower than the programmed current used in the SET procedure.

Meanwhile, the magnitude of the switch OFF voltage V_{OFF} increases by 30 % as the the programmed current is increased, from 0.51 V at 300 μA to 0.65 V at 3 mA, as plotted in Figure 6.7 (d).

According to the filament model based on ion migration, the reason for multi-level resistive switching being controlled by the compliance current can be analyzed qualitatively as follows:

The electrical energy injected into the cell can be controlled by the magnitude of the compliance current. After the similar investigation from Schindler [79]the entire $I(V)$ resistive switching procedure is sketched in Figure 6.8 (a), where switching starts at V_{ON} and turns into a current-controlled process indicated by the thick blue lines. The corresponding actual applied voltage during this current-controlled process is sketched in Figure 6.8 (b), again in thick blue lines. After V_{ON}, the voltage decreases gradually and depends on the real resistance R because the current here remain unchanged at the compliance current I_C until voltage V_S when a stable resistance is achieved. This stage is marked by the red cycle in Figure 6.8 (b), which is responsible for stabilizing the resistance degradation because of the continuously reducing resistance R during this stage. Therefore, the energy needed for this process with the programmed compliance current can be written as:

$$W_{ON} = \sum_{V_{ON}}^{V_S} V_i I_C t = I_C t \sum_{V_{ON}}^{V_S} V_i \tag{6.3}$$

Vi is the real voltage during the switch ON process from V_{ON} to the voltage V_S in the stable state. t is the time delay during sweeping. I_C is the compliance current which is kept unchanged during this stage. The energy W_{ON} contributes to the ion migration needed for the switch ON process.

Waser and coworkers have discussed the ionic current density i generated by an electric field E for a mobile ionic species M^{z+} with charge z. [32] The resulting ionic current i can be described as:

$$i = 2zecav\exp(-\frac{Wa}{kT})\sinh(\frac{azeE}{2kT}) \tag{6.4}$$

where e is the elemental charge, c is the concentration of mobile ions M^{z+}, a is the hopping distance of ions and v is a frequency factor. Wa is the activation energy for ion hopping in the absence of an electrical field.

Assuming the switch ON voltage V_{ON} is similar and independent of switching cycles with different current compliance, and that the delay time remains the same, then increasing compliance current I_C in equation 6.3 provides more energy for the switch ON procedure before a stable resistance R_S is achieved at time t_S. Assuming that the mean energy W_i needed for every ion hopping through a distance a remains stable and constant, then a higher energy caused by a higher compliance current I_C implies more migration of ions (W_{ON}/W_i) and this leads to a degradation in resistance as the voltage goes from V_{ON} to V_S, causing more impurities to be injected into the open channel or filament. Once the density of impurities is high enough for them to be connected, metallic conduction occurs in the channel.

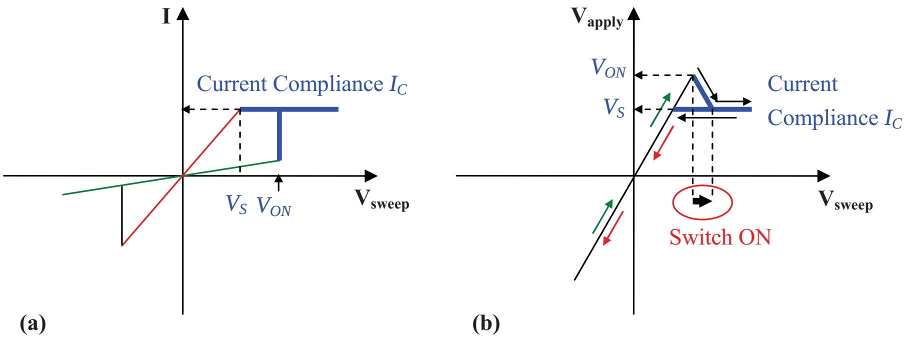

Figure 6.8: (a) Sketch of the $I(V)$ curve for complete resistive switching. (b)The real voltage against current, including the current controlled stage indicated by the thick blue line. The arrows indicate the sweep procedure.

6.2.3 Negative voltage dependence of resistive switching

Instead of an abrupt reduction, a continuous reduction of the switch OFF current after V_{OFF} is normally observed during bipolar resistive switching at lower compliance currents (µA ~ mA), as shown in Figure 6.5 and indicated by arrow 3. It was observed that the range of negative voltage used for switch OFF has a remarkable influence on the RESET as well as the following SET procedure of the memory cell. A cell with a 60 nm thick TiO_2 layer of size 3 x 5 μm^2 was switched for 5 continuous cycles with the compliance current set to 200 µA but with different maximum negative voltages of -1.0 V, -1.2 V and -1.5 V. The delay time was kept constant. Thus, three cycles depending on maximum negative voltages of -1.0 V, -1.2 V and -1.5 V were taken to represent the switching behaviour and are plotted in Figure 6.9 (a) in blue, red and black, respectively. The mean value of the current at 0.1 V for both ON (LRS) and OFF (HRS) states was plotted in Figure 6.9 (b) in red and black squares as a function of the maximum negative voltage. The higher negative voltage resulted in a decrease in the OFF (HRS) current (Figure 6.9 (b), black) which corresponds to a higher HRS resistance. Thus, with a larger negative voltage swept range of -1.5 V, the HRS can be enhanced by about 600 times compared with that with a negative voltage of -1.0 V. However, the LRS current (in red) programmed with the same compliance current of 200 µA reduced only slightly ~ 10 % as the maximum negative voltage was reduced from -1.5 V to -1.0 V. The negative voltage range had less influence on the LRS but a larger influence on the HRS. Therefore, the ratio of resistances in the HRS and LRS states can be controlled by both parameters: the maximum negative voltage and the compliance current and this gives more flexibility in regulating the two resistance states with respect to the design requirements of memory devices. Moreover, higher HRS resistances resulted in an increased switch ON voltage V_{ON} (SET voltage) as plotted in Figure 6.9 (b) (blue stars). This voltage had no obvious impact on the LRS with the same compliance current used in this study.

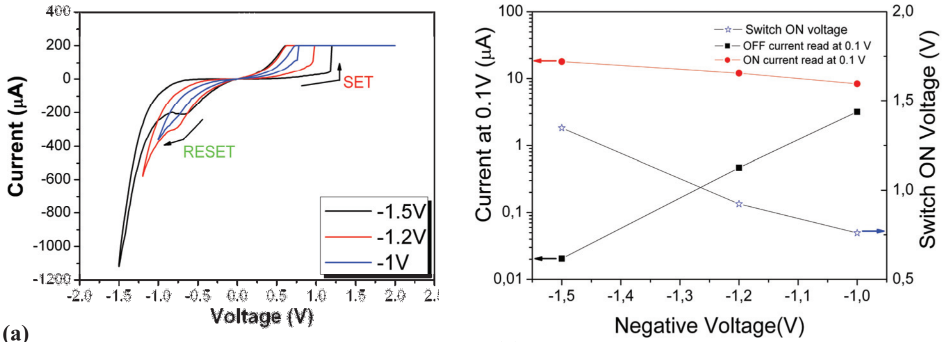

(a)

(b)

Figure 6.9: (a) Current-voltage characteristics of resistive switching cycles obtained by sweeping the negative voltage over different ranges (-1.5 V, -1.2 V and -1.0 V), (b) Mean value of the current at 0.1 V in both ON and OFF states and switch ON voltage. The measurements were done on a Cu/TiO_2/Pt MIM cross cell with a 60 nm thick ALD TiO_2 layer and a pad area of 3 x 5 μm^2.

On the basis of the above observations on the influence of the switch OFF voltage on the bipolar resistive switching behaviour, different OFF resistances (HRS) can be regulated by correctly setting the negative voltage. But an excessive negative voltage could lead to damage to the device by switching ON with a negative polarity. From the viewpoint of the electrochemistry of solids, the applied voltage plays a critical role in controlling ion migration in the material. The higher OFF resistance (HRS) at larger negative voltage (-1.5 V) may be caused by a more complete retracing of the Cu or possibly O ions along the filament than at the smaller negative voltage (-1.0 V). But here, the time effect could also contribute to the form of the final resistance state because the voltage sweep rate remains at 10 mV/10µs. Therefore, a larger negative voltage sweep range causes the cell to remain under electrical bias for a longer time. In the next section, we will discuss the effect of delay time on resistive switching.

As discussed in the last section, the actual voltage during switch ON should also have a critical impact on the final programmed LRS resistance. According to the multi-level characteristics of the LRS controlled by the compliance current, the actual input energy ($W = I_{compliance}^2.R.t$) during the switch ON procedure increases as the compliance current is increased. If ion migration involves the switch ON operation, similar to the forming process discussed above, more ion migration may take part in filament growth and thus be responsible for a lower resistance in the LRS.

Therefore, the magnitude of the voltage applied during both switch ON and switch OFF procedures has a direct influence on the formation of filaments. The model established for ion migration depending on the applied voltage polarity and magnitude helps to understand the related phenomenon discussed here.

6.2.4 Delay time dependence

Figure 6.10 shows the dependence of the switch OFF procedure on the length of the delay time during negative voltage sweeps while keeping a constant time delay during positive voltage sweeps. In this way, the switch ON procedures were almost the same from cycle to cycle under a positive bias, as shown in Figure 6.10 (a): the switch ON voltage varied very little around 1 V and the ON resistance in the LRS remained the same. As already discussed above, different ON resistance levels programmed by the compliance current lead to different erase voltages V_{OFF} and erase currents I_{Erase}. Thus, by setting the same LRS with the same switching parameters during the positive sweeping cycles, the effect of different delay times (10 µs, 100 ms, 200 ms, 800 ms, 2 s) on the switch OFF process can be observed and this is indicated by the red arrow in Figure 6.10 (a). The final HRS after switch OFF is almost identical. Before the voltage reaches the turning point V_{OFF}, the LRS resistances are almost the same and independent of delay time. But above V_{OFF}, the delay time changes the erase voltage and erase current during the passage from the LRS to HRS. The erase voltage V_{OFF} and erase current I_{Erase} are plotted in red and blue, respectively, in Figure 6.10 (b) as a function of the time spent sweeping the negative voltage. A longer delay time helps reduce the erase voltage from -0.67 V (10 µs) to -0.50 V (2 s). Meanwhile, the erase current reduces from 900 µA to 450 µA as the delay time is increased. Based on this measurement, a rough conclusion may be drawn that switching OFF with short pulses requires a higher erase voltage V_{OFF} and a higher permitted current I_{Erase}. Generally speaking, delay times ranging from 10 µs to 2 ms had little influence on the final HRS in this measurement.

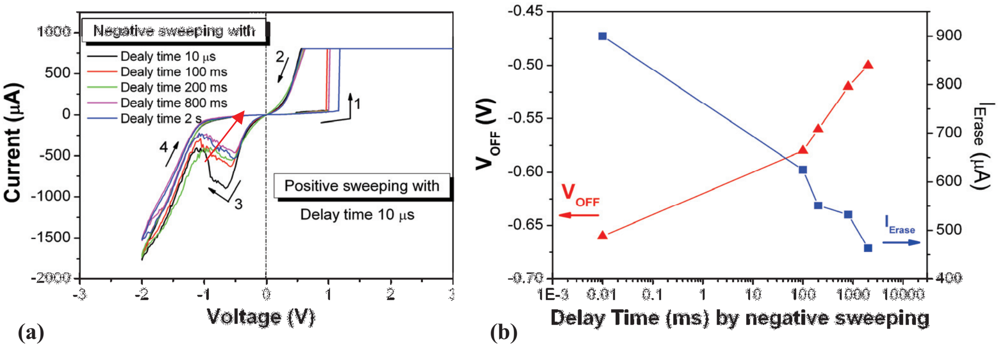

Figure 6.10: (a) Current-voltage measurements with same delay time during positive

voltage sweeping but different delay times during negative voltage sweeping. (b) Plot of the erase voltage and erase current versus delay time during negative voltage sweeping on a logarithmic scale. The measurements were done on a Cu/TiO_2/ Pt MIM crossed cell with a 60 nm thick ALD TiO_2 layer and a pad area of 2 x 3 μm^2.

6.2.5 Scalability

Resistive random access memory (RRAM) based on simple crossbar structures has attracted great attention because of the potential to produce high density, low power and more cost-effective memory devices. Apart from the switching mechanisms that have been discussed, scalability is an issue of great concern which could determine the commercial application of this technology in new memory devices. Memory cells with two thicknesses (27 nm and 60 nm) of TiO_2 have been studied. The electro-forming procedure depends on oxide thickness and pad size as discussed in section 6.1. But after forming, the resistive switching behaviour in devices with both thicknesses were observed to be very similar. Measurements on samples with the same 27 nm thick TiO_2 layer but with different crossed cell sizes (4, 25 and 100 μm^2) demonstrate that there is no pad size dependence of the resistive switching behaviour as shown in Figures 6.11 (a) and (b). Five continuous sweeping cycles between -3 V and +4 V were done on the same cell in order to ensure stable resistive switching as will be discussed. Figure 6.11 (a) shows that the resistive switching curves have almost the same shape on cells with 3 different sizes. In Figure 6.11 (b) is plotted the mean value and standard deviation of the OFF (black) and ON (red) resistances at 0.1 V calculated from the curves in plot (a). The OFF resistances do vary but are still within an order of magnitude larger than 1 MΩ. The ON resistances in red for three pad sizes remained almost the same around 2 kΩ. The fact that the resistive switching behaviour is independent of oxide thickness and pad size after electro-forming supports the idea that a local conductive path is responsible for the resistive switching of the memory cell. The forming process creates a certain local path, along which the ions migrate under the applied electrical field and results in the formation and rupture of filaments. Therefore, the dimension of such a locally conductive path should be a critical parameter in deciding the smallest functional memory cell size that can be made. Kozicki el. al, have already demonstrated Ag-Ge-Se solid electrolyte-based resistive switching cells down to 40 nm with a low programming current of 10 μA and good endurance beyond 10^{11} cycles. Further investigations on nanometre scale memory cells are needed to explore the limitations of reliable RRAM devices based on Cu/TiO_2/Pt structures.

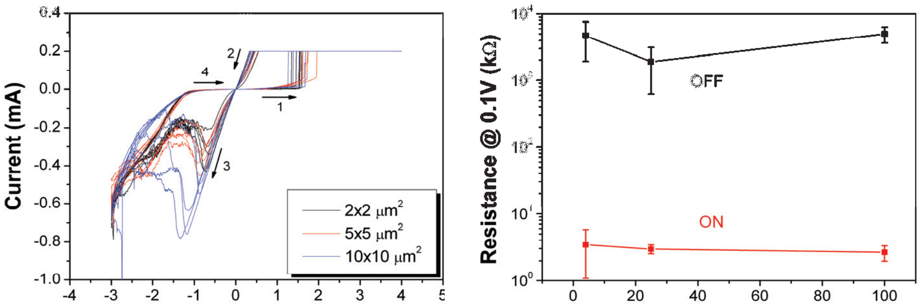

(a) (b)

Figure 6.11: (a) Current-voltage plot on cells with 27 nm thick TiO_2 layer but with three different pad sizes: 4 μm^2 (black), 25 μm^2 (red) and 100 μm^2 (blue). (b) Mean values and standard deviations of OFF resistances (black) and ON resistances (red) at 0.1 V calculated from the 5 repeated *I*(*V*) cycles on cells in the 3 different pad sizes of graph (a).

6.2.6 Endurance and retention of HRS and LRS

Good endurance is also a basic requirement for the commercial application of resistive switching memory devices. Until now, most reports of resistive switching in TiO_2 thin films have described unipolar resistive switching. According to published data, the endurance measured in TiO_2 is no more than 80 cycles. [DSJ 2007]. The switching mechanism in unipolar switching is classified as a fuse and anti-fuse effect. High temperatures can be generated by the large currents that flows through the filaments formed with very low resistances and this leads to the thermal breaking of such conductive paths. Such a process is very destructive of the film and this could be the reason for the poor endurance capability. In this work, the endurance of resistive switching was distinctly improved as shown in Figure 6.12 (a). More than 1,600 quasi-static swept cycles were performed on a Cu/TiO_2/Pt memory cell with 25 μm^2 pads. The current at 0.1 V for every 100 cycles was taken from both OFF (black) and ON (red) states. Both resistance states remained stable with swept cycles. The ratio of high resistance to low resistance is more than 4 orders of magnitude (2 x 10^4). The reason for the improvement in the endurance can be attributed to the bipolar switching characteristics related to ion migration. Copper has a good diffusion capability in many solid materials. In this study Cu atoms were detected by ToF-SIMS in the cell after switching as shown in Figure 6.2 (a). A structural change often accompanied unipolar resistive switching in Pt/TiO_2/Pt cells such as bubbles or local porosity, but none of this was observed in the Cu/TiO_2/Pt cells. It is very possible that Cu migration itself or the associated migration of O results in less damage to the memory cells than fuse and anti-fuse resistive switching.

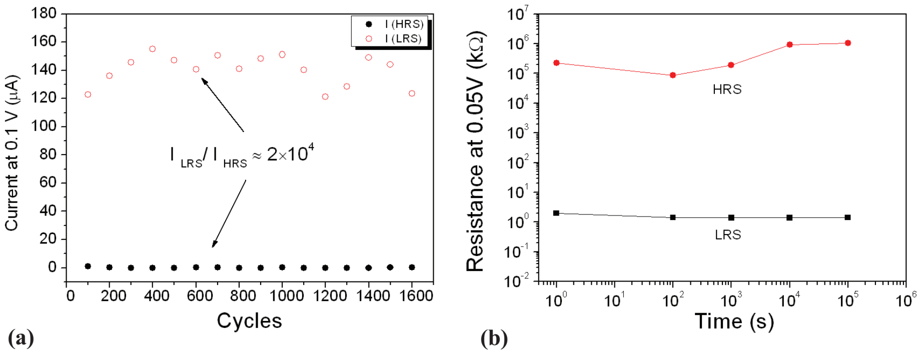

Figure 6.12: (a) Endurance test on a Cu/TiO_2/Pt memory cell with 27 nm thick TiO_2 and a pad size of 5 x 5 μm2. (b) Retention of both LRS (black) and HRS (red) read with 50 mV applied to the cell with 27 nm thick TiO_2 and a pad size of 3 x 3 μm^2.

Good retention characteristics are another basic requirement for non-volatile storage. By applying a small voltage, the resistance states can be read out as the magnitude of the current, as long as the cell has a sufficient OFF/ON ratio. As an example, both resistance states, HRS in red and LRS in black in Figure 6.12 (b), were read by 50 mV pulses. Their states remained stable at room temperature for more than 10^5 seconds with an OFF/ON ratio of more than 4 orders of magnitude. With such a large margin between the high and low resistance states, some degree of variation of the resistance (here increasing the HRS with time) does not change the state of the stored information as a “0” or “1”.

6.3 Temperature-dependence of resistance states

To further characterize the switching mechanism, the temperature dependence of the resistance and the *I*(*V*) characteristics of the various resistance states, including the initial, HRS and LRS states, were studied. Several models have already been proposed to describe electrical conduction in solid materials as listed in table 2.1 in chapter 2. Current transport through the metal-insulator-metal (MIM) stack cell is related to either interface or bulk characteristics. Important parameters like the barrier in the metal-insulator interface or the barrier between charge trap sites in the bulk depend on the nature of defects in the corresponding region. Moreover, the current flow is also related to temperature, which has a great impact on the density and mobility of charge carriers. Therefore, temperature measurements can be applied and help understand the model of charge transportation in the cell through the interface or bulk.

Figure 6.13 (a) sketches the structure of the MIM cell used for the temperature measurements. A second Pt thin film of 100 nm thickness protects the Cu from fast oxidation at the higher temperature up to 200°C. Similar resistive switching behaviours were observed in the ALD TiO_2 thin films with Cu top electrodes as shown in Figure 6.13 (b). The switching procedures after electro-forming are indicated with numbers 1 to 5 in different colours. Starting with a half cycle (No.1 in black) and sweeping the positive bias on the top Cu electrode, the resistance state switched from HRS to LRS at around 0.8 V with a compliance current of 3 mA. The LRS exhibits a linear current-voltage characteristic. The bipolar nature of the switching can be proved in cycle 2 shown in red (No. 2), where the switch OFF current I_{Erase} is around -2.5 mA, lower than the compliance current. Cycles 2, 3 and 4 are sequential half cycles with the forward and reverse bias swept between 0 and the maximum negative voltage: -1.0 V (No. 2 in red), -1.3 V (No. 3 in green) and -1.5 V (No. 4 in blue). It should be noted that every forward sweep of the next cycle runs along the same current I as the last reverse sweep: the I curve of cycle 3 in green from 0 to -1.0 V is the same as the I curve of cycle 2 in red from -1 V to 0 and the I curve of cycle 4 in blue from 0 to -1.3 V is the same as the I curve of cycle 3 in green from -1.3 V to 0. This demonstrates that the OFF state of every cycle is stable unless a larger negative voltage is applied. At -0.5 V, the linear ohmic LRS of cycle 2 turns to the HRS state abruptly. Afterwards, cycles 3 and 4 with larger negative sweep ranges lead to a further switch OFF process, where the resistance of the HRS state can be further enhanced. Obviously, here a higher negative voltage results in a higher HRS. The 5th cycle in yellow shows the non-linear current-voltage characteristic in the LRS state, resulting from the much lower compliance current of 500 μA. On the other hand, the LRS of cycle 5 is very similar to the HRS before switch ON in cycle 1. Therefore, whether a resistance state is HRS or LRS is sometimes relative. Muti-level switching of the cell implies that many intermediate states between the highest HRS and the lowest LRS can be set. Although several papers have compared the HRS and LRS states with temperature measurements or other methods, these intermediate states are still not well understood. In this section, different activation energies for charge transport in the initial, OFF and 3 different ON states can be compared with temperature measurements.

Five Pads of the same size and on the same sample were chosen. One of them remained in the initial state. The 2nd was set to the OFF state (HRS). The other 3 were set to ON states (LRS) with different resistances. These 5 resistance states are plotted in different colours on the same graph in Figure 6.14 (a). Afterwards, current-voltage measurements were carried out on every cell at different temperatures from room temperature at 25°C to 185°C with a step size of 20°C. The current-voltage characteristics of these 5 states are depicted at increasing temperature in Figures 6.14 (b) to (f). Among them, non-linear $I(V)$ curves were observed in this temperature range in those cells in the initial (Figure 6.14 (b)), OFF (Figure 6.14 (c)) and ON1 (Figure 6.14 (d)) states. The cell in the ON1 state shows nearly linear $I(V)$ conduction above 165°C. The other two cells (Figures 6.14 (e) and (f)) in the ON2 and ON3 states show linear $I(V)$ characteristics, suggesting ohmic conduction through the MIM cells.

Moreover, the cells in the initial, OFF, ON1 and ON2 states exhibit enhanced current conduction at increasing temperature, which implies semiconducting conduction. Only the cell in the ON3 state shows a lower conductance at higher temperature and the conduction was permanently interrupted above 165°C.

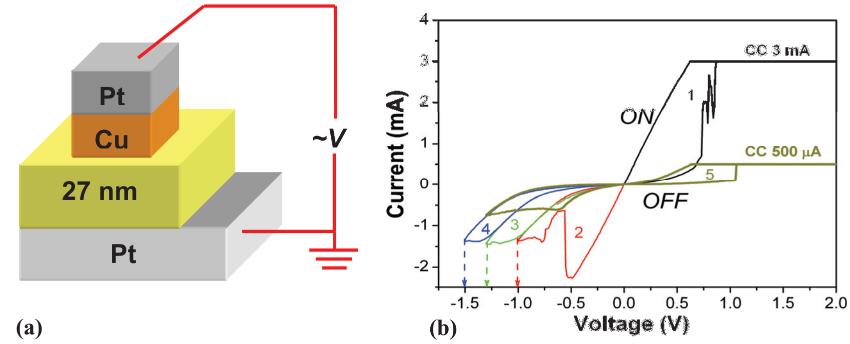

(a) (b)

Figure 6.13: (a) Cell structure for temperature measurements. (b) Typical resistive switching curves at room temperature on a Pt/Cu/TiO_2/Pt MIM cell with 27 nm sputtered TiO_2 under the top electrode in a 50 x 50 μm^2 size.

In order to compare the temperature dependence of the electrical conduction, the resistances at 50 mV were taken from all 5 cells in different resistance states and plotted in Figure 6.15 (a) and (b). The resistances at room temperature reduce as follows: R(initial) > R(OFF) > R(ON1) > R(ON2) > R(ON3). At room temperature, the resistance of the initial state (~ 0.3 GΩ) is more than 3 orders of magnitude larger than of the resistance of the OFF state (~ 6,000 Ω) in Figure 6.15 (a). But this very large difference decreases dramatically with temperature and, at 185°C, both resistances are very close to each other at around 300 kΩ. Three ON states have much lower resistances at room temperature compared with the initial and OFF states. According to the temperature dependence of the resistances from ON1 to ON3, a transition of the LRS conduction mechanism from semiconducting to metallic is observed.

Many metals exhibit a linear dependence of electrical resistance as a function of the temperature (K) near room temperature which can be described as follows:

$$R = R_0\left[\alpha(T - T_0) + 1\right] \qquad 6.5$$

where T_0 is room temperature, R_0 is the electrical resistance at T_0, α is the temperature coefficient indicating the rate of change of resistivity per unit temperature. Typical temperature coefficients of bulk copper and silver are similar ~ 3.9 x 10^{-3} K^{-1}. [80, 81] The temperature coefficient α of the filament in state ON3 can be calculated as 1 x 10^{-3} K^{-1}, which is close to the temperature coefficient α = 2.5 x 10^{-3} K^{-1} of a Cu nanowire of diameter ≥ 15 nm. [82] Thus, it can be concluded that the ON3 filament is Cu, which confirms the validity of a filament model based on Cu migration as discussed above.

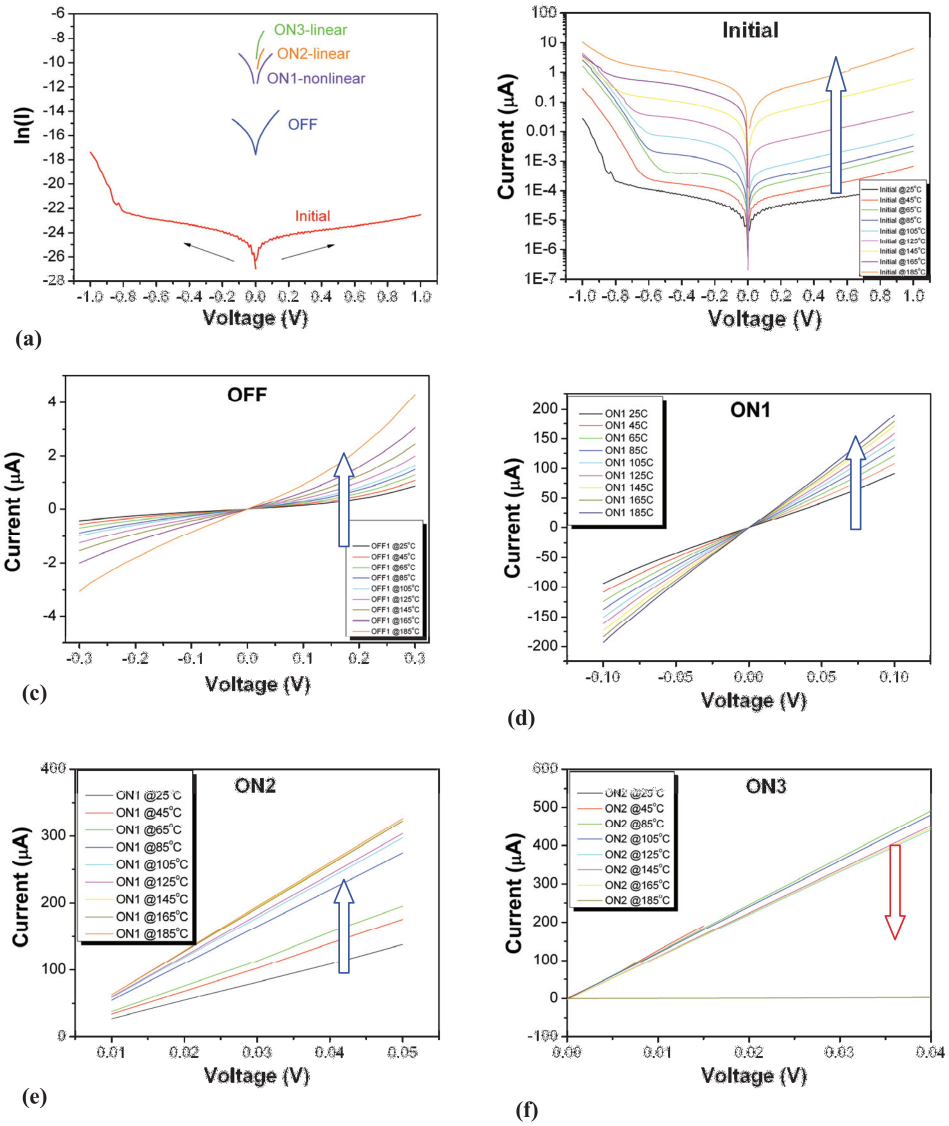

Figure 6.14: (a) Five different resistance states set in five cells: Initial (red), OFF (blue), ON1 (violet), ON2 (orange), ON3 (green). Temperature dependence of the current-voltage curve corresponding to the different resistance states: (b) Initial, (c) OFF, (d) ON1, (e) ON2, (f) ON3.

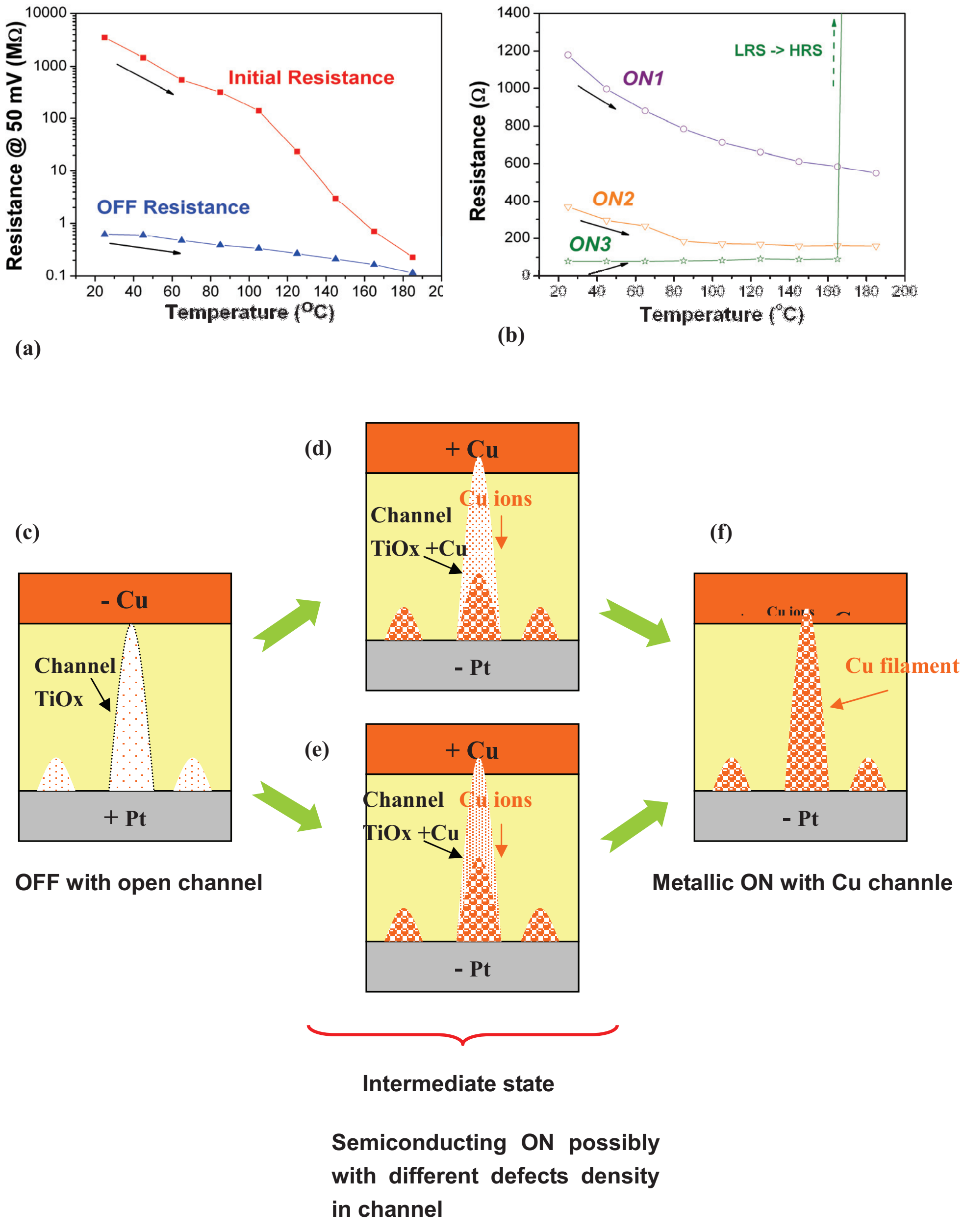

Figure 6.15: Temperature dependence of the resistances at 50 mV of (a) initial (red) and OFF (blue), (b) ON1 (violet), ON2 (orange) and ON3 (green). Sketch of the various resistance states of (c) OFF with open channel, (d) and (e) semiconducting ON state possibly with different defect densities in the channel, (f) metallic filament filled by Cu in the channel.

From the SIMS results and the temperature coefficient, we confirm the role played by Cu migration in the Cu filament. The question is, why do the two ON states with higher resistances than the metallic ON state have a semiconducting character? These two cells of ON1 and ON2 in semiconducting states could be intermediate states between the OFF state and ON1 state of the Cu filament. In such a solid electrolyte system, the Cu filament grows from the cathode (Pt) towards the anode (Cu) after the Cu ions are reduced and accumulated from the cathode. The channel provides a migration path for the Cu ions, which migrate from the anode (Cu) to the cathode (Pt) during the SET procedure. Therefore the semiconducting ON states could result from “frozen-in” Cu ions in the channel between the grown Cu filament tip and the anode, as sketched in Figures 6.15 (d) and (e). The density of Cu and possibly other defects in this region could play an important role in current conduction inside the cell and is represented in Figures 6.15 (d) and (e) in the form of different point densities in the channel. More calculations and some estimates will be performed in the next sections, from which a model can be better formulated. The discussions are all based on the fundamental conduction mechanisms listed in table 2.1 which could operate in MIM structures.

6.3.1 Initial state

Current conduction in a Cu/TiO_2/Pt MIM cell in the initial state depends on the polarity of the voltage, as shown in Figure 6.14 (b). Conduction of this type is generally believed to be controlled by interface states or electrode limited. Normally, either Schottky emission or tunnelling can dominate current conduction in the interface area of such a MIM structure. But simple tunnel conduction has a weak temperature dependence, whereas Schottky emission is strongly dependent on temperature. Schottky conduction under the higher electric field at the interface between the electrode and semiconductor or insulator layer can be described as follows:

$$I = A \cdot J = A \cdot A^{*}T^{2} \exp\left(\frac{1}{kT}\sqrt{\frac{q^{3}}{4\pi\varepsilon_{0}\varepsilon d}} \cdot \sqrt{V} - \frac{q\Phi_{B}}{kT}\right) \qquad 6.6$$

where A is the pad area, J is the current density, A^* is the Richardson constant, T is the temperature, k is the Boltzmann constant, ε_0 is the vacuum permittivity, ε is the optical dielectric constant or high frequency dielectric constant, which is the square of the refractive index (n^2) of the layer material TiO_2, d is the depletion width, V is the voltage applied through the structure, and Φ_B is the Schottky barrier height (SBH).

The linear dependence of the semilog current ln(I) on $V^{1/2}$ can be described by converting equation 6.6 in the Schottky model into:

$$\ln I = \ln(AA^{*}T^{2}) + \frac{1}{kT}\sqrt{\frac{q^{3}}{4\pi\varepsilon_{0}\varepsilon d}}\cdot\sqrt{V} - \frac{q\Phi_{B}}{kT} \tag{6.7}$$

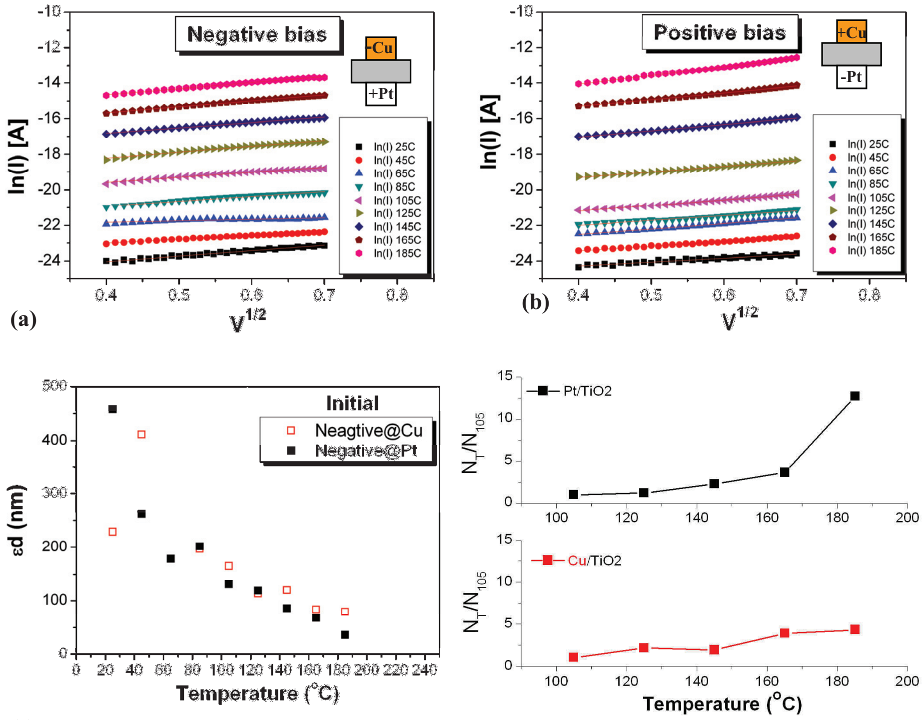

(a) (b)

(c) (d)

Figure 6.16: Temperature dependence of current-voltage characteristics plotted as ln (I) vs $V^{1/2}$ for (a) negative and (b) positive bias. (c) Product εd extracted from the the slope. (d) Increasing rate of charge density at different temperatures (N_T/N_{105}) in the interface region of both electrodes compared with that at 105 °C.

According to equation 6.7, the linear behaviour of the measured ln(I) versus $V^{1/2}$ curve at voltages between 160 mV and 460 mV or between -160 mV and -460 mV is consistent with Schottky emission from Cu or Pt electrodes, which is shown in Figure 6.16 for current conduction in the temperature range from 25°C to 185°C under a negative (a) and positive (b) bias. The polarities of the applied voltage are sketched in the insets of Figures 6.16 (a) and (b), indicating that the electron injected from the Cu top electrode into the bulk TiO_2 film under a negative bias and from the Pt bottom electrode into the TiO_2 under a positive bias. The slope of this curve is:

$$slope\left(\frac{\ln I}{\sqrt{V}}\right) = \frac{\beta_s}{kT} = \frac{1}{kT}\sqrt{\frac{q^{3}}{4\pi\varepsilon_{0}\varepsilon d}} \tag{6.8}$$

$$\beta_s = \sqrt{\frac{q^3}{4\pi\varepsilon_0 \varepsilon d}} \qquad 6.9$$

where β_s is the Schottky constant. The slopes at different temperatures from 25°C to 185°C can be extracted from the measurements results plotted in Figure 6.16 (a) for negative polarity and in (b) for positive polarity. Thus, the magnitude of εd can be calculated with equation 6.8 and this is plotted in Figure 6.16 (c) as a function of the temperature. The value of εd decreases with increasing temperature. From 105°C to 165°C the values under both polarities at the same temperature were similar, having a weak polarity dependence. If the optical dielectric constant ε is known, then the depletion width d can be calculated.

The optical dielectric constant ε can be obtained as the square of the refractive index n, which is n=2.5 measured by Ellipsometry on a 27 nm thick sputtered TiO_2 thin film. On the basis of the literature, the refractive index n can vary between 2.2 to 2.7 corresponding optical dielectric constants ε from 4.84 to 7.29, depending to a significant extent on the phase composition of TiO_2.[83, 84, 85] Amorphous films have the lowest refractive index and crystalline anatase and rutile have higher values.

With the optical dielectric constant ε = 6.25 based on Ellipsometry measurements, the depletion width d (Table 6.1) calculated from the results in Figure 6.16 (c) at temperatures between 105 °C and 185 °C are all lower than the TiO_2 thickness of 27 nm and they decrease with increasing temperature

Table 6.1: Depletion width d at both interfaces calculated with the optical dielectric constants ε = 6.25 of TiO_2 compared to the measured refractive index n=2.5.

***T* (°C)**	**105**	**125**	**145**	**165**	**185**
***d* (Cu/TiO_2)nm**	26.4	18.1	19.1	13.4	12.7
***d* (Pt/TiO_2)nm**	20.8	19	13.7	10.9	5.8

The reduction of the depletion width d with increasing temperature may result from a change in charge density in the depletion region, which is deduced from the following calculations. In a typical Schottky diode, the depletion width d in the full depletion approximation can be expressed as follows:

$$d = \left[\frac{2\varepsilon_r}{qN}(V_{bi} - V_A)\right]^{1/2} \qquad 6.10$$

where ε_r is the static dielectric constant of TiO_2 and N is the space charge density or ionized dopant density in the depletion region. V_{bi} is the built-in voltage which depends on the band bending caused by the alignment of the two different Fermi levels in the two materials in contact, while V_A is the applied voltage. A higher temperature can help to release trapped charge and leave N ionized sites behind in the depletion region, therefore a higher N leads to a thinner depletion width d. This could be one way of explaining the reduction of εd indicated in Figure 6.16 (c) by assuming the dielectric constant ε_r remains unaffected by temperatures. Therefore, the density in the depletion region from a temperature of 105 ^{o}C to 185 ^{o}C can be obtained by transforming equation 6.10 into:

$$N = \frac{2\varepsilon_r (V_{bi} - V_A)}{qd^2} \qquad 6.11$$

Thus, the ratio of charge density N_T at temperature T to N_{105} at 105 ^{o}C can be expressed as:

$$\frac{N_T}{N_{105}} = \frac{d_{105}^2}{d_T^2} \qquad 6.12$$

Assuming the dielectric constant doesn't change in this temperature range, then the ratio of N_T/N_{105} is:

$$\frac{N_T}{N_{105}} = \frac{d_{105}^2}{d_T^2} = \frac{(\varepsilon d_{105})^2}{(\varepsilon d_T)^2} \qquad 6.13$$

Using the calculated values of εd, the charge density in the depletion layer is plotted against temperatures in Figure 6.16 (d), starting at a temperature of 105 ^{o}C. The red lines are for Cu/TiO$_2$ and the black lines are for Pt/TiO$_2$ interface regions. At both electrodes interface regions, the charge density increases with increasing temperature, but the change from 105 ^{o}C to165 ^{o}C is lower than one order of magnitude. It is well known that TiO$_2$ is normally an n-type oxide containing oxygen vacancies which have significant influence on the electrical properties. Therefore, it is possible that more trapped charges in the interface region are released from such intrinsic defects with an increasing in temperature, resulting in a higher space charge density N_T in the depletion region.

The activation energy E_a can be obtained by fitting ln(I/T^2) to a straight line when plotted against 1000/T, as done in Figures 6.17 (a) and (b) corresponding to conduction with a negative and positive bias applied to the Cu top electrode. The slope of the straight lines in the ln(I/T^2) vs. 1000/T plots with different voltages can be expressed as follows on the basis of the Schottky model:

$$\ln(\frac{I}{T^2}) = \ln(AA^*) + \frac{1}{kT}\sqrt{\frac{q^3}{4\pi\varepsilon_0 \varepsilon d}} \cdot \sqrt{V} - \frac{q\Phi_B}{kT} \qquad 6.14$$

$$slope[\frac{\ln(\frac{I}{T^2})}{\frac{1000}{T}}] = \frac{E_a}{1000k} = \frac{\beta_s \sqrt{V} - q\Phi_B}{1000k} \qquad 6.15$$

Using equation 6.15, the activation energy E_a from 105 ^{o}C to 165 ^{o}C can be calculated and plotted as a function of $V^{1/2}$ in Figure 6.17 (c), where the points in hollow red points depict E_a for a negative bias and the red points show Ea for positive bias. By extrapolating to V=0, the Schottky barrier height (Φ_B) of the Cu/TiO$_2$ interface (negative bias on Cu) is obtained as ~ 0.85 eV and the Schottky barrier height of the

Pt/TiO_2 interface (negative bias on Pt) is ~ 1.3 eV, which are very similar to the published values for SBHs for Cu/TiO_2 and Pt/TiO_2 interfaces.[86, 87, 88, 89, 90] The band diagram of the initial state of the Cu/TiO_2/Pt MIM cell is sketched in Figure 6.17 (d) because the TiO_2 is normally an n-type semiconducting oxide.[91, 92]

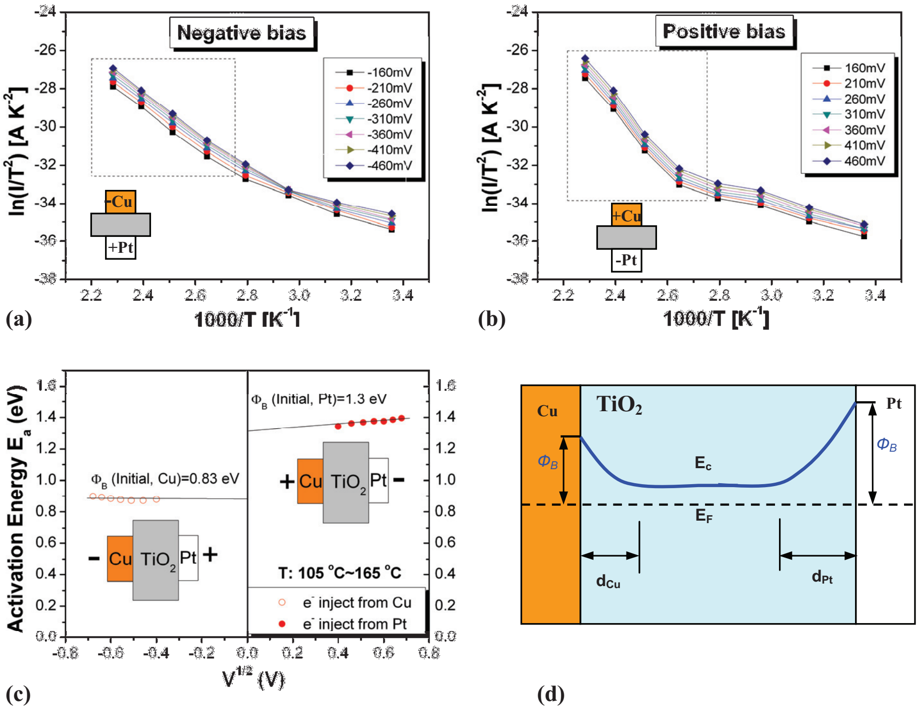

Figure 6.17: Temperature dependence of current-voltage characteristics plotted as ln (I/T^2) vs 1000/T for (a) negative and (b) positive bias on the Cu electrode. (c) Activation energy extracted from the function for $V^{1/2}$ for both negative and positive bias. (d) Band diagram for Schottky emission through the Cu/TiO_2/Pt sandwich cell.

6.3.2 OFF state

In this part, the temperature dependence of the OFF state is discussed.

The linear relation of ln(I) against $V^{1/2}$ at negative and positive polarities is shown in Figures 6.18 (a) and (b) and is consistent with a Schottky emission model from both electrodes. After linear fitting to straight lines in the range from 80 mV to 300 mV in both polarities, the slopes at different temperatures from 25°C to 185°C can be obtained in the same way as mentioned in the case of the initial state, which led to the value of εd shown in Figure 6.18 (c). Here the value d is the depletion width (in nm) of the SBH in the interface region of the Cu or Pt electrode in the OFF state. With the filament model, repeated resistive switching was carried out through the growth (ON) and retrace (OFF) of Cu filaments in local channels between both electrodes created after the electro-forming process. Hence, in the OFF state, the channel does not contain Cu but has a better conductivity than that in the initial state, which implies a very defective channel of TiOx after the RESET procedure.

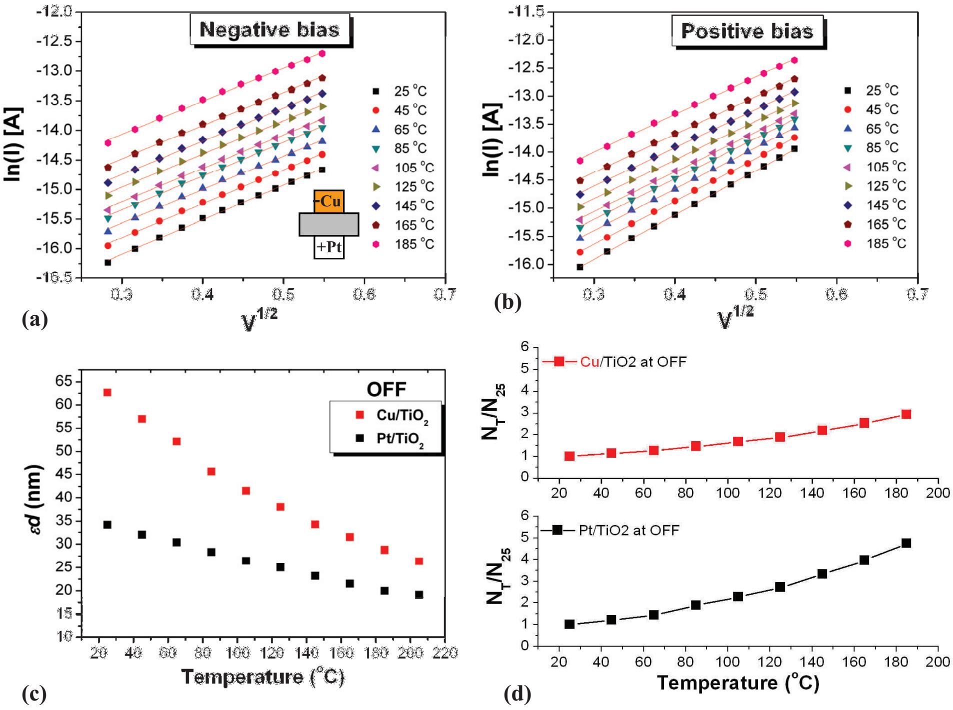

Figure 6.18: Temperature dependence of current-voltage characteristics plotted as ln(I) vs $V^{1/2}$ for (a) negative and (b) positive bias on the Cu electrode. (c) εd product extracted from the equation of the slope. (d) Increasing rate of the charge density at different temperatures (N_T/N_{25}) in the interface region of both electrodes compared to that at 25 °C.

Until now little experimental evidence about the exact composition of the filaments in the OFF and ON states are available for this case. However, Cu should contribute to conduction in the resistive switching of the Cu/TiO_2/Pt system. No bubbles were observed in the top Cu electrodes during switching in the high current range (> 1 mA) compared with the appearance of bubbles during resistive switching in the Pt/TiO_2/Pt system. ToF-SIMS (Figure 6.3) has proved the existence of Cu in the film after switching. Thus, if it is assumed that Cu is traced back from the channel after switching OFF, a channel is left which is composed only of TiO_2 or TiO_x. As already mentioned above, the refractive index n is higher in the crystalline phase and depends on the composition of TiO_2, asreported in many works. Zakrzewska et al. report the refractive index of sputtered stoichiometric and non-stoichiometric TiO_2.[93] It is found that the more TiO_2 departs from stoichiometry, the higher is the refractive index of the thin film. The range of such variation can be between 2.3 and 2.5 according to the composition of TiOx. The $n = 2.5$ measured on our TiO_2 thin films is a little larger than this, possibly because of the different deposition conditions. Because of the difficulty in exactly knowing the phase and composition of local filaments, an estimation of the depletion width d in the channel in the OFF state can be made by using a refractive index of 2.5 according base values reported in the literature. The results of d at different temperatures are listed in Table 6.2.

Table 6.2: Depletion width d in the OFF state using the same refractive index n as that in the initial state of TiO_2, assuming its interface has similar composition TiO_x ($x \leq 2$) in both cases.

T (^oC)	**25**	**45**	**65**	**85**	**105**	**125**	**145**	**165**	**185**
d (Cu/TiO_2)nm	10	9.1	8.3	7.3	6.7	6.1	5.5	5	4.6
d (Pt/TiO_2)nm	5.5	5.1	4.9	4.5	4.2	4.0	3.7	3.4	3.2

According to equation 6.10, the decrease of the depletion width d of the Schottky barrier in Table 6.2 can be attributed to an increasing in the carrier density N in the interface region with increasing temperature. The increasing rate of space charge density formed in Cu/TiO_2 and Pt/TiO_2 barriers in the OFF state (HRS) are plotted in Figure 6.18 (d), obtained from equation 6.13 by comparing the space charge density at room temperature (25 ^oC). The charge density increases with increasing temperature, but the rates are still lower than one order of magnitude.

Compared with the depletion width d in the initial state (Table 6.1), the d in the OFF state (Table 6.2) is much narrower, possibly because of the much higher defects (TiOx) in the interface region between Cu and the TiOx channel after the RESET procedure. On the other hand, more surface states can also lead to a decrease in the Schottky barrier height as well as the built-in voltage V_{bi}.

The reduction of Schottky barrier in this measurement is supported by fitting a straight line to the ln (I/T^2) versus 1000/T curve, as shown in Figures 6.19 (a) and (b). Two stages can be indentified with different slopes in the temperature range below 85 ^oC and that above 85 ^oC. The calculated activation energy E_a as a function of voltage and a sketch of the polarity are plotted in Figure 6.19 (c). The red square points indicate the E_a in the higher temperature range between 105 ^oC and 165 ^oC for both bias polarities. By extrapolating the straight line of E_a to $V = 0$, the Schottky barrier height SBH at both interfaces are independent of polarity at ~ 0.1 eV. In the same way, the SBH at both interfaces in the lower temperature range between 25^oC and 85 ^oC were almost independent of polarity at ~0.06 eV. Because of the uncertainty surrounding the exact filament diameter A which decides resistive switching or the current conduction in the OFF state, the Richardson constant A* can be calculated from the intersection of the linear fit with the axis by assuming different filament sizes of 10 x 10 nm^2, 50 x 50 nm^2 and 100 x 100 nm^2 as shown in Figures 6.20 (a) and (b) below 85 ^{o}C and above 85 ^{o}C, respectively.

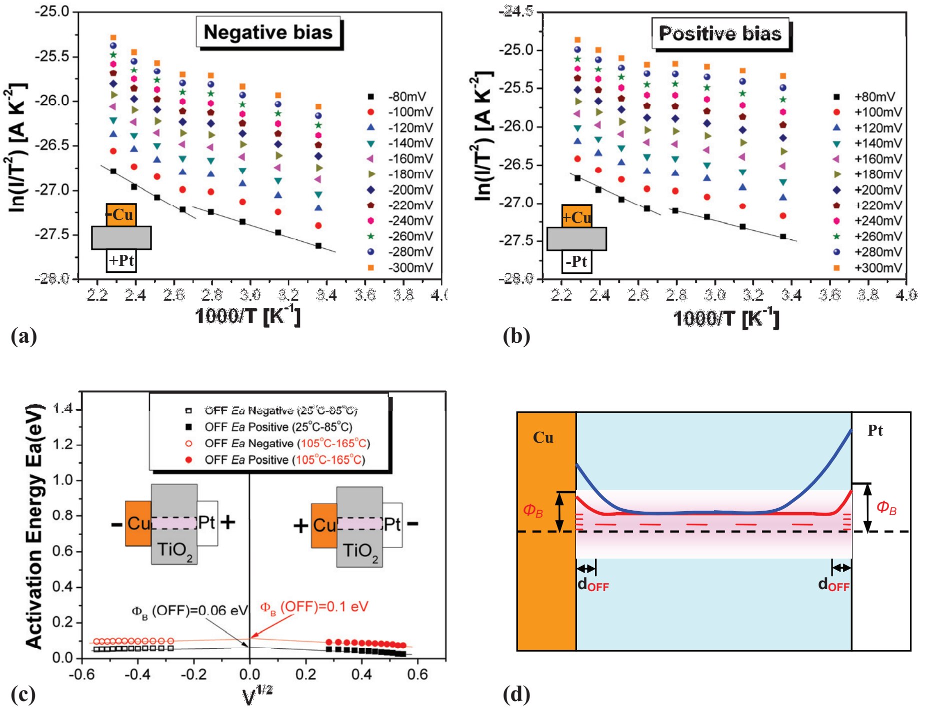

(a) (b) (c) (d)

Figure 6.19: Temperature dependence of current-voltage characteristics plotted as ln(I/T^2) vs 1000/T for (a) negative and (b) positive bias applied to the Cu electrode. (c) εd extracted from the equation of the slope. (d) Band diagram showing the lowering of the SBH in the OFF state.

We assume that the electro-forming process creates a channel with lots of structural defects in the polycrystalline TiO_2 thin film. Such defects facilitate the migration of Cu ions and possibly O ions, under the action of the applied electrical field in the formed Cu/TiO_2/Pt cell, more so than in the initial state. Figure 6.19 (d) sketches the band diagram of the cell in the OFF state based of the above considerations. The light pink region sketches the channel for growth or dissolving of filament by ion migration. The red curve indicates the band diagram in the OFF state with a much lower SBH of 0.1 eV between 105 ^{o}C and 165 ^{o}C than in the initial state, depicted in blue. The lowering of the barrier height can be attributed to surface states at the interface, which could be structural defects of the channel created by ion migration during electro-forming and RESET procedures. The short red lines under the conduction band indicate the electric defect states in the form of oxygen vacancies in the bulk.

Theoretically, the defective channel of TiOx has a great influence on electrical conduction by moving the Fermi level close to the conduction band and by narrowing the depletion width in the interface due to the increased defects (oxygen vacancies) compared with the initial state. Calculations based on a Schottky model suggest that this could be due to a similar source: The reduction of the Schottky barrier height to 0.1 eV from 0.83 eV in Cu and 1.3 eV in Pt is due to the reduction of the Fermi level between the metal electrode and the defective TiOx channel. Accordingly, the built-in voltage V_{bi} is also reduced. Both V_{bi} and the increased charge density N in the interface region contribute to a reduction in the depletion width d of the Schottky barrier from 0.1 eV on both sides in the OFF state from 0.83 eV in Cu and 1.3 eV in Pt, based on equation 6.10.

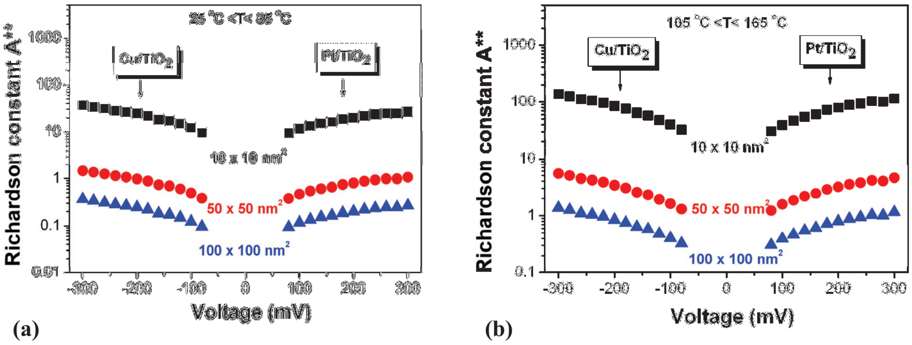

(a) (b)

Figure 6.20: Richardson constant A** at both electrodes at temperatures (a) from 25 °C to 85 °C and (b) from 105 °C to 165 °C by assuming different filament areas.

6.3.3 Three ON states

Three ON states with different resistances ($R_{ON1} > R_{ON2} > R_{ON3}$) were set on separate cells with a positive bias. The voltage sweep range for temperature measurements was limited to very narrow regions in order to protect the samples from sudden changes in the resistance state with increasing temperature.

ON1 state

Symmetric non-linear current-voltage $I(V)$ characteristics were measured at raised temperatures by sweeping the bias from 0 to 100 mV and from 0 to -100 mV, indicating non-ohmic conduction as shown in Figures 4.22 (a) and (b). Given the strong temperature dependence of the current, pure tunnelling conduction can be excluded. Thus, in this case, there are possibly three other kinds of current conduction mechanisms to consider: Schottky emission, Poole-Frenkel conduction and space charge-limited conduction (SCLC).

Schottky emission ?

The linear dependence of ln *I* on $V^{1/2}$ at higher voltages above 50 mV here could suggest Schottky emission from the electrodes as shown in Figures 6.21 (a) and (b) for both polarities.

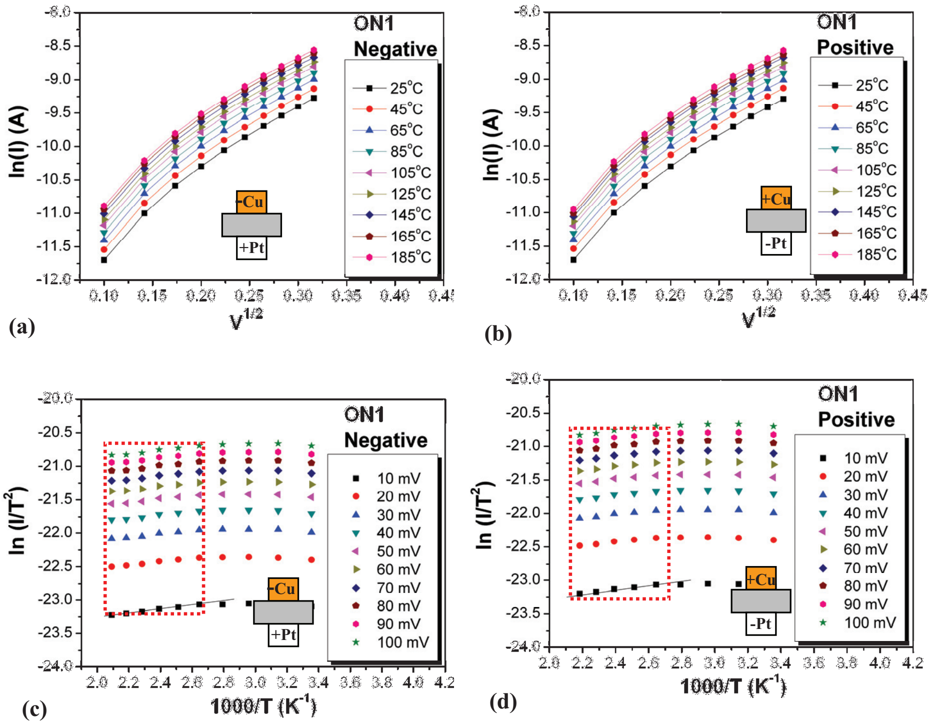

(a) (b) (c) (d)

Figure 6.21: Temperature dependence of current-voltage characteristics plotted as ln(*I*) versus $V^{1/2}$ for a (a) negative and (b) positive bias on the Cu electrode. Temperature dependence of current-voltage characteristics plotted as $\ln(I/T^2)$ versus 1000/*T* under (c) negative and (d) positive bias on the Cu electrode.

The corresponding slope of the straight line fit of $\ln I/T^2$ plotted against 1000/*T* must be negative because of the energy "expended" in overcoming the barrier to transport electrons. Based on the Schottky model, $\ln(I/T^2)$ was plotted against 1000/*T* in Figures 6.21 (c) and (d) for negative and positive bias, respectively, and it was found that the slope of the straight line fit over the whole voltage range at raised temperatures between 105°C and 185°C was positive, as indicated in the red dotted frames, which is unreasonable. Therefore Schottky emission can be excluded in the case of the ON1 state.

Poole-Frenkel emission?

Poole-Frenkel emission from localized states (traps) of the filament into extended states at higher energy can be expressed as follows:

$$I_{PF} = A\sigma_0 \frac{V}{d}\exp(-\frac{q\sqrt{\frac{q}{\pi\varepsilon\varepsilon_0 d}}\sqrt{V}+q\Phi_B}{kT}) = A\sigma_0 \frac{V}{d}\exp(-\frac{E_a}{kT}) \tag{6.16}$$

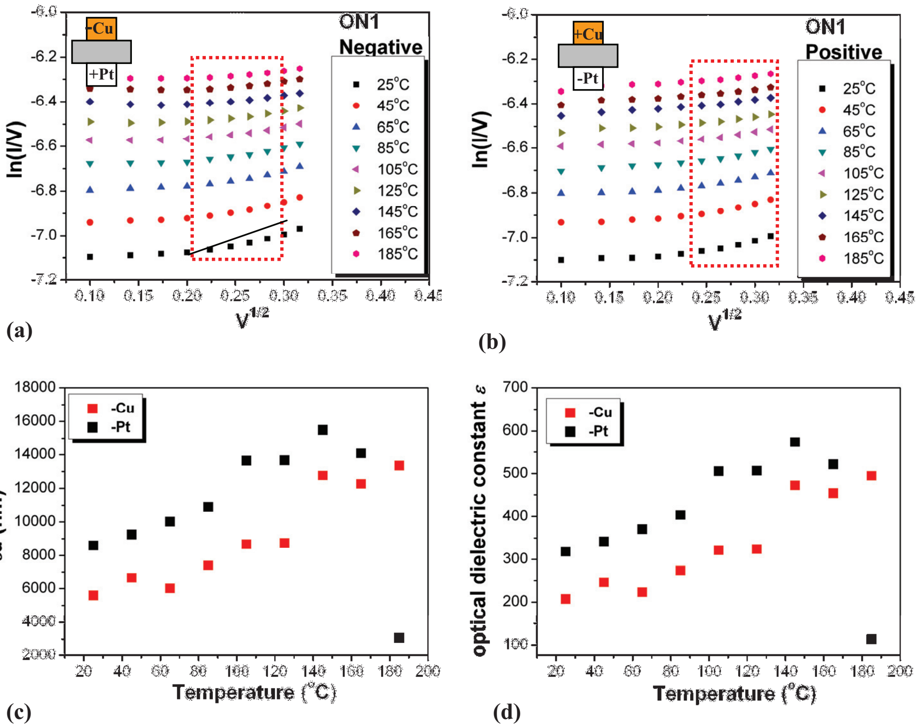

Figure 6.22: Temperature dependence of current-voltage characteristics plotted as ln(*I*) versus $V^{1/2}$ for (a) negative and (b) positive bias on the Cu electrode. (c) Product *εd* obtained from the slope of the linear fit to ln(*I*/*V*) versus $V^{1/2}$ based on plots (a) and (b). (d) Maximum *ε* calculated from the maximum possible *d* equal to an oxide film thickness of 27 nm.

where *A* is the lateral area of filament responsible for conduction on the basis of the filament model, *d* is the length of the filament, which is the same as the film thickness, σ_0 is a constant, Φ_B is the voltage barrier between the energy of the trap and the extended states at the edge of the energy band. The other parameters are the same as those in the equation for Schottky emission introduced above. Equation 6.16 can also be transformed to:

$$\ln(I_{PF}) = \ln(A\sigma_0 \frac{V}{d}) + \frac{q\sqrt{\frac{q}{\pi\varepsilon\varepsilon_0 d}}}{kT}\sqrt{V} - \frac{q\Phi_B}{kT} \qquad 6.17$$

$$slope(\frac{\ln\frac{I_{PF}}{V}}{\sqrt{V}}) = \frac{\beta_{PF}}{kT} = \frac{1}{kT}\sqrt{\frac{q^3}{\pi\varepsilon_0\varepsilon d}} \qquad 6.18$$

$$\beta_{PF} = \sqrt{\frac{q^3}{\pi\varepsilon_0\varepsilon d}} \qquad 6.19$$

Compared to the Schottky model, the coefficient β_{PF} is double the β_S found from equation 6.9 and 6.19. Figures 6.22 (a) and (b) plot ln(I/V) as a function of $V^{1/2}$ for the two polarities, with linear fits obtained at higher voltages between 70 mV and 100 mV. The slopes can be obtained at different temperatures, according to which the product of optical dielectric constant ε and thickness d can be estimated. This product is plotted in Figure 6.22 (c) with red squares for electron injection from Cu and black square for injection from Pt electrode. The maximum d can no be larger than the film thickness 27 nm. Therefore, the minimum optical electrical constant ε within the framework of the Poole-Frenkel model is extremely large, correspond to a refractive index n between 14 and 24. This inconsistency suggests that Poole-Frenkel conduction cannot be responsible for current transportation in the ON1 state.

Space charge-limited conduction?

Space charge limited conduction refers to carrier transport through the bulk materials and depends on the occupation of traps. This effect exhibits three different behabiours with increasing voltage: Ohm's law, trap-filled limited (TFL) conduction and the Child law. [94]

(1) In the low voltage region, the injected carrier density is lower than the thermally generated carrier density. Trapped carriers have less influence on current conduction under an electrical bias. Thus the conduction follows Ohm's law and can be expressed as follows:

$$I_{Ohm} = Aqn_0\mu\frac{V}{d_S} = Aq\mu\frac{V}{d_S}N_C\exp(-\frac{E_C - E_F}{kT}) \qquad 6.20$$

where A is the switching area which is a function of filament diameter, q is the elementary charge, n_0 is the thermally generated free carrier density in equilibrium and μ is the electron mobility. d_S is the thickness of the SCLC region. N_C is the equivalent density of states. From equation 6.20, the resistance of this stage R_{Ohm} can be described as following:

$$R_{Ohm} = \frac{V}{I_{Ohm}} = \frac{d_S}{qn_0\mu A} = \frac{d_S}{q\mu AN_C}\exp(\frac{E_C - E_F}{kT}) \qquad 6.21$$

(2) In the higher voltage region, the injected carrier density starts to dominate over the thermally produced carrier density. The unfilled traps in the bulk limit current conduction, by trapping a proportion of the free carries. This trap-filled-limited (TFL) current can be expressed as:

$$I_{TFL} = \frac{9}{8}A\varepsilon_0\varepsilon_r\mu\theta\frac{V^2}{d_S^3} \qquad 6.22$$

$$\theta = \frac{N_C}{N_T}\exp(-\frac{E_C - E_T}{kT}) \qquad 6.23$$

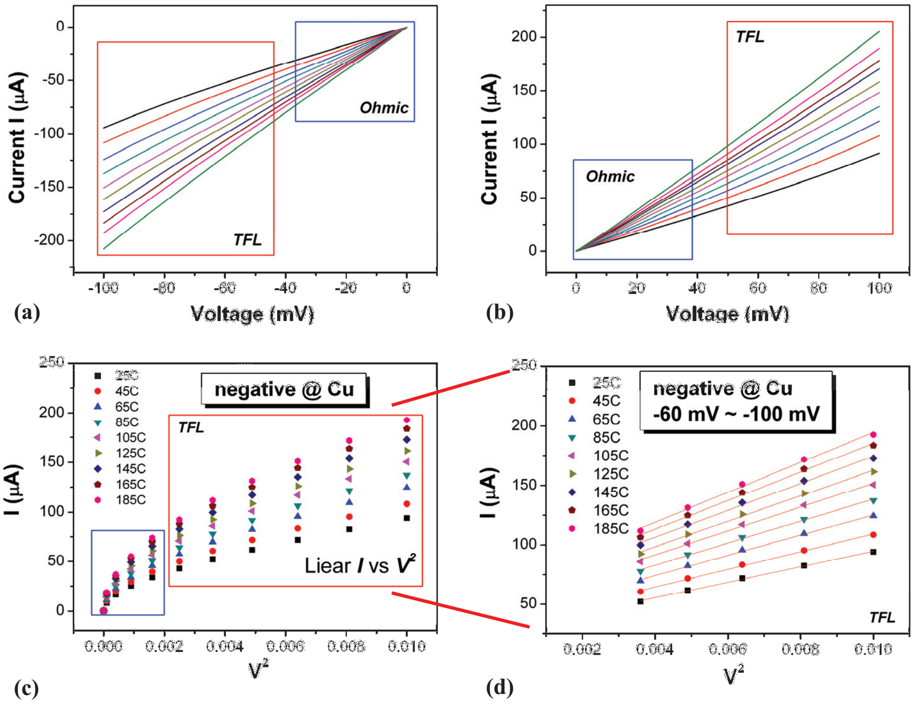

Figure 6.23: Symmetric temperature dependence of current-voltage characteristic plotted as *I* versus *V* for (a) negative and (b) positive bias on the Cu electrode. (c) Temperature dependence of current-voltage characteristic plotted as *I* versus V^2 for a negative bias on the Cu electrode. (d) Linear fitting of *I* as a function of V^2 between -60 mV and -100 mV.

The current is suppressed relative to the trap-free case by a factor θ resulting from the trapped injection electrons. ε_r is the static dielectric constant of the effective filament. N_T is the unfilled trap density in the bulk. E_T is the energy level of the trap sites in the band gap.

(3) The unfilled traps are filled with injected carries at increasing voltage and become part of a trap-free state. Therefore the parameter θ in equation 6.23 approaches unity which results in an enhancement of current conduction according to the Child law given by:

$$I_{Child} = \frac{9}{8} A\varepsilon_0\varepsilon_r\mu\frac{V^2}{d_S^3} \qquad 6.24$$

The symmetric current-voltage curves for both polarities are shown in Figures 6.23 (a) and (b). The conduction obeys Ohm's law in the lower voltage range between 0 V and ± 40 mV. A non-linear $I(V)$ characteristic appears at $V > 40$ mV or $V < -40$ mV. Because of the symmetry for both polarities, only the values for a negative bias are used in the following calculations and discussions. The $I(V)$ curves for a negative bias are transformed into $I(V^2)$ as shown in Figure 6.23 (c). We observe good linearity in the I versus V^2 curve in Figure 6.23 (d) between -60 mV and -100 mV which is consistent with the SCLC model.

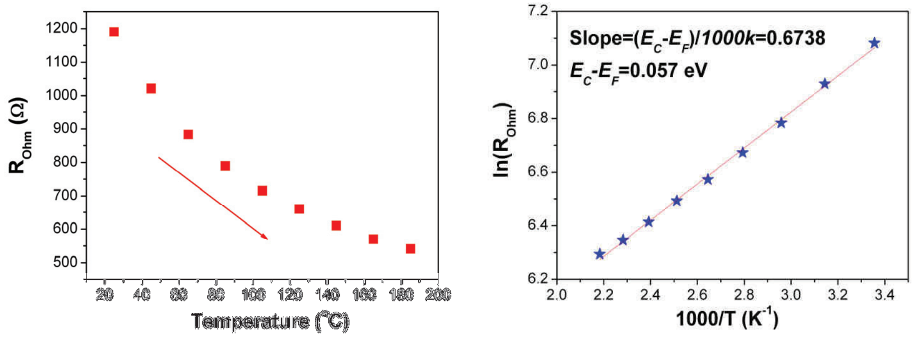

(a) **(b)**

Figure 6.24: Temperature dependence of resistance in the ohmic conduction regime at low voltages between 0 and -40 mV plotted as (a) R_{ohm} versus T and (b) $\ln(R_{ohm})$ versus 1000/T.

In the ohmic conduction region, between 0 V and -40 mV, the measured resistance R_{Ohm} reduces exponentially with temperature T, as shown in Figure 6.24 which is consistent with equation 6.21. The corresponding activation energy or the depth of the Fermi level is 0.057 eV, very close to the conduction band edge E_C.

In the space charge regime (from -60 mV to ~ -100 mV), current conduction can be formulated by combining equations 6.22 and 6.23 as:

$$I = \frac{9}{8} A\varepsilon_0\varepsilon_r\mu \frac{V^2}{d_S^3}\frac{N_C}{N_T}\exp\left(-\frac{E_C-E_T}{kT}\right) \tag{6.25}$$

$$\ln(I) = \ln\left(\frac{9}{8} A\varepsilon_0\varepsilon_r\mu \frac{V^2}{d_S^3}\frac{N_C}{N_T}\right) - \frac{E_C-E_T}{1000k}\frac{1000}{T} \tag{6.26}$$

Therefore, $\ln(I)$ should vary linearly with $1000/T$, the slope being given by $-(E_C-E_T)/1000k$. The experimental data confirm this linearity as shown in Figures 6.25 (a) and (b) for negative and positive bias, respectively. By fitting straight lines to both plots, the activation energies for trap carriers of both polarities are almost symmetric and decrease slightly as the magnitude of voltage increase, as seen in the plotted of Figure 6.25 (c). The weak voltage dependence of the activation energy here may be due to a voltage dependence of the carrier mobility μ, which in the above discussion has been regarded as constant and independent of temperature and voltage. Normally, the carrier mobility μ can be described as:

$$\mu(E.T) = \mu_0 \exp\left(-\frac{\Delta}{kT}\right)\exp(\gamma\sqrt{E}) \tag{6.27}$$

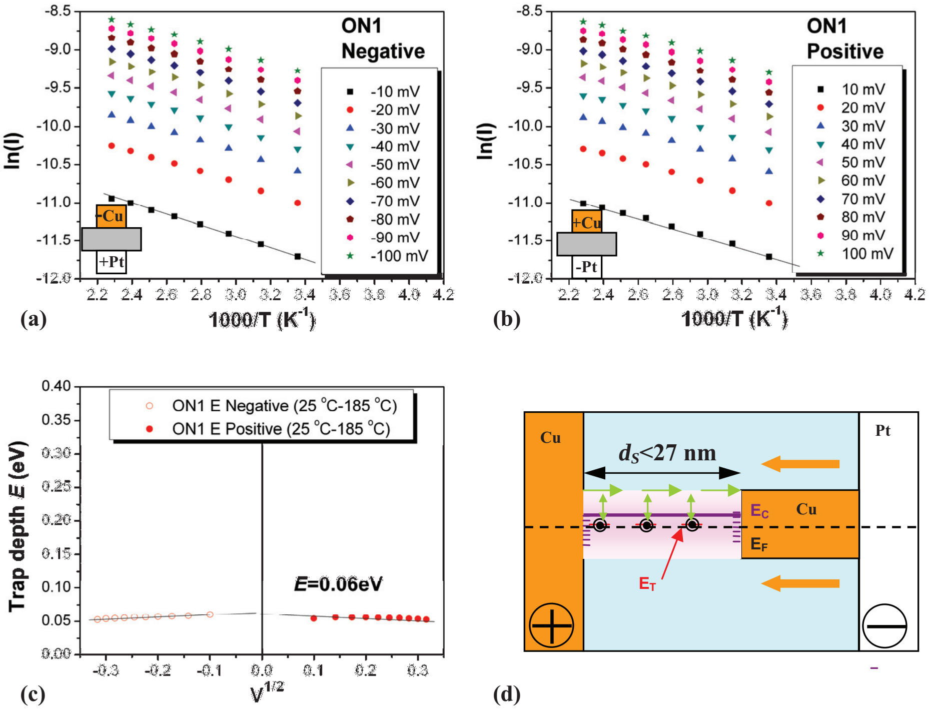

Figure 6.25: Temperature dependence of-current voltage characteristics of ON1 plotted as $\ln(I)$ versus $1000/T$ for (a) negative and (b) positive bias on the Cu

electrode. (c) Activation energy E_a extracted from the slope.

From this point of view, the activation energy is ($\Delta + E_C - E_T$) and around 0.06 eV which can be obtained by extrapolating the points in Figure 6.25 (c) to 0 V. This energy is very close to the Fermi level E_F. When account is take of the thermal activation energy Δ of carrier mobility, the trap depth ($E_C - E_T$) will be lower than 0.06 eV and very close to E_C as well as near the Fermi level E_F.

The corresponding conduction mechanism in the ON1 state is sketched in Figure 6.25 (d) in terms of the energy band diagram for a conductive channel between two electrodes. The filament grows from the cathode (Pt) to the anode (Cu) as indicated by the two orange arrows, and this is called a virtual cathode. Thus, the length of the SCLC d_S should be less than 27 nm. This state could be an intermediate state between the OFF state with an open channel and the metallic ON3 state with metallic bridging between two electrodes as already sketched in Figure 6.15. This is suggested by the measurement results, for example the $I \propto V^2$ dependence at higher voltages, the activation energy being symmetric regardless of electrode differences. The conduction band edge E_C shown as a thick violet line and the Fermi level E_F shown as a black line are sketched with a very narrow energy separation of 0.057 eV as calculated from the experimental results. The trap energy in red is distributed over the entire filament located near the Fermi level with an energy depth less than 0.06 eV below E_C.

ON2 state

The second low resistance state, ON2, exhibits a linear current-voltage characteristic at all temperatures from 25°C to 185°C (Figure 6.26 (a)) and has a resistance of 400 Ω at room temperature. The linear behaviour of the *I*-*V* relation can be regarded as a hopping process. However the ON2 state cannot be classified as metallic conduction because the conduction current increases with increasing temperature. Such a kind of current conduction can be often observed in doped semiconductors, where the electrons travel through localized states under the applied electrical field. Hopping conduction in semiconductor materials can be expressed as follows:

$$I = AN\mu E \exp(-\frac{E_a}{kT}) \qquad 6.28$$

$$slope = \frac{\ln I}{\frac{1000}{T}} = -\frac{E_a}{1000k} \qquad 6.29$$

where *A* is the lateral size of the switching area or filament, *N* is the carrier density, *μ* is the mobility of the carriers in the filament and E_a is the activation energy needed for hopping from one localized state to another. Figure 6.26 (b) plots ln *I* as a function of 1000/*T* at five different voltages. A linear behaviour can be indentified between 25°C and 65°C with a similar activation energy E_a of ~ 0.07 eV. A second stage can be observed in the higher temperature range above 105°C with much lower activation energy E_a of ~ 0.02 eV, almost constant with voltage.

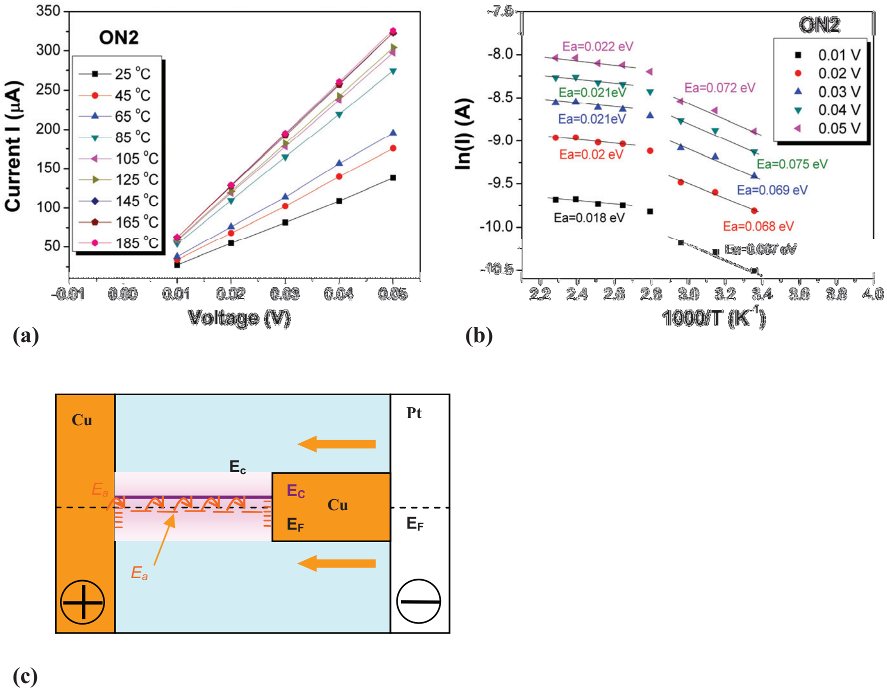

Figure 6.26: Temperature dependence of current-voltage characteristics in the ON2 state plotted as (a) *I* versus *V* and (b) ln *I* versus 1000/*T*. (c) Band diagram of hopping conduction in the ON2 state of the cell.

The hopping mechanism inside the cell in the ON2 state is sketched in Figure 6.26 (c). A very low activation energy of ~ 0.02 eV (105 °C to ~ 165 °C) and low resistance ~ 400 Ω imply a larger defect density in the bulk. It is still unknown exactly what kind of composition the filament is made from. Possibly, the injected Cu atoms or the reduced TiO_x work as traps for current conduction by releasing and capturing electrons in the electrical field.

ON3 state

The third low resistance state ON3 has a very low resistance of 79 Ω and is characterised by metallic conduction in that the resistance increases with increasing temperature from 25 °C to 165 °C, as plotted in Figure 6.27 (b). As already calculated above, the temperature coefficient of the filament is very close to the published value for Cu nanowires larger than 15 nm in diameter. Therefore it can be concluded that the filament is most probably Cu. As the temperature continues to increase from 165 °C, the resistance increases dramatically by more than 2 orders of magnitude to ~

18 kΩ, as shown in Figure 6.27 (a), where the arrows with numbers indicate the heating and the cooling procedure. This high resistance remained stable at 205°C and also at room temperature (25 °C). The OFF state (blue stars) before the cell is set to ON3 was ~40 kΩ, which is very close to the resistance of the cell after the low resistance is turned OFF, as indicateby arrows 2 and 3 in Figure 6.27 (a).

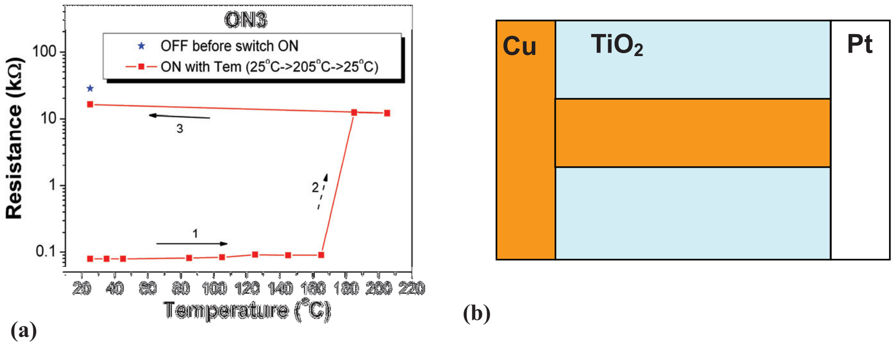

(a) (b)

Figure 6.27: Temperature dependence of resistance in ON3 state (a) 25 °C to 205 °C and back to 25 °C. (b) Cu filament formed between two electrodes.

6.3.4 Discussion

Five resistance states in cells with the same nominal structure and size were measured at different temperatures up to 185 °C. Their resistances at room temperature are all plotted together in Figure 6.14 (a) in different colours. The resistance reduces depending on resistance state in the sequence R(initial) > R(OFF) > R(ON1) > R(ON2) > R(ON3). On the basis of the temperature measurements, various conduction mechanisms can be identified. The extracted activation energy reduces with decreasing resistance, as shown in Figure 6.28. The activation energy of metallic ON3 can be ignored.

The nature of the resistance changes suggests a transformation from semiconductor to metallic characteristics with decreasing resistance. Stoichiometric TiO_2 is generally considered to be a good insulator with a relatively wide band gap between 3.05–3.5 eV. Increasing either the density of O vacancies or the density of impurities in the form of foreign metallic impurities can enhance the conductivity of TiO_2-based materials. The corresponding Fermi level is pushed closer to the conduction band edge E_C and to the valence band edge E_V by increasing donor or acceptor impurities, respectively. In the former case, a slightly reduced sub-oxide of TiO_2 increases the conductivity dramatically as listed in Table 2.1. In the latter case, the insulating stoichiometric TiO_2 becomes an n-type semiconductor by extrinsic doping with V, Ta, or Nb [95] or a p-type semiconductor by doping with Al, Fe, or In. [96, 97, 98] Therefore, the reduction of resistance depends on different programmed resistance states and is due to the change of stoichiometry in the TiO_2 thin film. Cu can be detected in thin films after electro-forming. Cu should contribute to resistance degradation of the cell either by being incorporated as an interstitial atom to form a donor impurity or in Ti^{4+} sites as a acceptor impurity. However, electrical conduction in the presence of p-type doping with Al or Fe is still related to O vacancies and can change to n-type conduction. In Cu-doped TiO_2 thin films, room temperature ferromagnetism (RTFM) has been observed experimentally by Duhalde [99] and Errico [100] has explained this phenomena on the basis of *ab initio* calculations in which oxygen vacancies play a critical role for the appearance of RTFM and such Cu impurities favour the formation of oxygen vacancies. These theoretical results are verified by the experiments of Hou. [101] XRD and XPS confirmed that Cu substitutes for Ti^{4+} ions, resulting in a stretching of the lattice constant. The RTFM effect reduces with increasing Cu concentration, similar to Cu-doped ZnO. [102] The increase in the Cu impurity density reduces the distance between neighbouring Cu atoms and thus a larger proportion of adjacent cation lattice positions will be occupied, which induces antiferromagnetism. As a consequence, the effect of ferromagnetism is weakened by increasing the Cu impurity concentration. The $Ti_{0.8}Cu_{0.2}O_2$ thin film proves to be an n-type semiconductor with a resistivity lower than 5 Ω.cm at 300 K. The sample was deposited by reactive magnetron sputtering on a substrate at 673 K and annealed at 873 K in vacuum for 30 minutes. In our case, Cu diffuses into the TiO_2 thin film under the action of the applied electrical field during the electro-forming and switching procedures. Although the exact composition of the filament is still unknown, the above-mentioned published results could suggest similar properties for the Cu-doped channel in the incomplete portion of Cu filament between the grown Cu tip and anode. As the Cu impurity density increases, the isolated Cu impurities become connected and form a complete metallic chain.

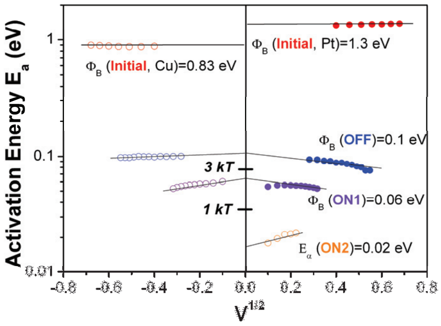

Figure 6.28: Extracted activation energy E_a of cells in the initial, OFF, ON1 and ON2 states, measured at temperatures between 105 °C and 185 °C.

A simple physical model could be used here to explain the above-mentioned observations. The resistance states and current conduction mechanism change with increases in defect or impurity densities, which are on the result of the ion migration under the proper electrical field or electrical energy applied to the cell during forming, switching ON and switching OFF procedures.

Firstly, the asymmetric SBH barrier (0.8 eV for Cu/TiO_2 and 1.3 eV for Pt/TiO_2) reduces dramatically from the initial state to the OFF state (0.1 eV) due to the creation of an interface and possibly bulk defects in the channel during the electro-forming process. This can be confirmed by a clear reduction of the depletion width d at the interface, under the assumption that the Cu impurities in the channel are all retraced back to the Cu electrodes, resulting in an optical dielectric constant ε which is similar to that in the initial state.

The intermediate states (ON1 and ON2) between the OFF state and the metallic ON3 state are semiconducting as mentioned above, which could be the result of an incompletely formed Cu filament, because the Cu ions migrate from anode to cathode during the SET procedure in the same channel where the filament simultaneously grows from cathode to anode. It is very possible that the channel becomes highly conductive while growing the Cu filament tip and anode because of the transport of Cu ions through the channel, but the density of the Cu ions there are still not high enough to form a complete Cu chain.

In the ON3 state, metallic conduction is due to the formation of a Cu chain with an increasing density of defects or impurities. The Cu filament thus connects to the anode and makes the cell metallic.

6.4 Resistive switching in Ag/TiO_2/Pt structures

Sputtering of polycrystalline TiO_2 thin film of 50 nm thickness was integrated between micro-crossbar structured Pt and Ag electrodes. Compared to resistive switching in TiO_2, either with two Pt electrodes or with one Cu electrode as discussed in chapters 3 and 4, the Ag/TiO_2/Pt cells exhibited a much lower current down to 50 nA during resistive switching. On the other hand, there was no obvious electro-forming process needed to initiate the cell and start resistive switching; the cell was already the initial state ready for switching. Multi-level bipolar resistive switching is shown in Figures 6.29 (a) and (b) in the nano-ampere and micro-ampere ranges, respectively, where five continuous cycles with the same compliance current are plotted in the same colour. Resistive switching with a compliance current from 50 nA to 10 μA had almost the same SET ON voltage at 0.2 V and also similar SET OFF voltage at –0.05 V. From the point of view of applications, such low operating currents and voltages give great advantages in the design of low power consumption memory or logic devices.

More than 3,600 sweep cycles were consequently repeated with 100 µA compliance current on Ag/TiO2/Pt cells with a cross point size of 2 x 2 µm^2 shown in Figure 6.30 (a). Their switching characteristics such as the form of the I(V) curves, the SET ON and SET OFF voltages were very similar from cycle to cycle. The resistances in the ON (LRS) and OFF (HRS) states were measured every 50 cycles at 0.05 V and are plotted in Figure 6.30 (b) as red points and black empty points, respectively. The ratio of R_{OFF} to R_{ON} was more than two orders of magnitude.

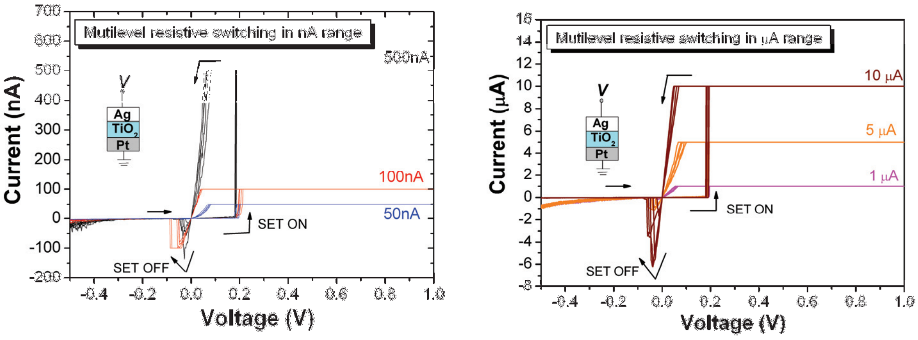

(a) **(b)**

Figure 6.29: Bipolar resistive switching in Ag/TiO$_2$/Pt cell of 2 x 5 µm^2 area at different compliance currents in the (a) nA and (b) µA range.

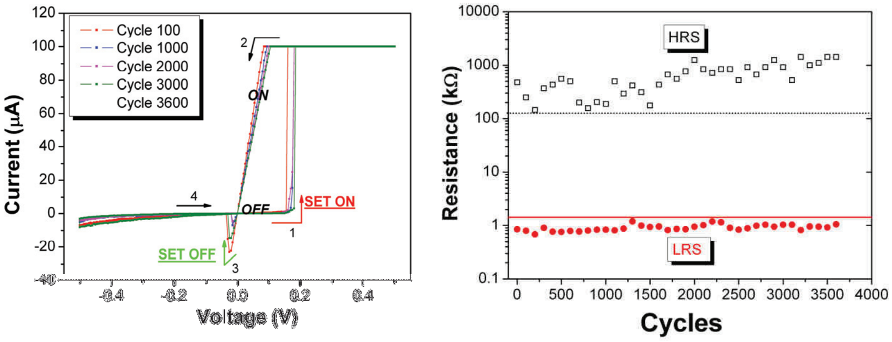

(a) **(b)**

Figure 6.30: (a) Stable continuous sweep cycles with 100 µA compliance current. (b) Resistances in the HRS and LRS states measured every 50 cycles at 0.05 V.

Long pulse measurements were conducted and are plotted in Figure 6.31 (a). The cell can be written ON and written OFF repeatedly with +2 V and -2 V, respectively, with 300 ms long pulses. The resistance states were read out by low voltage pulses at 0.1 V for 50 ms. This SET-Read-RESET-Read procedure was repeated for 100 cycles.

Figure 4.33 (b) shows the read-out resistances in the ON (black) and OFF (red) states after SET and RESET. The ratio of the resistances in the two states RON/ROFF remained one order of magnitude. Generally, the voltage (±2 V) needed for SET and RESET of the pulse measurements is much higher than the switching voltage (+0.2 V and ~ -0.08 V) in the sweep procedure. This could be a reason why the ratio of the resistances in the two states is not identical in the case of pulse measurements and sweep procedures. The long pulse measurements show a memory effect which is controlled by electrical pulses; this is the basic model for programming and reading out memory states in many commercial memory devices.

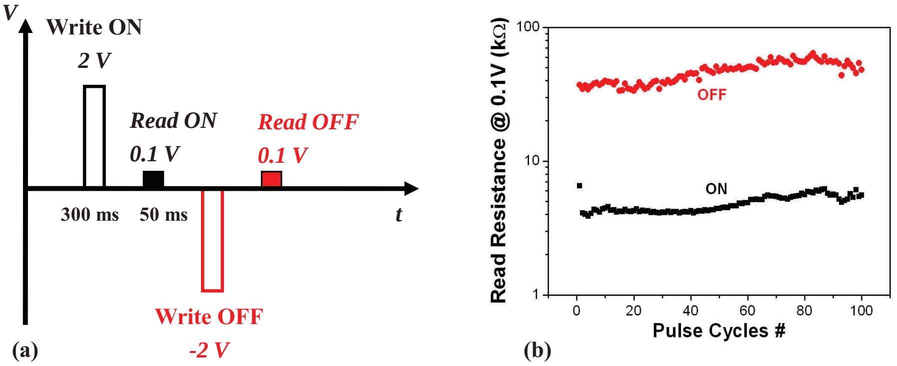

Figure 6.31: (a) Schematic diagram of the pulse measurements for operation of Write ON, Read ON, Write OFF, Read OFF. (b) The ON and OFF resistance states read at 0.1 V from continuous long pulse measurements on a Ag/TiO_2/Pt stack structure.

One of the serious problems besetting resistive switching in Ag/TiO_2/Pt cell structures is the retention and thermal stability of the resistance state, especially the ON resistance state. Although the LRS can be set to different levels corresponding to the compliance current, the LRS set by a compliance current less than 100 μA had very poor retention at room temperature. The LRS state can disappear after several minutes or even seconds. Only very low ON resistances are non-volatile at room temperature, as depicted in Figure 6.32, where the LRS of 23 Ω was confirmed to be metallic in that the resistance increased with temperature. According to equation 6.5, the temperature coefficient of the filament, here in Ag/TiO_2/Pt, can be calculated to be 3.5 x 10^{-3} K^{-1}, which is very close to the value (3.8 x 10^{-5} K^{-1}) reported in the literature. Therefore, a Ag filament is confirmed. The HRS decreased with increasing temperature but became unstable above 125°C. However, this LRS returned back to the HRS after cooling down to room temperature from 185°C, as indicated by the blue triangle in Figure 6.32. Thus, the resistance increased by more than two orders of magnitude to be very close to the HRS at room temperature. The same phenomenon was also observed on a second pad with a resistance of 55 Ω on the same sample. This resistance reversal took place during cooling down of the sample holder of the probe station. This process can be attributed to dissolving of Ag atoms from filaments during heating and cooling down as sketched in Figure 6.32 (b). But what happens exactly to result in disruption of the LRS is yet to be understood in further studies. Tsunoda has reported similar low current resistive switching and thermal instability of the LRS above room temperatures. [13]

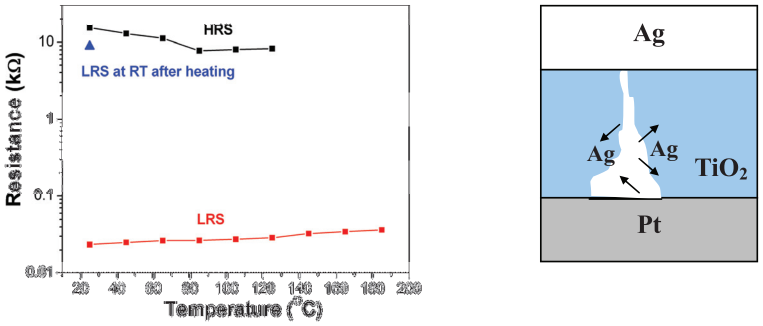

(a) **(b)**

Figure 6.32: Temperature dependence of LRS (red) and HRS (black). The LRS turns to a HRS after heating (blue). (b) Schematic diagram of the dissolving of Ag from the filament into the surrounding bulk TiO_2.

6.5 Conductive AFM study of resistive switching in a $Cu/TiO_2/Pt$ cell

6.5.1 CAFM on pristine ALD TiO_2

The switching characteristics of pristine ALD TiO_2 thin films with a thickness of 30 nm were investigated with by CAFM measurements at 10^{-5} mbar and at room temperature with a JEOL JSPM-4210A. Figure 6.33 (a) sketches the measurements set-up: the Pt-coated tip works as a mobile Pt top electrode and is grounded. A voltage is applied to the Pt bottom electrode. The local current-voltage characteristic is measured by settling the tip on an arbitrarily chosen position on the film. A resistive switching curve is observed as shown in Figure 6.33 (b).The inset picture enlarges the $I(V)$ curve with a voltage sweep between 0 and 1.5 V. The black and red arrows indicate the sweeping procedure in the forward and reverse directions, respectively. A read voltage (V_{read}) of 1 V is used to read out a sufficiently large current and therefore the resistance states after the writing and erasing processes. The corresponding OFF/ON ratio is only about 2 as given by the currents in the OFF (260 pA) and ON states (120 pA) at 1 V. Switching was polarity-dependent as shown by the curves, where the resistance state changed to the LRS state as sweeping started from -8 V at the bottom electrode (+8 V at the tip) and changed to the HRS upon sweeping from 8 V at the bottom electrode (-8 V at the tip). This form of bipolar resistive switching is also observed in large area devices as described in the next section .

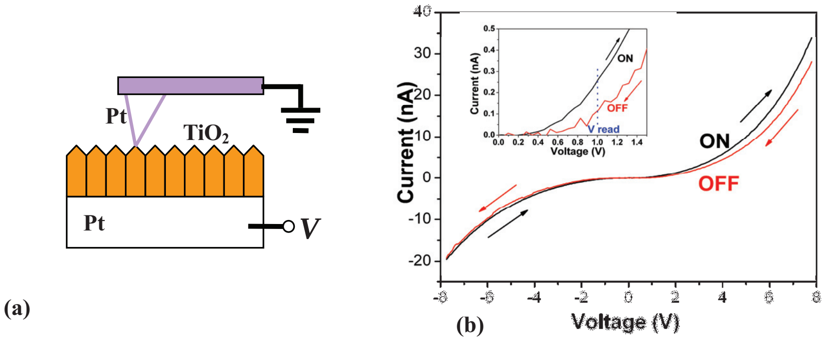

Figure 6.33: (a) Schematic diagram of CAFM measurement set-up. (b) Typical I(V) curves of local resistive switching of the Pt tip/ALD 30 nm TiO_2/Pt MIM structure.

The surface topography and current image were acquired simultaneously after every CAFM scanning cycle. The central image of Figure 6.34 (a) shows the topography of the concerned area on the surface of the TiO_2 film. The surface roughness was measured to be 0.423 nm (rms) reflecting a corrugated form produced by the polycrystalline structure of the film, as discussed already in chapter 2. It should be mentioned that, according to the study of Peter el al., an adsorbate layer causes an additional potential drop between the Pt tip and the bulk material. [76, 77] Therefore, using 1 V as the read voltage (V_{read}) can increase the current response between tip and actual TiO_2 layer. Meanwhile this voltage does not change the sample resistance state. Figures 6.34 (b) to (e) illustrate current images of the CAFM experiments read with a V_{read} of +1 V over the 500 x 500 nm^2 area, where the central area of 200 x 200 nm^2 could be repeatedly SET (write ON) and RESET (Erase) after scanning under -7 V and +7 V, respectively. At the beginning, a 500 x 500 nm^2 large square was scanned with V_{read} = 1 V showing no significant conduction and was found to be in the OFF state (Figure 6.34 (b)). Then, the LRS was written in the centre 200 x 200 nm^2 region by scanning the tip under a SET voltage of -7 V relative to the bottom electrode (+7 V at tip). The bright contrast in the current image of Figure 6.34 (c) demonstrates the LRS, whereas the other area in dark is in the HRS state, which was not scanned by any SET or RESET procedures. In the polycrystalline TiO_2 thin film, almost the entire area after a SET scan showed better conductivity. The current in the LRS is a maximum 156 nA, which is of the same order of magnitude as the current measured at a single location, as illustrated above in Figure 6.33 (b).

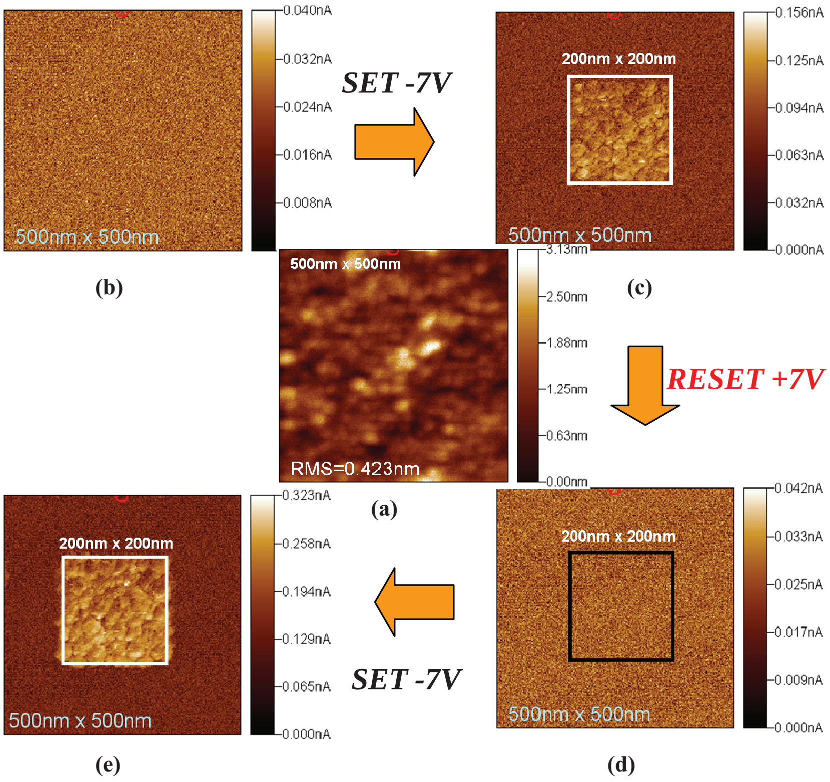

Figure 6.34: Current images with $V_{read} = +1$ V in the same area of size 500 nm x 500 nm after SET and RESET operations with -7 V and +7 V, respectively, in the centre 200 nm x 200 nm area. (a) is the topography measured simultaneously with the current image. (b), (c), (d), (e) indicate the OFF, ON, OFF, ON states read out with 1 V after SET or RESET operation sequences.

The transfer between resistance states did not affect the surface topography noticeably. Such a kind of resistance switching in the central area can be repeated consistently, as shown in Figures 6.34 (d) and (e). The LRS can be erased and changed to the HRS by scanning the centre region with +7 V applied to the bottom electrode (-7 V at tip) as shown in Figure 6.34 (d). Again, the central region can be switched to the LRS by applying -7 V to the bottom electrode during the SET scan as shown in Figure 6.34 (e). The local switch between the two resistances has an OFF/ON ratio larger than 5 although the magnitude of the current is very small around several hundred pico-amperes in the LRS.

6.5.2 CAFM on TiO_2 after removing Cu electrode

The second set of CAFM experiments concentrates on the influence of the Cu top electrodes on the switching mechanism. First, the Cu/TiO_2/Pt cell as sketched in the inset of Figure 6.35 (a) is set to the ON state with a static voltage sweep as shown in Figure 6.35 (a). After switching a Cu/TiO_2/Pt stack into the LRS, the top electrode was removed by wet etching in 0.1 mol $FeCl_3$ for 90 seconds. ToF-SIMS analysis proves already that, after Cu deposition and electro-forming, a certain amount of Cu migrates into the TiO_2 up to the interface between titanium dioxide and Pt counter electrode. The CAFM measurement is conducted on this etched cell as sketched in Figure 6.35 (b).

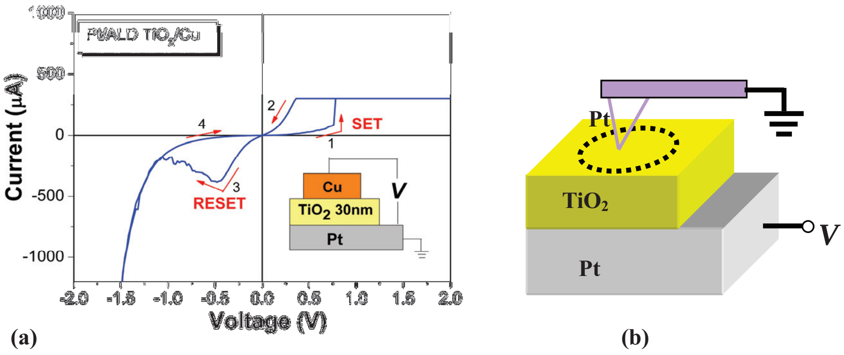

Figure 6.35: (a) Switching current-voltage characteristics of the Cu/TiO_2/Pt cell. (b) Schematic diagram of CAFM measurement set-up after removing the Cu top electrode.

A CAFM scan of 500 nm x 500 nm reveals many hillocks with a diameter up to 100 nm and a height up to 40 nm randomly distributed. Moreover, these spots are always conductive and can be switched repetitively from LRS to HRS and vice versa (Figure 6.36 (a-d)). The small images show the corresponding topographies. The large images depict the current images recorded with $V_{read} = +1$ V as “read out” of the resistance in the area. Between each read-out cycle, the whole area was scanned with $V = \pm 4$ V during SET and RESET scans. The conductive spots always appear in the same positions (compare Figures 6.36 (a) and (c)) without any change of topography. By moving the AFM tip to one of the more conductive locations, continuous $I(V)$ sweeps similar to those observed on cells with Cu top electrodes were measured (Figure 6.36 (e)). This supports the idea that the formation of Cu or Cu^{n+} filaments is responsible for the resistive switching effect in Cu/TiO_2/Pt stack cells.

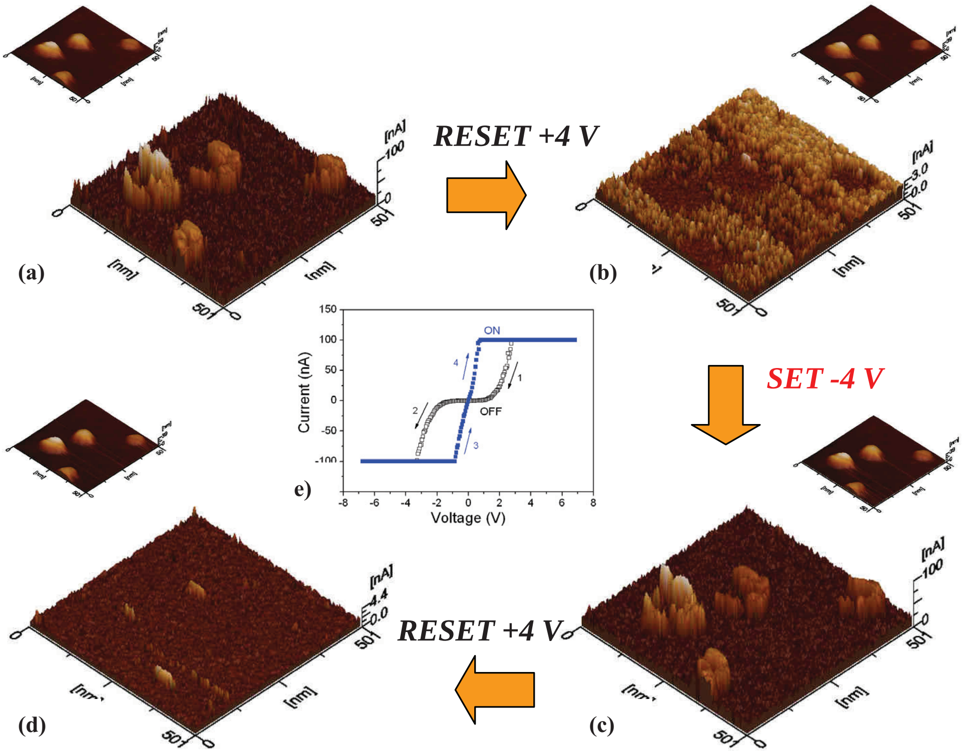

Figure 6.36: Sequential read out cycles after writing or erasing operations show reversible resistive switching and their respective surface topographies (small figures): a) LRS, b) HRS, c) LRS, d) HRS can be set by scanning with -4V for LRS and +4V for HRS. e) Typical I(V) hysteretic cycle on a single filament. The bias is swept from -7 V to +7 V (blue) to set the HRS and then swept reversely from +7 V to -7V to reset to the LRS (empty squares). The compliance current is set to 100 nA.

6.5.3 Characterization of a single conductive spot

On the basis of the CAFM results discussed in the last section, the conductive nature of a single hillock was not everywhere uniform. In order to get more insight into the resistive switching behaviour of a single conductive spot, two CAFM experimental set-ups were conducted by scanning an area including only one hillock with SET and RESET voltages as well as by applying a SET and RESET voltage sweep on a single point of the hillock.

Figure 6.37 demonstrates the repeated resistance change of a bump between LRS (images (a) and (c)) and HRS (images (b) and (d)) by scanning the Pt tip over the area, where only a single bump was found and is illustrated in image (e). The current images from (a) to (d) were read out with +1 V on the bottom electrode (-1 V on the tip) after the area was written (SET) with -6 V on the bottom electrode (+6 V on the tip) and erased (RESET) with +6 V on the bottom electrode (-6 V on the tip) sequentially, as indicated by the yellow arrows. A large LRS/HRS current ratio of around 20 can be achieved after the SET and RESET procedures. Meanwhile, the topography of the concerned area remains unchanged during either SET (RESET) or reading processes. Moreover, the conductive capability on the same dot was position-dependent, which is clearly observed in the current image of the LRS shown in images (a) and (c). A gap at the same position in both pictures shows a much weaker conductivity compared to the other area of the bump indicated with the blue arrows. But there was still the open question as to whether the entire bump switches as a unit or separately depending on the location of the hillock?

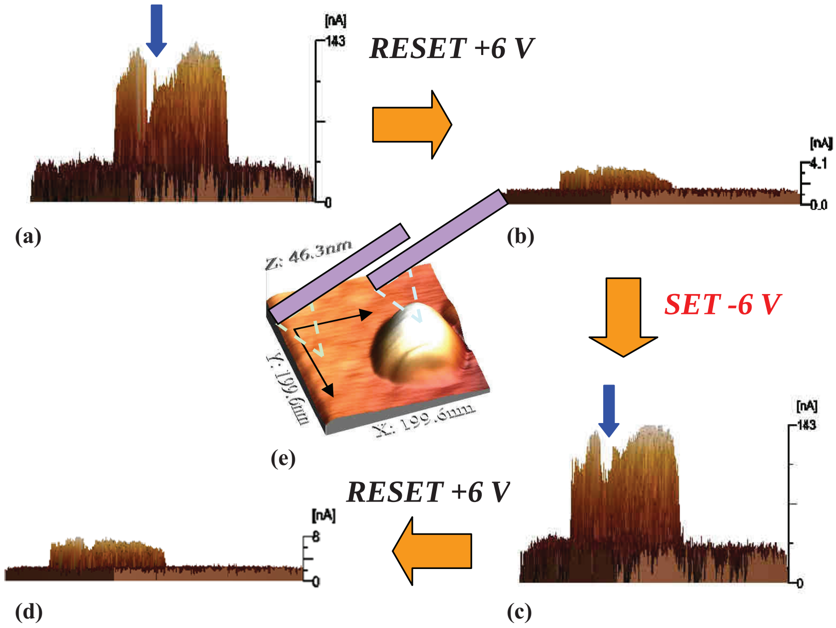

Figure 6.37: Sequential read-out cycles with V_{read} = +1 V after SET and RESET scans with -6 V and +6 V respectively over an area including a single hillock and showing reversible resistance states: a) LRS, b) HRS, c) LRS, d) HRS. (e) The topography did not change during resistive switching.

A very small region as small as 10 nm x 10 nm on the dot can be switched OFF by scanning with +6 V on the bottom electrode. Figures 6.38 (a) and (b) show the current images read with +1 V before and after the RESET scan respectively in the area indicated by the blue frames. The current contour along the blue dotted lines sketched in both states give more concrete information about the change in conductivity in the dot as shown in Figure 6.38 (c). The corresponding RESET region is marked between two straight lines, where the ratio of the current before RESET to that after RESET is between 5 and 15, according to different positions in the region. It is also found that the neighbouring region outside the RESET scan area (33 nm < x < 40 nm and 50 nm < x < 60 nm) clearly changes its conductivity as well, which could be due to the electrical field dispersed around the Pt tip as illustrated in Figure 6.38 (d). However the 10 nm x 10 nm scanned area experiences the most strong resistance change and therefore highlights the great potential in realizing very fine resistive switching structures scaled down to 10 nm.

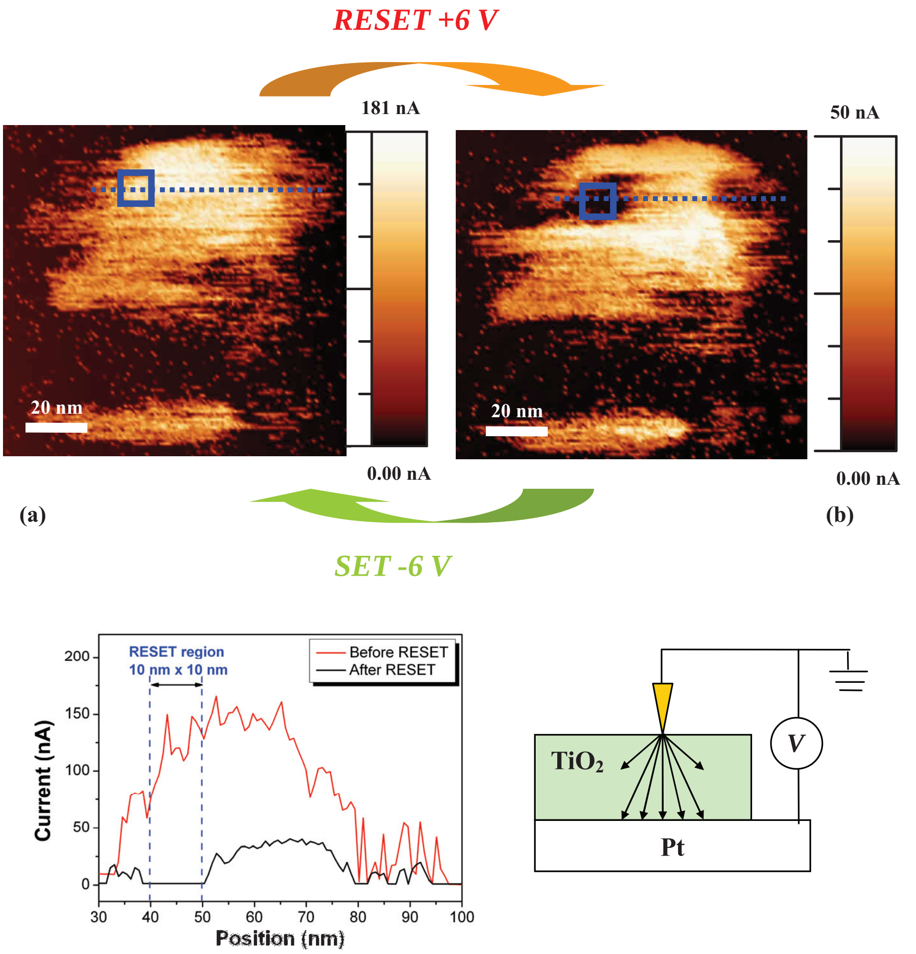

(a) (b)

(c) (d)

Figure 6.38: Current image read with V_{read} = +1 V (a) before RESET and (b) after RESET in a 10 nm x 10 nm area indicated by the blue square. The RESET voltage is +6 V on the bottom electrode (-6 V at the tip). (c) The current contour along the

dotted lines in images (a) and (b) showing the large difference in conductivity in both states. (d) Schematic diagram of the electric field from the tip to the bulk layer. The surrounding area can also be influenced by this electrical field.

To answer this question, the second measurement set-up sketched in Figure 6.39 (a) was carried out by keeping the tip fixed and in contact with the surface in area A on the bump and then applying a voltage sweep with 100 nA compliance current shown in image (b) for SET (-6 V to +6 V) and RESET (+6 V to -6V) procedures, respectively. The read-out scan with +1 V on the bottom electrode throughout this whole area includes only one bump and indicates that the resistance change occurs only in the small area surrounding the tip position after the SET and RESET voltage sweeps, as shown in images (c) to (f). In the read-out procedure, a much higher

compliance current of 1000 nA was set to get the real conduction current at +1 V. Area A was the location where the tip made contact with the surface during the SET and RESET voltage sweeps. Areas B and D belong to the higher conductivity region on the same bump, whereas area C has very poor conductivity and forms a gap in current between B and D. Resistive switching occurs only in area A, around the tip position, which proves to be a local phenomenon and the resistance of the other areas (areas B, C, D) remained almost unchanged during repetitive SET (RESET) and read-out procedures. The maximum current difference in area A can be estimated to be around 60 µA (from LRS to HRS), whereas the maximum current in area A in the HRS was much larger than that measured during the voltage sweep in Figure 6.39 (b). The reason for this may be due to the different contact positions of the tip as the tip was ordered to move to a chosen location in both cases. Therefore, the position at which the tip makes contact is not always the same from cycle to cycle, which may cause the differences observed in the HRS current. This measurement indicates that, even on a single dot, the switchable area can be limited down to 25 nm depending on the tip diameter. Down-scaling of the switching geometry to the low nanometres is therefore possible and implies a very high integration density of resistive switching memory cells via crossbar arrays.

From the above discussion of the CAFM measurements, the local formation of filaments can be confirmed and related to resistive switching in Cu/TiO_2/Pt structures. Although the exact composition of the observed dispersed bumps is unknown, diffusion of Cu subsequent to the forming and switching procedures could take place during resistive switching. Switching on a single bump provides great potential to scale down the switching area to 10 nm, which is beneficial for further integration of high density ReRAM cells in future applications.

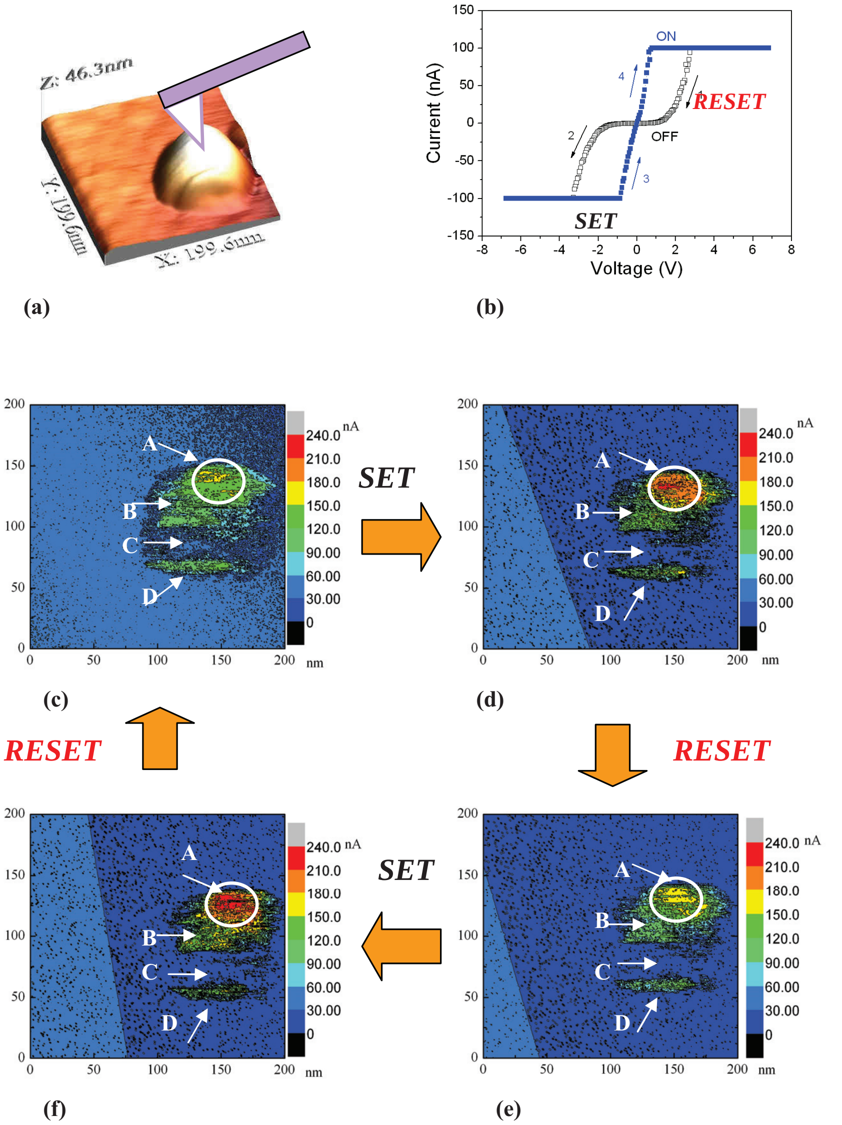

Figure 6.39: (a) Topography unchanged by resistive switching. (b) Resistive switching curves at position A with SET and RESET voltage sweeps. Sequential read-out cycles by scanning entire area with $V_{\mathrm{read}} = +1$ V after SET and RESET voltage sweeps at a single point on the bump showing reversible resistance changes locally: c) HRS, d) LRS, e) HRS, f) LRS. A, B, C, D with corresponding arrows indicating the different areas on the bump.

Chapter 7 Summary and outlook

Summary

The subject of this thesis is the study of the resistive switching effect in thin TiO_2 films and a better understanding to reduce the switching current for low power applications and increase retention and endurance of the RRAM cells.

Thin TiO_2 films are deposited in two different ways: magnetron reactive sputter deposition and atomic layer deposition. Films deposited with both methods are of polycrystalline structure. However the crystalline structure of the sputtered TiO_2 shows clearer column structures along the deposition direction. The ALD TiO_2 thin films show finer structures and much smoother surface morphology. Conductive AFM measurements on both virgin TiO_2 films with a thickness of 60 nm indicate the resistive switching of the whole area. The results reveal that the virgin sputtered TiO_2 is better conductive not only near the grain boundaries but also on the crystalline columns.

Some further behaviors are found in the Pt/60 nm TiO_2/Pt MIM cells. Electro-forming is needed to initiate the cell to be ready for the repetitive resistive switching. Both bipolar and unipolar resistive switching can be transferred repetitively depending on the compliance current. Low current bipolar resistive switching can be observed with a compliance current of 200 μA. Multilevel bipolar resistive switching is also obtained by setting the compliance current properly even up to 5 mA. Stable repeatable unipolar resistive switching can be obtained with 10 mA current compliance. Bubbles appear frequently on the top Pt electrode as the cells are switched with high current above 5 mA, which could be attributed to the formation of the O_2 gas near the anode interface region as the result of the redox electrochemical process. One possible reason for the formation of the bubbles only in the top electrode could be the much smaller top electrodes (150 μm diameter) than the continuous 1 inch platinized substrate, which focuses the electrical field and thus attracts more O ions to the anode. The microscopic morphology changes after forming or switching in the form of bump formations during conductive AFM measurements by scanning the surface with a very sharp Pt tip as mobile anode electrode. Within the bump some area is much better conductive. These better conductive locations become dramatically weakened as the sample is exposed into the air, which could imply a re-oxidation of the filament resulting in the reduction of the conductivity. In conclusion, the microscopic CAFM results show that the polarity dependent morphology changes and the bipolar resistive switching are similar to the macroscopic observations on the Pt/TiO_2/Pt stack structure, which thus confirms the filament model.

In the Cu/TiO_2/Pt system an electro-forming procedure is also necessary to form the cell to start the resistive switching and therefore is studied with samples with two different thicknesses of 27 nm and 60 nm TiO_2 and different pads size. It is advantageous to using this mode because forming is to be finished with only one forming procedure, therefore the forming parameters of different pads can be compared with each other. Firstly the electrical field for the forming is almost the same regardless the thickness and the pad size of 4, 25 and 100 μm^2. This may suggest an ion migration related process, in which similar migration barrier should be overcome for the hopping of the ions in the TiO_2 layer in different thickness and pads size. The switching current increases with increasing pad size and the film thickness. However, after the electro-forming the resistance of the cells with thicker TiO_2 is almost constant and at least 50 % lower than that in the cells with thinner TiO_2. The calculated total input energy $W=UIt$ before the forming reaches is also almost constant in the thicker cells and clearly larger than those in the thinner cells, which may suggest more ion migration in the forming process for thicker cells and thus resulting in a lower resistance. The low resistance state after forming can be switched back to high resistance state using a sweep under negative bias on the Cu top electrode to initiate the cell for the repetitive resistive switching.

The resistive switching behavior in the Cu/TiO_2/Pt system after forming has the similar characteristics observed in the ECM system such as the GeSe with Ag or Cu electrodes. It shows multilevel switching with a wide span of the low resistance states depending on the current compliance between hundred micro amperes and several milli amperes. The low current switching is generally much lower and more stable than that in the Pt/TiO_2/Pt systems, which could be attributed to the easier migrations of the Cu than the oxygen migrations in most solid materials. By replacing the Cu electrode with a Ag electrode the switching behavior is very similar to the Ag/Ag:GeSe/W system with similar very low switch ON voltage at around 200 mV and the switching can be observed with low current compliance down to 50 nA.

Evidence for the metal migrations related to the resistive switching is given. The ToF-SIMS analysis shows the Cu distributing in the thin TiO_2 layer after the Cu top electrodes are removed from the pads Cu/TiO_2/Pt, which is already set to ON state. Therefore Cu migration should be related to the resistive switching in this system. However more precise analysis scaling down to the nano meter range is until now still difficult. On the other hand, the temperature dependent measurements on the pads of Cu/TiO_2/Pt and Ag/TiO_2/Pt indicate a metallic conduction. The calculated temperature coefficients in both cells are very close to the published value of the Cu and Ag wires. Therefore the filaments in both cases should be metallic Cu or Ag wires, which are formed by Cu or Ag migrations from the top Cu or Ag electrodes.

Conductive AFM measurements are carried out on the pad after removal of the top Cu electrode, which is already set to low resistance state. With this method the local conductivity under the Cu electrode can be observed and characterized. Bumps in diameter around 50 - 100 nm distribute inhomogeneous on the surface, which is normally better conductive than other areas outside these bumps but they can be switched back to similar high resistance states as the other area by scanning with negative bias on the tip through the region including the bumps. Such kind of switching between two states can be repeatedly observed with a R_{OFF}/R_{ON} ratio of around 20. Even on the same bump the switching can be limited down to 10 nm x 10 nm area with the sharp tip. The repeatedly local resistive switching on a single bump can also be observed around the motionless tip by applying the SET or RESET voltage sweeping on it. These results of the resistive switching in the very fine area around the 10 nm x 10 nm indicates the great potential to reduce the effective cell size dramatically for the future RRAM application.

Temperature measurements are conducted on the pads in configuration of $Cu/TiO_2/Pt$ in different resistance states of virgin, OFF and 3 ON states with reduced resistances. Their current conduction is discussed on the base of the basic conduction mechanisms in the MIM structure. The virgin state shows typically Schottky emission between 105 ^{o}C and 165 ^{o}C with the Schottky barrier height of 1.3 eV at Pt/TiO_2 and 0.83 eV at Cu/TiO_2 interfaces by fitting the measured current lines with Schottky model, similar to the published results. With the measured refractive index (n=2.5) of TiO_2 by Ellipsometry the depletion width is calculated which reduces with increasing temperature. The similar Schottky like conduction could be resulted in the OFF state but with much lower barrier height ~ 0.1 eV between 105 ^{o}C and 165 ^{o}C. The depletion width in OFF state is much narrower than that in virgin state. The metallic ON3 state is proven to be the Cu filament by comparing the temperature coefficient with the literatures. The other two low resistance states show their semiconducting conduction and thus could be the intermediate state between the OFF state and the metallic ON state as the result of the possibly incomplete formed channel between the top of growing Cu filament and the anode. Under this model, the growing process could be frozen as the region between containing higher Cu concentration resulting in much better conduction than the OFF state but worth conduction than the final metallic state.

Outlook

The resistive switching mechanisms in the TiO_2 with either both Pt electrodes or one electrochemically active electrode (Cu or Ag) is confirmed to be related to the formation and disruption of the local filament in the thin films based on this work. However there are still some questions open. In the $Pt/TiO_2/Pt$ system it is still very difficult to observe directly the suggested oxygen migrations based conductive path, which is properly composed by defective TiOx. Applying the high resolution TEM on a single crystalline TiO_2 thin film may help to find out the local changing in the composition or the structures after forming or switching. The similar method could be used to detect the electrochemically active Cu or Ag ions in the TiO_2 thin films of amorphous, polycrystalline or single crystalline phases. However, whether the oxygen migration takes place in the resistive switching in Cu/TiO_2/Pt system is still to be answered with more additional evidences.

For the future RRAM application the electro-forming process must be avoided. Therefore it will be very advantageous to produce the cells ready for switching. Well controlled Cu doping in TiO_2 thin films or the introduction of the defective TiOx is possibly a good way to create channel for easy ion migration. A system study on the resistive switching in such samples can find out the optimal concentration and preparing process for non forming switching cells. Cu is very compatible to the CMOS technology and widely used in the microelectronic circuits. One possible way to reduce the switch ON and OFF voltage is to introduce the Cu metal particles in the TiO_2 by implantation or through the deposition processes. The defective TiOx could make the oxygen migration easier than the TiO_2 thin films and thus may change the resistive switching properties in the Pt/TiO_2/Pt system.

Ultra short pulse measurements down to nano seconds should be investigated in the Cu/TiO_2/Pt system in order to find out the switching speed limitation of the cells and compare the published high speed resistive switching speed in the Pt/Ti/TiO_2/Pt system ~ 10 ns. For this purpose the size of the cells should be reduced down to nano meter scale to reduce the RC time. The further reduction of the cell size is also the requirements for the high density integrations on the chip. The nano structures for investigation here can be prepared with E-beam lithography or the nanoimprint lithography. The further optimization of the switching speed could be done on samples with different Cu doping concentration in the TiO_2 thin films.

As the very good compatibility of the Cu and TiO_2 to the existing CMOS technology, there should be still large potential to improve the resistive switching performance of the Cu/TiO_2/Pt system. Therefore, the further optimization of the resistive switching in the TiO_2 thin films can be continued with the focus on devices made of Cu doping or the defective TiOx. On the other side, CAFM can still be used to investigate the nanometer scale resistive switching with separated very fine Cu nano particles on the surface of the thin films. Comparing the local conduction on virgin thin film and the thin film with nano Cu particles may give more insight into the ion migrations through the defects.

Bibliography

---

1 http://www.semiconductor.net/article/354546-IBM_Readies_32_nm_eDRAM_With_Low_Latency.php

2 http://www.hynix.com/datasheet/pdf/flash/HY27UH08AG(5_D)M%20(Rev0.6).pdf

3 "Past, Present and Future of MRAM", NIST Magnetic Technology, 22 July 2003

4 DJ. Lee, YS. Seok, DC. Choi, JH. Lee, YR. Kim, HS. Kim, DS. Jun, OH. Kwon, VLSI Circuits, 1992. Digest of Technical Papers., 1992 Symposium on Volume, Issue , 4-6 Jun 1992 Page(s):64 – 65

5 A Memory Breakthrough, Kate Greene, Technology Review, 04-Feb-2008

6 "Intel, STMicroelectronics Deliver Industry's First Phase Change Memory Prototypes". Numonyx. 2008-02-06. Retrieved 2008-08-15.

7 C. Schindler, M. Weides, M. N. Kozicki, R. Waser, Appl. Phys. Lett. 92, 122910 (2008)

8 http://gizmodo.com/334274/could-fujitsus-reram-replace-flash-storage

9 K. Szot, W. Speier, G. Bihlmayer, and R. Waser, Nat. Mater. 5, 312 (2006).

10 http://www.4-d-s.com/technology.html

11 D. B. Strukov, G. S. Snider, D. R. Stewart, R. S. Williams, Nature 453, 80-83,(2008)

12 D. S. Jeong, H. Schroeder, R. Waser, Electrochem. Solid-State Lett., 10, Issue 8, pp. G51-G53 (2007)

13 K. Tsundona, Y. Fukuzumi, J.R. Jameson, Z. Wang, P.B. Griffin, Y. Nishi, Appl. Phys. Lett. 90, 113501 (2007)

14 A.E. Feuersanger, “Titanium-dioxide dielectric films prepared by vapour reaction,” Proceedings of the IEEE, vol. 52, no. 12, pp. 1463–1465, 1964.

15 E.T. Fitzgibbons, K.J. Sladek, and W.H. Hartwig, “TiO2 film properties as a function of processing temperature,” Journal of the Electrochemical Society, vol. 119, pp. 735–739, 1972.

16 http://en.wikipedia.org/wiki/File:Anatase-unit-cell-3D-balls.png

---

17 http://en.wikipedia.org/wiki/File:Rutile-unit-cell-3D-balls.png

18 Y. Takahashi, K. Tsuda, K. Sugiyama, H. Minoura, D. Makino, and M. Tsuiki, “Chemical vapour deposition of TiO2 film using an organometallic process and its photoelectrochemical behaviour,” Journal of the Chemical Society: Faraday Transactions 1, vol. 77, pp. 1051–1057, 1981.

19 K.H. Guenther, “Recent progress in optical coating technology: low voltage ion plating deposition,” in SPIE, 1990, vol. 1270, pp. 211–221.

20 H.K. Pulker, G. Paesold, and E. Ritter, “Refractive indices of TiO2 films produced by reactive evaporation of various titanium-oxygen phases,” Applied Optics, vol. 15, no.12, pp. 2986–2991, 1976.

21 A. Bendavid, P.J. Martin, and H. Takikawa, “Deposition and modification of titanium dioxide thin films by filtered arc deposition,” Thin Solid Films, vol. 360, pp. 241–249, 2000.

22 Metal Oxides – Chemistry and Application, edited by J.L.G. Fierro, Taylor and Francis Group, 2006

23 The CRC Handbook of Solid State Electrochemistry, edited by P.G. Gellings and H.J.M. Bouwmeester, CRC Press, Inc. 1997

24 P.A. Cox, Transition Metal Oxides: An Introduction to Their Electronic Structure and Properties, Clarendon Press, Oxford 1995.

25 O.T. Sorensen, Nonstoichiometric Oxides, Academic, New York 1981.

26 Y. Takahashi, A. Ogiso, R. Tomoda, K. Sugiyama, H. Minoura, and M. Tsuiki, “Electrical and electrochemical properties of TiO2 films grown by organometallic chemical vapour deposition,” Journal of the Chemical Society, Faraday Transactions 1, vol. 78, pp. 2563–2571, 1982.

27 P. Kofstad, Nonstoichiometry, Diffusion and Electrical Conductivity in Binary Metal Oxides, Wiley-Interscience, New York, 1972.

28 N. Tsuda, K. Nasu, A. Yanase, and K. Siratori, Electronic Conduction in Oxides, Springer-Verlag, Berlin, 1983.

29 R.J. Lad, Surf. Rev. Letter. 2, 109 (1995)

30 C.T. Campbell, Surf. Sci. Rep. 27, 1 (1997)

31 R. Waser and M. Aono, Nat. Mater. 6, 833 (2007)

32 R. Waser, R. Dittmann, G. Staikov, K. Szot, Adv. Mater. 21, 2632–2663, (2009)

---

33 E. Loertscher, J. W. Ciszek, J. Tour, H. Riel, Small 2, 973 (2006).

34 H. Kohlstedt, N.A. Perstev. J.R. Contreras, R. Waser, Phys. Rev. B 72 (2005) 125341-1-10

35 Y. Hirose, H. Hirose, J. Appl. Phys. 1976, 47, 2767.

36 X. Guo, Appl. Phys. Lett. 91, 133513, (2007)

37 K. Terabe, T. Hasegawa, T. Nakayama, M. Aono, Quantised conductance atomic switch. Nature, 433, pp. 47–50, (2005)

38 M. Kund, et al. Conductive bridging RAM (CBRAM): an emerging non-volatile memory technology scalable to sub 20 nm. IEDM Tech. Digest, 754–757, (2005).

39 M. N. Kozicki, M. Yun, L. Hilt, and A. Singh. Proceedings of Solid-State Ionic Devices, Seattle, WA, USA, 02/05/1999-07/05/1999, Pennington, NJ, USA: Electrochem. Soc, 298-309 (1999)

40 T. Sakamoto,a) H. Sunamura, H. Kawaura, T. Hasegawa, T. Nakayama, M. Aono, Appl. Phys. Lett. 82, (2003)

41 M. N. Kozicki, C. Gopalan, M. Balakrishnan, M. Park, M. Mitkova, in Proc. IEEE Non-Volatile Memory Technology Symp, p. 10. (2004)

42 C. Schindler, S. C. P. Thermadam, R. Waser, M. N. Kozicki, IEEE Trans. Electron Devices 2007, 54, 2762.

43 L. Yang, K, Carsten, C, Szot, A. Ruediger, R. Waser, APPLIED PHYSICS LETTERS, 95, 013109, (2009)

44 W. Guan, S. Long, Q. Liu, M. Liu, W. Wang, IEEE Electron Device Lett. 2008, 29, 434.

45 T. Kever, U. Bottger, C. Schindler, R. Waser, Appl. Phys. Lett. 2007, 91, 083506.

46 M. Balakrishnan, M. Kozicki, C. Poweleit, S. Bhagat, T. Alford, M. Mitkova, J. Non-Cryst. Solids 2007, 353, 1454.

47 D. M. Smyth, Prog. Solid State Chem. 1984, 15, 145.

48 P. A. Cox, Transition Metal Oxides: An Introduction to Their Electronic Structure and Properties, Clarendon Press, Oxford 1995.

49 O. T. Sorensen, Non-stoichiometric Oxides, Academic, New York 1981.

50 K. Szot, W. Speier, R. Carius, U. Zastrow, W. Beyer, Phys. Rev. Lett. 2002, 88, 075508/1.

---

51 J. JH. Yang, M. D. Pickett, XM. Li, D. A. A. Ohlberg, D. R. Stewart, R. Stanley Williams, Nature Nanotechnology 3, 429 - 433 (2008)

52 K. Szot, W. Speier, G. Bihlmayer, R. Waser, Nat. Mater. 5, 312, (2006)

53 A. Sawa, Mater. Today 2008, 11, 28.

54 A. Baikalov, et al., Appl. Phys. Lett. 83, 957, (2003)

55 S. Tsui, et al., Appl. Phys. Lett. 85, 317, (2004)

56 X. Chen, et al., Appl. Phys. Lett. 87, 233506, (2005)

57 Y.B. Nian, et al., Phys. Rev. Lett. 98, 146403, (2007)

58 A. Sawa, et al., Appl. Phys. Lett. 85, 407, 3(2004)

59 T. Fujii, et al., Appl. Phys. Lett. 86, 012107, (2005)

60 B. J. Choi, D. S. Jeong, S. K. Kim, C. Rohde, S. Choi, J. H. Oh, H. J. Kim, C. S. Hwang, K. Szot, R. Waser, B. Reichenberg, and S. Tiedke, J. Appl. Phys. 98, 033715 (2005)

61 D. S. Jeong, H. Schroeder, and R. Waser, Appl. Phys. Lett. 89, 082909 (2006)

62 D. C. Kim, S. Seo, S. E. Ahn, D.-S. Suh, M. J. Lee, B.-H. Park, I. K. Yoo, I. G. Baek, H.-J. Kim, E. K. Yim, J. E. Lee, S. O. Park, H. S. Kim, U.-I. Chung, J. T. Moon, and B. I. Ryu, Appl. Phys. Lett. 88, 202102 (2006)

63 K.M. Kim, B.J. Choi, B.W. Koo, S.C., D.S. Jeong, C.S. Hwang, Electrochemical and Solid-State Letters, 9 (12) G343-G346 (2006)

64 D.S. Jeong, Phd. Thesis, 2008.

65 R. Yasuhara, K. Fujiwara, K. Horiba, M. Kotsugi, F. Guo, H. Kumigashira, M. Oshima, H. Tagaki, Workshop on Oxide Electronics WOE15, Estes Park, 2008, (Poster).

66 D.S. Jeong, H. Schroeder, R. Waser, Electrochemical and Solid-State Letters, 10 (8), G51-G53 (2007)

67 J.J. Yang, M.D. Pickett, X. Li, D.A.A. Ohlberg, D.R. Stewart, R.S. Wlliams, Nat. Nano,. 3(7) 429-433, (2008)

68 A. Ahnd, Semicond. Int. 26, 46–51, (2003)

69 M. Vehkamaki et al., Electrochem. Solid-State Lett. 2, 504–506, (1999).

70 K.E. Elers et al., Chem. Vap. Deposition 4, 149, (2002)

---

71 C. Nauenheim, PhD thesis (2009)

72 P.D. Greene, E.L. Bush, I.R. Rawlings, Proc. Symp. on Deposited Thin film Dielectrical Materials, Montreal, Ed. F. Vratny, New York: The Elelctrochemical Society, p.167–185 (1969).

73 K.M. Kim, B.J. Choi, B.W. Koo, S. Choi, D.S. Jeong and C.S. Hwang, Electrochemical and Solid-State Letters, 9 (12), G343–G346 (2006).

74 D.S. Jeong, H. Schroeder and R. Waser, Appl. Phys. Lett., 89, 082909 (2006).

75 C. Rohde, B.J. Choi, D.S. Jeong, S. Choi, J.S. Zhao, C.S. Hwang, Appl. Phys. Lett. 86, 262907 (2005).

76 F. Peter, K. Szot, R. Waser, B. Reichenberg, S. Tiedke and J. Szade, Appl. Phys. Lett., 85, 2896–2898, (2004).

77 F. Peter, J. Kubacki, K. Szot, B. Reichenberg and R. Waser, Phys. Stat. Sol. A 203, No. 3, 616–621 (2006).

78 R. Waser, R. Dittmann, G. Staikov and K. Szot, Advanced Materials, 21, 2632–2663 (2009).

79 C. Schindler, PhD thesis, (2009).

80 R. A. Serway (1998). Principles of Physics (2nd ed.). London: Saunders College Pub., pp. 602.

81 D. Griffiths (1999) [1981]. "7. Electrodynamics". In: A. Reeves (ed.) Introduction to Electrodynamics (3rd ed.). Upper Saddle River, New Jersey: Prentice Hall, pp. 286.

82 A. Bid, A. Bora and A. K. Raychaudhuri, Phys. Rev. B 74, 035426 (2006).

83 A. Bendavid, P. J. Martin and H. Takikawa, “Deposition and modification of titanium dioxide thin films by filtered arc deposition,” Thin Solid Films, 360, 241–249 (2000).

84 C. R. Ottermann, R. Kuschnereit, O. Anderson, P. Hess and K. Bange, “Young’s modulus and density of thin TiO2 films produced by different methods,” Materials Research Society Symposium Proceedings, 436, 251–256 (1997).

85 B. S. Richards, Novel Uses of Titanium Dioxide for Silicon Solar Cells, PhD. Thesis, University of New South Wales (2002).

86 A. Linsebigler, C. Rusu and J. T. Yates Jr., “Absence of platinum enhancement of a photoreaction on TiO2–CO photooxidation on Pt/TiO2(110)”, J. Amer. Chem. Soc. 118, 5284, (1996).

---

87 X. Z. Ji and G. A. Somorjai, Continuous hot electron generation in Pt/TiO2, Pd/TiO2, and Pt/GaN catalytic nanodiodes from oxidation of carbon monoxide, J. Phys. Chem. B 109, 22530, (2005).

88 K. D. Schierbaum, X. Wei-Xing, S. Fischer and W. Göpel, Springer Series Surf. Sci. 33 (1993).

89 Th. Dittricha, V. Zinchuk, V. Skryshevskyy, I. Urban and O. Hilt, J. Appl. Phys. 98, 104501 (2005).

90 D. L. Carroll, M. Wagner, M. Rühle and D. A. Bonnell, J. Mater. Res. 12, 975 (1997).

91 G. Grosso and G. P. Parravicini, “Solid State Physics”, San Diego: Academic Press, 2000

92 P. A. Cox, ”Transition Metal Oxides: An Introduction to Their Electronic Structure and Properties”, Oxford: Clarendon Press, 1992.

93 K. Zakrzewska, A. Brudnki, M. Radecka and W. Posadowski, “Reactively sputtered TiO2−x thin films with plasma-emission-controlled departure from stoichiometry,” Thin Solid Films, 343-344, 152–155 (1999).

94 K. C. Kao and W. Hwang, Electrical Transport in Solids, International Series in the Science of the Solid State, New York: Pergamon, 1981, pp.150–170.

95 N. Golego, S. Studenikin and M. Cocivera, “Thin-film polycrystalline titanium dioxide grown by spray pyrolysis,” On-line abstract for Surface Canada 97 conference, May 21-24, Sherbrooke, Canada, 1997.

96 D. Mardare and G. I. Rusu, “Structural and electrical properties of TiO2 RF sputtered thin films,” Materials Science and Engineering B, 75, 68–71 (2000).

97 A. Bernasik, M. Rekas, M. Sloma and W. Weppner, “Electrical surface versus bulk properties of Fe-doped TiO2 single crystals,” Solid State Ionics, 72, 12–18 (1994).

98 S. R. Kurtz and R. G. Gordon, “Chemical vapor deposition of doped TiO2 thin films,” Thin Solid Films, 147, 167–176 (1997).

99 S. Dulalde, M. F. Vignolo, F. Golmar, C. Chiliotte, C. E. R. Torres, L. F. Vabrera, M. Renteria, F. H. Sanchez and M. Weissmann, Phys. Rev. B 72, 161313 (R) (2005).

100 L. A. Errico, M. Renter´ıa. and M. Weissmann, Phys. Rev. B 72, 184425 (2005).

101 D. L. Hou, H. J. Meng, L. Y. Jia, X. J. Ye, H. J. Zhou and X. L. Li, EPL, 78, 67001 (2007).

102 D. B. Buchholz, R. P. H. Chang, J. H. Song and K. J. Betterson, Appl. Phys. Lett., 87, 082504, (2005).

Resume

Lin Yang
Changzhou, China

Date of birth: 17/06/1976 in China
Nationality: Chinese

09/2005-12/2009	Institute of Electronic Materials (IWE2), RWTH Aachen Institute of Solid State Research (IFF), Forschungszentrum Jülich Ph.D student Dissertation: Resistive switching in TiO2 thin films
11/2002-06/2005	RWTH Aachen Master of Material Science, Specialization: Micro and Nanotechnology Master thesis: Selforgnized patterned magnetic nanodots fabricated by ion sputtering on the GaSb/Co/GaSb semiconductor heterostructure
09/1995-07/2000	South China University of Technology, China Bachelor of Engineering (Electronic Materials and Devices) Bachelor of Economy (International Economy and Trade)
09/1989-07/1995	Middle and High School of Qijichang, Changzhou
09/1983-07/1989	Primary School of Qijichang, Changzhou

Publications:

1. **L. Yang**, C. Kuegeler, K. Szot, A. Ruediger, R. Waser, The influence of copper top electrodes on the resistive switching effect in TiO2 thin films studied by conductive atomic force microscopy, APPLIED PHYSICS LETTERS, **95**, 013109, (2009),

2. T. Watanabe, S. Hoffmann-Eifert, **L. Yang**, A. Rüdiger, C. Kügeler, C. S. Hwang, R. Waser, Liquid Injection Atomic Layer Deposition of TiOx Films Using Ti[OCH(CH3)2]4, Journal of The Electrochemical Society, **154** (12) G262-G269 (2007)

3. T. Bobek, N. Mikuszeit, J. Camarero, S. Kyrsta, **L. Yang**, M. Á. Niño, C. Hofer, L. Gridneva, D. Arvanitis, R. Miranda, J. J. de Miguel, C. Teichert, H. Kurz, Self-Organized Hexagonal Patterns of Independent Magnetic Nanodots, Advanced Materials, **19**, Issue 24, 4375-4380, (2007).

Schriften des Forschungszentrums Jülich
Reihe Information

1. **Ferrocenes as Potential Building Blocks for Molecular Electronics**
   Self-Assembly and Tunneling Spectroscopy
   by L. Müller-Meskamp (2008), 153 pages
   ISBN: 978-3-89336-509-8

2. **Magnetic Proximity Effects in Highly-ordered Transition Metal Oxide Heterosystems studied by Soft x-Ray Photoemission Electron Microscopy**
   by I. P. Krug (2008), XX, 180 pages
   ISBN: 978-3-89336-521-0

3. **Seltenerd-basierte ternäre Oxide als alternative Gatedielektrika**
   von J. M. Roeckerath (2008), 148 Seiten
   ISBN: 978-3-89336-543-2

4. **Strominduzierte Magnetisierungsdynamik in einkristallinen Nanosäulen**
   von R. Lehndorff (2009), I, 86 Seiten
   ISBN: 978-3-89336-564-7

5. **Magnetization Dynamics in Magnetically Coupled Heterostructures**
   von A. Kaiser (2009), X, 121 pages
   ISBN: 978-3-89336-577-7

6. **Resistive switching in Pt/TiO$_2$/PT**
   by D. S. Jeong (2009), vii, 133 pages
   ISBN: 978-3-89336-579-1

7. **Electromechanical Force Microscopy and Tip-Enhanced Raman Spectroscopy for Polar Oxide Nanoparticles**
   by S. Röhrig (2009), vi, 114 pages
   ISBN: 978-3-89336-600-2

8. **Investigation of resistive switching in barium strontium titanate thin films for memory applications**
   by W. Shen (2010), 114 pages
   ISBN: 978-3-89336-608-8

9. **Nanostrukturierte Metallelektroden zur funktionalen Kopplung an neuronale Zellen**
   von D. Brüggemann (2010), vii, 160 Seiten
   ISBN: 978-3-89336-627-9

10. **Integration of resistive switching devices in crossbar structures**
    by Chr. Nauenheim (2010), XII, 142 pages
    ISBN: 978-3-89336-636-1

11. **Correlation between Raman spectroscopy and electron microscopy on individual carbon nanotubes and peapods**
by C. Spudat (2010). xiv, 125 pages
ISBN: 978-3-89336-648-4

12. **DC and RF Characterization of NiSi Schottky Barrier MOSFETs with Dopant Segregation**
by C. J. Urban (2010), iv, 151 pages
ISBN: 978-3-89336-644-6

13. **Alternative Systems for Molecular Electronics: Functionalized Carboxylic Acids on Structured Surfaces**
by M. C. Lennartz (2010), 183 pages
ISBN: 978-3-89336-667-5

14. **Highly conductive electrodes as diffusion barrier for high temperature applications**
by B. Mešić (2010), VII, 138 pages
ISBN: 978-3-89336-670-5

15. **Modeling, Fabrication and Characterization of Silicon Tunnel Field-Effect Transistors**
by C. P. Sandow (2010), XIII, 112 pages
ISBN: 978-3-89336-675-0

16. **Substituted Coronenes for Molecular Electronics: From Supramolecular Structures to Single Molecules**
by P. Kowalzik (2010), ix, 149 pages
ISBN: 978-3-89336-679-8

17. **Resistive switching in TiO2 thin films**
by L. Yang (2011), VII, 117 pages
ISBN: 978-3-89336-707-8

Information / Information
Band / Volume 17
ISBN 978-3-89336-707-8

JÜLICH
FORSCHUNGSZENTRUM